PNNL-24552

Pacific Northwest
NATIONAL LABORATORY

Proudly Operated by Battelle Since 1965

Front-end Electronics for Unattended Measurement (FEUM): Results of Prototype Evaluation

July 2015

RC Conrad
DT Keller
SJ Morris
LE Smith

U.S. DEPARTMENT OF ENERGY

Prepared for the U.S. Department of Energy
under Contract DE-AC05-76RL01830

DISCLAIMER

PACIFIC NORTHWEST NATIONAL LABORATORY
operated by
BATTELLE
for the
UNITED STATES DEPARTMENT OF ENERGY
under Contract DE-AC05-76RL01830

Printed in the United States of America

Available to DOE and DOE contractors from the
Office of Scientific and Technical Information,
P.O. Box 62, Oak Ridge, TN 37831-0062;
ph: (865) 576-8401
fax: (865) 576-5728
email: reports@adonis.osti.gov

Available to the public from the National Technical Information Service,
U.S. Department of Commerce, 5285 Port Royal Rd., Springfield, VA 22161
ph: (800) 553-6847
fax: (703) 605-6900
email: orders@ntis.fedworld.gov
online ordering: http://www.ntis.gov/ordering.htm

This document was printed on recycled paper.
(9/2003)

PNNL-24552

Front-end Electronics for Unattended Measurement (FEUM): Results of Prototype Evaluation

RC Conrad
DT Keller
SJ Morris
LE Smith

July 2015

Prepared for
the U.S. Department of Energy
under Contract DE-AC05-76RL01830

Pacific Northwest National Laboratory

ACRONYMS AND ABBREVIATIONS

AWG	arbitrary waveform generator
COTS	commercial off the shelf
DIP	dual in-line package
DUT	device under test
EMI	electromagnetic interference
FEUM	Front-end Electronics for Unattended Measurements
HDPE	high density polyethylene
HV	high voltage
IAEA	International Atomic Energy Agency
LED	light-emitting diode
MCA	multichannel analyzer
NGAM	Next Generation ADAM Module
NGSI	Next Generation Safeguards Initiative
PW	digital pulse width
RFI	radio frequency interference
SCA	single channel analyzer
τ	analog shaping time
TTL	transistor-transistor logic
UMS	unattended monitoring system(s)

TABLE OF CONTENTS

LIST OF TABLES

LIST OF FIGURES

1 ABSTRACT

The International Atomic Energy Agency (IAEA) deploys unattended monitoring systems to provide continuous monitoring of nuclear material within safeguarded facilities around the world. As the number of unattended monitoring instruments increases, the IAEA is challenged to become more efficient in the implementation of those systems. In 2010, the IAEA initiated the Front-End Electronics for Unattended Measurement (FEUM) project with the goals of greater flexibility in the interfaces to various sensors and data acquisition systems, and improved capabilities for remotely located sensors (e.g., where sensor and front-end electronics might be separated by tens of meters). In consultation with the IAEA, a technical evaluation of a candidate FEUM device produced by a commercial vendor has been performed. This evaluation assessed the device against the IAEA's original technical specifications and a broad range of important parameters that include sensor types, cable lengths and types, industrial electromagnetic noise that can degrade signals from remotely located detectors, and high radiation fields. Testing data, interpretation, findings and recommendations are provided.

2 SUMMARY

The International Atomic Energy Agency (IAEA) deploys unattended monitoring systems to provide continuous monitoring of nuclear material within safeguarded facilities around the world. As the number of unattended monitoring instruments increases, the IAEA is challenged to become more efficient in the implementation of those systems. In 2010, the IAEA initiated the Front-End Electronics for Unattended Measurement (FEUM) project with the goals of greater flexibility in the interfaces to various sensors and data acquisition systems, and improved capabilities for remotely located sensors (e.g., where sensor and front-end electronics might be separated by tens of meters). In consultation with the IAEA, under funding from the U.S. National Nuclear Security Administration's Next Generation Safeguards Initiative (NGSI), and with support from Los Alamos National Laboratory and Idaho National Laboratory, Pacific Northwest National Laboratory (PNNL) has performed an evaluation of FEUM prototype devices developed by Bot Engineering, Ltd (Canada).

The evaluation of the FEUM candidate devices was originally expected to begin in October 2013 and to be completed in late 2014. Due to delays in the delivery of the initial prototypes by vendor, and design deficiencies in the first two versions received by PNNL, the evaluation results presented in this report were predominantly collected since receipt of the latest version of the Device Under Test (DUT) in January 2015.

PNNL's test and evaluation plan for the FEUM prototypes is based on the functional requirements and performance targets communicated by the IAEA in its original procurement specifications and prior publications. Functional testing analyzed basic electronics characteristics, for example, gain and discriminator linearity, shaping amplifier characteristics, and dead-time behavior. Performance testing was focused on the ability of the FEUM devices to perform reliably and with sufficient contrast between signal and noise to support the IAEA's often demanding deployment applications (e.g., high neutron count rates in an intense gamma-ray background). Performance testing was conducted in baseline scenarios (ideal conditions) and also in "noisy" electromagnetic (EM) and high-radiation environments intended to represent typical IAEA installations. For all tests, the FEUM prototype was stimulated by one or more of four input signal types: an arbitrary waveform generator (AWG) that produces a tail-pulse signal generally representative of radiation sensors, ^{3}He proportional counters, ^{235}U fission chambers and NaI(Tl) gamma-ray detectors. The AWG provided a well-characterized, baseline input for functional tests, and idealized outputs to serve as a reference in performance tests. The three detector types are commonly used by the IAEA in unattended instruments and provided an indication of how the FEUM prototype is expected to perform in common IAEA deployments.

This body of this report includes testing data and interpretation of the results for each of the tests performed. The table below provides a summary of the findings for each test; additional discussion is provided here.

- The prototype device supports the various functions specified by the IAEA. There are, however, caveats on that statement for the dynamic range of the gain, discriminator linearity, digital summing, and the absolute accuracy of the high-voltage supply.
- The dead-time characteristics of the device, for the analog and digital outputs, appear consistent with the respective settings for those signals. As with commercially available front-end electronics packages investigated by others, the prototypes exhibited indications of double pulsing at very short shaping times, when coupled to ^{3}He sensors.
- The general trends of the Electronic Noise Charge (ENC) for the device are consistent with expectations, for example, that the ENC decreases with increasing shaping time but increases linearly with input capacitance. In absolute terms, the ENC of the prototype in near-ideal conditions (i.e., low external capacitance and long shaping times) is approximately 1 fC. This is somewhat higher than commercially available low-noise preamplifiers used in high-resolution spectroscopy (~0.2 fC), but consistent with the needs of a FEUM design focused on pulse-counting applications and applicability to a broad range of sensor types.
- Performance testing generally utilized three analog shaping times intended to represent the extremes, and the typical, for IAEA deployments (i.e., 0.1, 0.4 (typical) and 2.4 μs) that must strike a balance between noise discrimination (favoring longer shaping times) and count-rate and gamma-ray pileup management (favoring shorter shaping times). Generally speaking, the performance of the prototypes was good for the typical shaping time, but the extremes often created problems with ballistic deficit (0.1 μs) and gamma-ray pileup (2.4 μs).
- Performance of the FEUM prototype, when coupled to a ^{3}He detector, is consistent with expectations of the IAEA for the charge-sensitive mode. The performance in current-sensitive mode with longer cables, by comparison, is somewhat degraded. Performance of the prototype with a ^{3}He detector operating in high gamma-ray fields also appears to be consistent with expectations and prior work by other groups using different commercially available front-end

electronics packages: for dose rates above 10 R/hr and above, gamma-ray pileup substantially overwhelms the ^{3}He neutron events of interest for most shaping-time and cable combinations.

- Performance when coupled to a NaI(Tl) detector meets expectations for all cable lengths and shaping times tested, and in both charge- and current-sensitive modes. This finding is not surprising given the very large signals generated by NaI(Tl) spectrometers coupled to photomultiplier tubes, and the lack of significant ballistic deficit issues with scintillator detectors.
- The performance-test findings for FEUM when coupled to a ^{235}U fission chamber were encouraging but not conclusive. The primary concern is how well FEUM copes with gamma-ray pileup at very high dose rates, and the testing configurations available at PNNL for this evaluation extended only to 30 R/hr, a gamma-ray field unlikely to significantly challenge the discrimination and neutron-sensitivity for fission chambers. Important to note is that the performance in current-sensitive mode was significantly worse than in charge-sensitive mode for the fission chamber—not unexpected since the signal size produced in fission chambers is significantly lower than in ^{3}He and NaI(Tl) sensors, and the current-sensitive mode is generally more susceptible to noise pickup than is the charge-sensitive mode (at least for the cable types and component configurations tested here).
- Testing in radiated electromagnetic interference (EMI) fields up to ~2 GHz showed that the device susceptibility to interference from such signals is low. It is presumed that the higher-frequency EMI does not have a substantial effect on the performance because the frequency of interference is outside the characteristic frequency typical radiation sensor signals, and the higher frequencies do not couple well, electromagnetically, into the FEUM prototype.

Table 2.1 Summary results of all tests performed on the FEUM prototypes (i.e., DUT).

Test	Result	Comments
Test 1: Feature Conformance Verification	Pass (with caveats)	The DUT departs from the IAEA specifications for several features/functions. Input from the IAEA is needed to determine whether these departures are critical to efficacy in UMS deployments.
Test 2: Pulse Rise Time	Removed	Deemed of limited value, given evaluation objectives.
Test 3: Shaping Amplifier - Gain and Charge Calibration	Pass (with caveats)	Linearity for all gain ranges tested fall within acceptable error bounds ($R^2 > 0.999$). The measured gain values at three different settings are consistent with the vendor-asserted values, but the range of absolute gain provided by the DUT is not as broad (at the high or low end) as that specified by the IAEA.
Test 4: Analog Shaping Constant	Pass	The measured pulse durations for both charge- and current-sensitive modes, as a function of τ, are consistent with theoretical predictions over the full range of τ variability.
Test 5: Discriminator Threshold	Inconclusive	Input from the IAEA is needed to determine whether the relatively low degree of linearity and relatively high offset at the top of the discriminator is critical to UMS deployments
Test 6: TTL Pulse Width	Pass (with caveats)	The DUT has met the basic functional requirements of the test, however further investigation of suspect behavior may be warranted for long digital pulse width settings.
Test 7: Bias Supply Voltage	Pass (with caveats)	The measured versus asserted voltage relationship shows a high degree of linearity but the absolute accuracy progressively degrades as voltage level is increased. It is expected that is accuracy is not problematic for the kinds of sensors utilized by the IAEA, but input from the IAEA is needed on this question.
Test 8: Bias Supply Stability	Inconclusive	Short duration tests were run over a subset of high voltages. Longer-term testing, over a range of nominal values and loads, is needed to provide definitive findings on high-voltage stability.
Test 9: Input/Output Port Resistance	Removed	This test is not feasible for all ports of the device, but for those where it is viable, the measured resistances were consistent with Bot documentation.

Test 10: LED Count Rate	Pass	
Test 11: Isolated Input Power	Pass	The deviation in high voltage and gain due to varying input voltage is minimal and is not expected to impact the operation of typical UMS sensors operated in counting mode.
Test 12: Digital Input Logic Voltage Levels	Pass	The measured pulses for logic levels above the threshold are consistent with expectations.
Test 13: Digital Summing	Inconclusive	At input rates approaching 1 Mcps at the detector and digital input, significant departures from the expected summed rates were observed. More investigation is needed to determine whether this behavior is to be expected, given the design of the device, and whether IAEA uses of FEUM devices would be compromised by this behavior.
Test 14: Grounded Input Power	Pass	The deviation in high voltage and gain due to varying input voltage is minimal and is not expected to impact the operation of typical UMS sensors operated in counting mode.
Test 15: Analog Outputs 1 & 2	Pass	
Test 16: Digital Output Logic Voltage Levels	Pass	
Test 17: Ground Isolation	Pass	
Test 18: NGAM Compatibility	Removed	Deemed of limited value, given evaluation objectives.
Test 19: Baseline FEUM Performance	Pass	The baseline performance for the DUT coupled to a NaI(Tl) detector is generally consistent with expectations, including relatively clean spectroscopic performance in even the most challenging cases with short shaping times and long cables. The relatively high amount of charge produced by a PMT / NaI(Tl) combination makes signal degradation in long cables less problematic than for 3He. The lack of ballistic deficit effects in NaI(Tl), as compared to 3He, are a significant factor in maintaining strong performance even at short shaping times. Performance in charge-sensitive mode was marginally better than for current-sensitive, in terms of the noise floor and FWHM.
Test 20: Radiated EMI/RFI Susceptibility	Pass	The performance of the DUT in radiated EMI conditions was, generally speaking, unchanged from the baseline performance, indicating that the FEUM prototypes are robust against ambient EMI conditions over a broad range of frequencies. There were some results for the 0.4 μs shaping time where degradation in performance was evident, however the reasons are not yet well understood.
Test 21: Conducted EMI/RFI Susceptibility	Removed	Deemed of limited value, given evaluation objectives.
Test 22: Ground Loop Noise	Removed	Deemed of limited value, given evaluation objectives.
Test 23: Dead Time	Pass	The dead time is consistent with the device settings for analog shaping time and digital pulse width. When coupled to ^{3}He sensors, evidence of double-pulsing at very short shaping times.
Test 24: Equivalent Noise Charge	Pass	Best-case ENC of ~1 fC is higher than COTS low-noise preamplifiers used in high-resolution spectroscopy (~0.2 fC), but consistent with counting-system requirements for the IAEA. All ENC trends consistent with expectations.
Test 25: High Radiation Field Susceptibility	Inconclusive	When coupled to ^{3}He sensors, performance degrades significantly above 10 R/hr for typical shaping times, as expected. For ^{235}U fission chamber and charge-sensitive mode, performance is generally consistent with expectations but dose rates are likely too low to stress the system at shorter shaping times. Current-sensitive mode performs poorly over most scenarios—more investigation is needed.

The results and interpretation presented in this report provide the IAEA with an initial evaluation of one candidate FEUM design in terms of functionality and performance. It is expected that this evaluation can help inform an IAEA decision about the path forward for these particular prototypes and more generally, the concept of a unified design for front-end electronics in unattended radiation detection systems. More investigation is likely warranted in several places but, feedback from the IAEA is needed to guide and prioritize those efforts.

3 ACKNOWLEDGEMENTS

This research was supported in part by the U.S. National Nuclear Security Administration (NNSA) Office of Nonproliferation and Arms Control (NA-24) within the U.S. Department of Energy (DOE) under Contract DE-AC05-76RL01830. Pacific Northwest National Laboratory is a multi-program national laboratory operated by Battelle for the U.S. Department of Energy.

The authors would also like to thank Kiril Ianakiev of Los Alamos National Laboratory, and Jeff Sanders, Benjamin Baker, John Svoboda and Jim West from Idaho National Laboratory for helpful suggestions and review during prototype testing.

4 INTRODUCTION

Remotely monitored, unattended nondestructive assay systems are central to the International Atomic Energy Agency's (IAEA's) ability to safeguard an expanding global fuel cycle while balancing the associated manpower and financial resources. In these unattended monitoring systems, the front-end electronics are typically co-located with the detector and often in harsh environments with limited accessibility (e.g., reactor vaults or hot cells). Lack of accessibility to the front-end electronics makes calibration, repair, and replacement of nuclear electronics components problematic. In many of the unattended measurement scenarios undertaken by the IAEA, it would be advantageous to have the front-end electronics a considerable distance from the detector location, for example in an adjacent room where access is more readily available (Figure 1). Additionally, the front-end electronics currently in use have different variations, manufacturers, and interfaces. This creates complications in setup and standardization of equipment. Field experience has shown that front-end electronics (i.e., preamplifier, shaping amplifier, and sometimes discriminator stages) are often the weak link in the IAEA's unattended measurement systems, in terms of reliability and ease of maintenance and configuration.

In 2010, the IAEA began an internal project to investigate improved Front-end Electronics for Unattended Measurement (FEUM), with improvements in deployment flexibility (e.g., separation of detector and front-end electronics), reliability, standardization, and user accessibility as the primary objectives. Preliminary experimental work by the IAEA supported an initial characterization of selected commercially available charge-sensitive and current-sensitive preamplifiers [1]. The results informed technical specifications, including functional requirements and performance targets, for the procurement of front-end electronics specifically engineered to the needs of unattended instruments for nuclear fuel cycle safeguards. Initial FEUM prototypes were fabricated by Bot Engineering, Ltd. (hereafter, "Bot") and evaluation of those candidate devices is needed to better understand where and how advanced FEUM devices could be implemented by the IAEA.

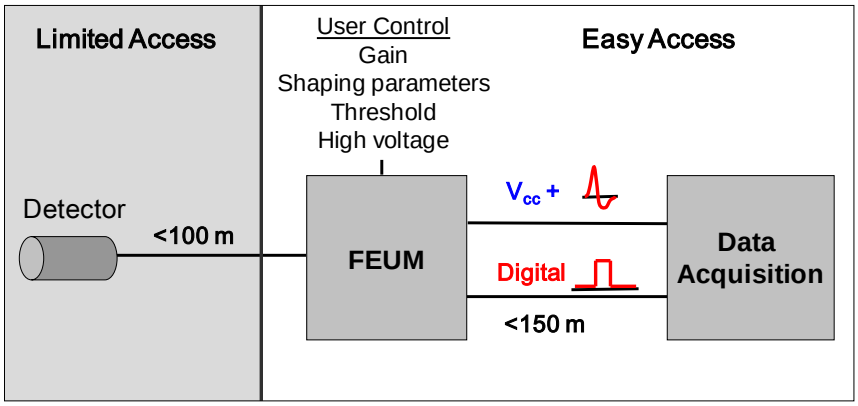

Figure 4.1 Conceptual unattended monitoring system configuration with front-end electronics (FEUM) separated from the detector by up to 100 m, and located outside of limited-access areas. FEUM should have the flexibility to interface with various detector types and IAEA data acquisition platforms that process analog and/or digital pulses and provide the supply voltage (V_{cc}) in varying configurations.

Under support from the U.S. National Nuclear Security Administration's Next Generation Safeguards Initiative (NGSI), Pacific Northwest National Laboratory (PNNL), with support from Los Alamos National Laboratory and Idaho National Laboratory, is performing an evaluation of the FEUM prototype devices [2].

The evaluation of the FEUM candidate devices is significantly behind the original schedule due primarily to delays and deficiencies in the early prototypes delivered by the vendor, Bot Engineering. A summary chronology is provided here:

- October, 2013 — NGSI project begins
- November, 2013 — IAEA provides a first prototype ("FEUM Prototype") to PNNL to support initial testing
- December, 2013 — PNNL places order for two FEUM prototypes; expected delivery date of May, 2014

- Early 2014 — FEUM Prototype failures and design flaws: initial testing is halted
- March-May, 2014 — PNNL provides feedback to Bot regarding device operation and design
- May, 2014 — Bot states that design revisions are in progress; prototype delivery will be delayed
- November, 2014 — PNNL receives originally purchased prototypes ("FEUM v1.0")
- November, 2014 — Catastrophic failures of input protection circuit of FEUM v1.0: testing is halted
- December, 2014 — PNNL returns one prototype to Bot for repair; Bot sends "patch kit" for other
- January 7, 2015 — PNNL receives repaired prototype and uses patch kit to repair the other; testing of FEUM v1.1 as presented in this report begins

PNNL's test and evaluation plan [3] for the FEUM prototypes is based on the functional requirements and performance targets communicated by the IAEA in its original procurement specifications and prior publications [1]. The test plan developed by PNNL was not intended to be all-encompassing or wholly sufficient for qualification of the FEUM prototypes by the IAEA, but rather, an initial evaluation to help inform the IAEA about the suitability of the Bot Engineering implementation, and the feasibility of the FEUM concept more generally. Details of each test, including the experimental configurations and settings used by PNNL [3] and not repeated here. This report is focused on the testing data, interpretation, findings and recommendations.

5 RESULTS

The set of tests described below fall into two general categories: functional and performance. Functional testing by PNNL analyzed basic electronics characteristics of the prototypes, for example, gain and discriminator linearity, shaping amplifier characteristics, and dead-time behavior. Performance testing was focused on the ability of the FEUM devices to perform reliably and with sufficient contrast between signal and noise to support the IAEA's often demanding deployment applications (e.g., high neutron count rates in an intense gamma-ray background). Performance testing was conducted in baseline scenarios (ideal conditions) and also in "noisy" electromagnetic (EM) and high-radiation environments to represent typical IAEA facility conditions. For all tests, the FEUM prototype was stimulated by one or more of four input signal types: an AWG that produces a tail-pulse signal generally representative of radiation sensors, ^{3}He proportional counters, ^{235}U fission chambers and NaI(Tl) gamma-ray detectors. The AWG provided a well-characterized, baseline input for functional tests, and idealized outputs to serve as reference in performance tests. The three detector types are commonly used by the IAEA in unattended instruments and provided an indication of how the FEUM prototypes may perform in common IAEA deployments. Other configuration variations were tested in order to observe FEUM performance in a variety of scenarios. These included RG-174 and RG-71 cables ranging from 12cm to 100m in length and FEUM configuration parameters of analog shaping time (τ), discriminator threshold, and digital pulse width (PW). Digital pulse width is also referred to as TTL pulse width in this report. FEUM signals and performance were measured using common nuclear test equipment as shown in Figure 5.1. Section numbers listed in the following results refer to the test procedures as documented in the test plan [3].

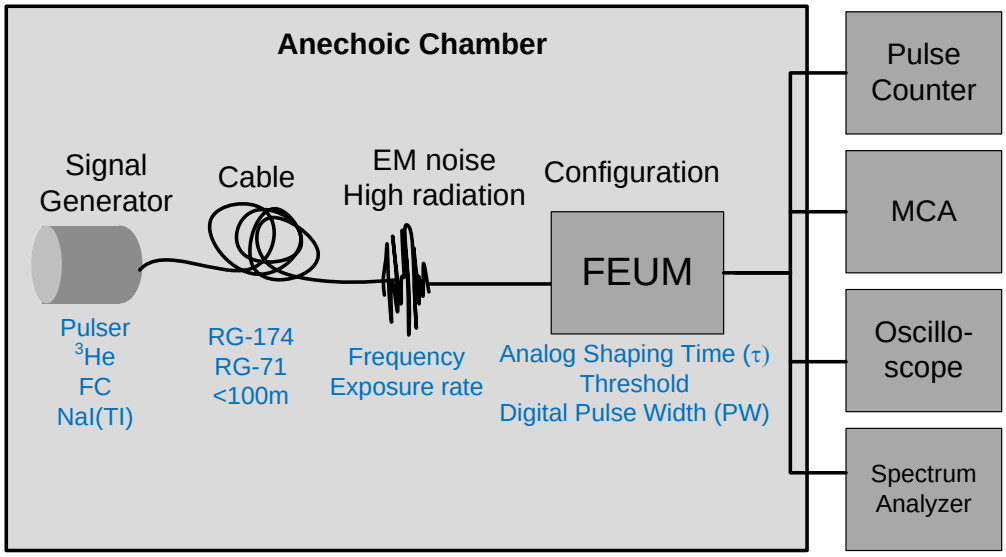

Figure 5.1 Generalized diagram for the configurations used during FEUM prototype testing. Parameters in blue were varied for performance testing scenarios.

Figure 5.2 shows a photo of the FEUM v1.1 device. In the results presented following, the DUT is assumed to be the FEUM v1.1 from Bot Engineering, unless otherwise explicitly stated.

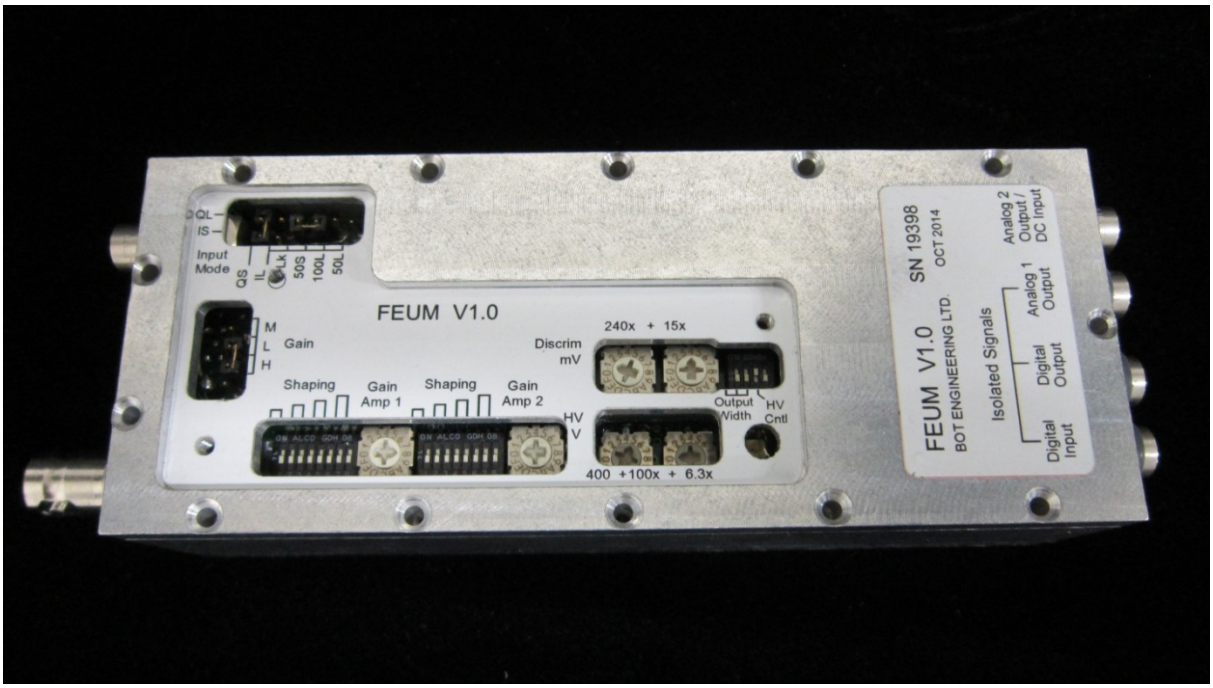

Figure 5.2 FEUM v1.0/v1.1 device.

Test 1: FEATURE CONFORMANCE VERIFICATION

Test 1 compares the basic functional specifications from the IAEA [2] to the specifications of the as-delivered devices tested by PNNL. A summary of the various specifications compared is given in Table 5.1.

Table 5.1 IAEA's FEUM requirements and comparison to manufacturer specifications or PNNL investigation of DUT (grey shading indicates a departure that may be viewed as significant to the IAEA).

	IAEA Requirement	Specification
Preamplifier		
Front-End Sensitivity	Charge-sensitive and current-sensitive	Charge-sensitive and current-sensitive
Rise Time	< 20 ns at C_{ext} = 0 pF, < 50 ns at C_{ext} = 100 pF	Not specified in documentation and not tested (see discussion below)
Shaping Amplifier		
Shaping Configuration	Bipolar (CR^2-RC) shaping	Not specified in documentation; no detailed schematic provided; unable to determine from visual inspection of circuit board. Inspection of output signal indicates consistency with requirement.
Analog Shaping Time	Internally adjustable to discrete settings. Nominal range: 50 ns to 2 µs.	Internally adjustable to discrete settings. Range: 100 ns to 2.4 µs
Gain	Internally adjustable to discrete settings. Nominal range: 1000 V/pC to 0.2 mV/pC.	Internally adjustable to discrete settings. Range: 70 V/pC to 1.9 mV/pC
Output Amplitude	Nominal range: 0 to 0.9·V_{cc}.	Range: 0 to 5V
Output Configuration	Analog signal superimposed on V_{cc} and decoupled from V_{cc}.	Analog signal superimposed on V_{cc} and decoupled from V_{cc}
Discriminator		

Lower Level Discriminator	Externally adjustable to discrete settings. Nominal range: 0 to $0.9 \cdot V_{cc}$.	Internally adjustable to discrete settings. Range: 0 to 3.825V.
Output Pulse Width	Internally adjustable to discrete settings. Nominal range: 50 ns to 500 ns.	Internally adjustable to discrete settings. Range: 50 ns to 2 µs.
Bias Supply		
Voltage Range	Internally adjustable in increments no greater than 50 V. Nominal range:+200 V to +2000 V.	Internally adjustable increments of 6.25 V. Range:+400 V to +2000 V.
Noise	Nominal: 20 mV root-mean-square (RMS) over entire operating range	Charge-sensitive (at gain of 70 V/pC) 0 pF : 10 mV RMS 10m RG-71 : 32 mV RMS 100m RG-71 : 50 mV RMS Current-sensitive (190 V/mA) 0 pF : 8.5 mV RMS 10m RG-71 : 8.5 mV RMS 100m RG-71 : 8.5 mV RMS 300m RG-71 : 8.5 mV RMS
Stability	Nominal: 0.05 V/hour over operating range	Not specified in documentation
Protection	Bias protection network for HV transients	Notional diode protection with no specified quality of protection
Output Impedance	No requirement	Internal adjustment. Range: 330 KΩ to 10 MΩ.
Connectors		
Detector	SHV type consistent with NEMA Standard IP-62	SHV specified in documentation. Conformance to NEMA IP-62 not specified
Other Signal Inputs	LEMO HGP.00.250	ERA.00.250 specified in documentation. Functionally equivalent to HGP
Power Input	LEMO HGP.00.302	ERA.00.302 specified in documentation. Functionally equivalent to HGP
Output	LEMO HGP.00.250	ERA.00.250 specified in documentation. Functionally equivalent to HGP
Power Requirements		
Voltage	+9 VDC to +13.8 VDC	Isolated input, voltage isolation-enabled[1]: +8 VDC to +16 VDC[2]
		Isolated input, voltage isolation-bypassed: +10.5 VDC to +16 VDC
		Ground-referenced (V_{cc} superimposed) input: +10.5 VDC to +16 VDC
Current	No Requirement	Isolated input, voltage isolation enabled : 9 mA to 19 mA
		Isolated input, voltage isolation bypassed: 21 mA to 31 mA
		Ground-referenced (V_{cc} superimposed): 21 mA to 31 mA
Form Factor		
Material	Polished stainless steel	Matte finish stainless steel
Volume	< 100 cm^3	233 cm^3
Aspect Ratio (Length to Cross Sectional Dimension)	> 2	2.0
Number of Fasteners	4 or fewer to access internally adjustable settings	5
Visible settings	LLD must be externally visible	LLD setting is internal

[1] The FEUM v1.1 has 2 voltage inputs, however the isolated input has a switch with 2 different modes: isolation bypass and isolation enabled. The isolation bypass mode feeds the input voltage directly into the 10.5V internal regulator, similar to the ground-referenced input.

[2] The FEUM documentation lists both 15 VDC and 16 VDC as the upper bound of the input power supply.

Additional observations from Test 1 are given here:

- The supporting documentation provided by the vendor is minimal, which makes comprehensive evaluation of the device more challenging. Provision of more thorough documentation by Bot is recommended.
- IAEA specifications dictated that some frequently used settings (e.g., gain, analog shaping time) are to be externally adjustable without the need to remove a cover plate. This specification is not strictly met in the prototypes—the removal of 3 screws is required to access those settings. However, all key adjustments are accessible during FEUM operation.
- As the reader may observe in Figure 5.2, all of the connections are made on the ends of the device. This feature, although not required, enables ease of mounting and simplified cabling designs, particularly in multi-unit implementation scenarios that are common for the IAEA.
- The jumper for the charge gain setting may be a problem in the field as it could be easily dropped and lost. Switches may prove to offer a more robust field design.
- There is no evidence of an environmental seal around the connectors, on the cover plate or between the main body and the two covers. This will most likely fail a moisture intrusion test, though such a test was outside the scope of this project and may not be critical to the IAEA.

Test Result: Pass (with caveats). The DUT departs from the IAEA specifications for several features/functions. Input from the IAEA is needed to determine whether these departures are critical to efficacy in UMS deployments.

Test 2: Pulse Rise Time – Section C.1

This test was not conducted because it would require access to an internal test point that is not readily available in the DUT, and the evaluation of the preamplifier at this intermediate stage was deemed of limited value in comparison to the investigation of the amplifier output, as discussed below.

Test Result: Not Performed.

Test 3: Shaping Amplifier - Gain and Charge Calibration – Section C.2

This test is used to evaluate accuracy and linearity of the gain control. As described in the procedures section of the Test Plan [3], an AWG is the signal source. The AWG produces a voltage ramp that is propagated through a precision capacitor and into the detector input of the DUT. The pulse presented to the DUT charge-sensitive preamplifier is approximately 100ns in width. This pulse width is somewhat shorter than the typical charge evolution times in He-3 and NaI sensors (approximately a few hundred nanoseconds for the majority of charge collection). This means that the gain relationships presented here for the AWG are not necessarily identical to those that would be produced by He-3 and NaI sensors producing the same total amount of charge (due to ballistic deficit and other effects). The settings used for this test are shown in Table 5.2.

Table 5.2 DUT settings used for Test 3.

Parameter	**Setting**	**Value**
HVH - High Voltage	0	400 V
HVL - High Voltage	0	
G2 – Gain	0	1
G3 – Gain	0	
DH – Discriminator High	0	60 mV
DL – Discriminator Low	4	
SW4 – TTL Pulse Width	001	200 ns
Charge Gain	L	1.9-68 mV/pC

SW1 - Shaping Time	00000000	0.1 us
SW2 – Shaping Time	00000000	

The waveform from the AWG prior to the precision capacitor (shown in violet below) and after the precision capacitor (shown in yellow below) are shown in Figure 5.3, Figure 5.4, and Figure 5.5. The capacitor output waveform is a negative tail pulse with a fast leading edge and slow trailing edge. The leading edge exhibits some high frequency (~80 MHz) ringing, but this noise is generally outside of the bandwidth of the preamplifier (<10 MHz) and therefore, does not propagate through to the output. This filtering effect is illustrated in the screen capture of the bandwidth-limited oscilloscope interrogation in Figure 5.5..

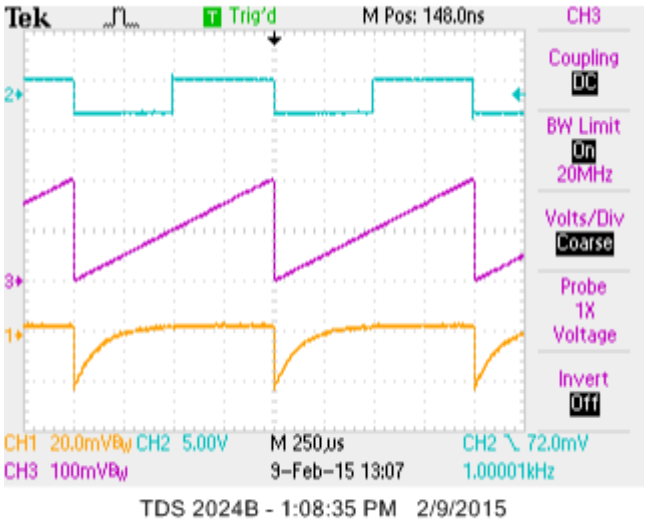

Figure 5.3 AWG and capacitor waveforms for multiple pulses (250 µs per time division). Yellow(1)-Capacitor Output, Blue(2)-AWG Sync Signal, Magenta-AWG Waveform Output.

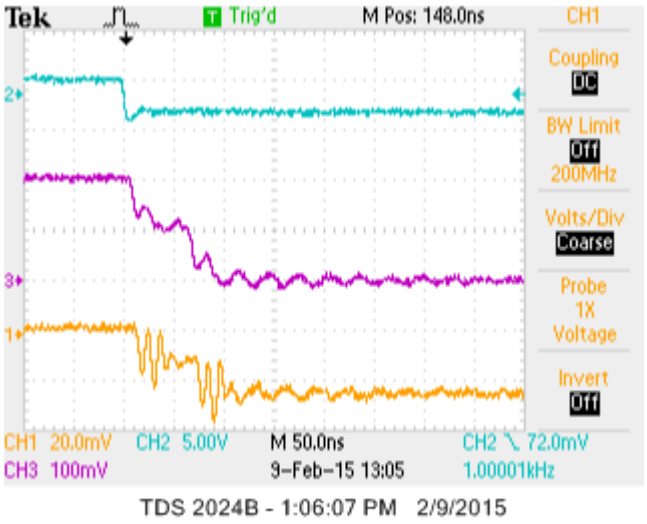

Figure 5.4 AWG and capacitor waveforms for the rising edge of a single pulse (50 ns per time division). Yellow(1)-Capacitor Output, Blue(2)-AWG Sync Signal, Magenta(3)-AWG Waveform Output.

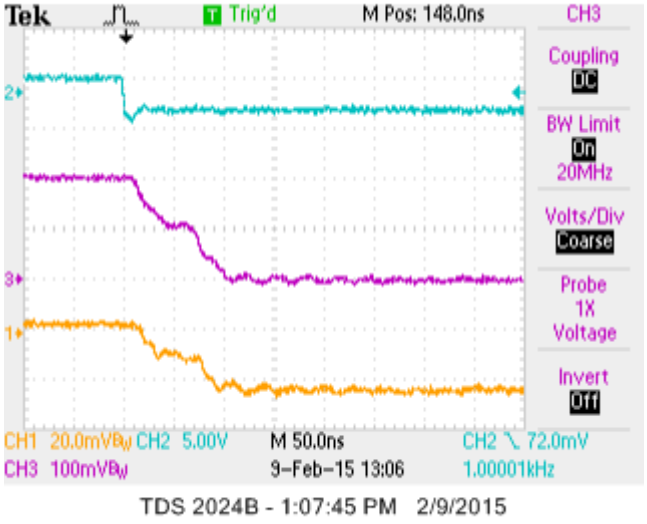

Figure 5.5 AWG and capacitor waveforms for rising edge of single pulse (50 ns per time division), with 20 MHz bandwidth on the oscilloscope (as compared to 200 MHz in Figure 5.4). Yellow(1)-Capacitor Output, Blue(2)-AWG Sync Signal, Magenta(3)-AWG Waveform Output.

The gain linearity curves for both analog output 1 and output 2 for three gain settings are shown in Figure 5.6 through Figure 5.8 The pulse height values tabulated for the figures below were determined by averaging 128 pulses on an oscilloscope over 45 different gain settings; analog 1 output had a 100 Ω terminator. Note that the DUT maximum gain setting of 70 V/pC was not tested.

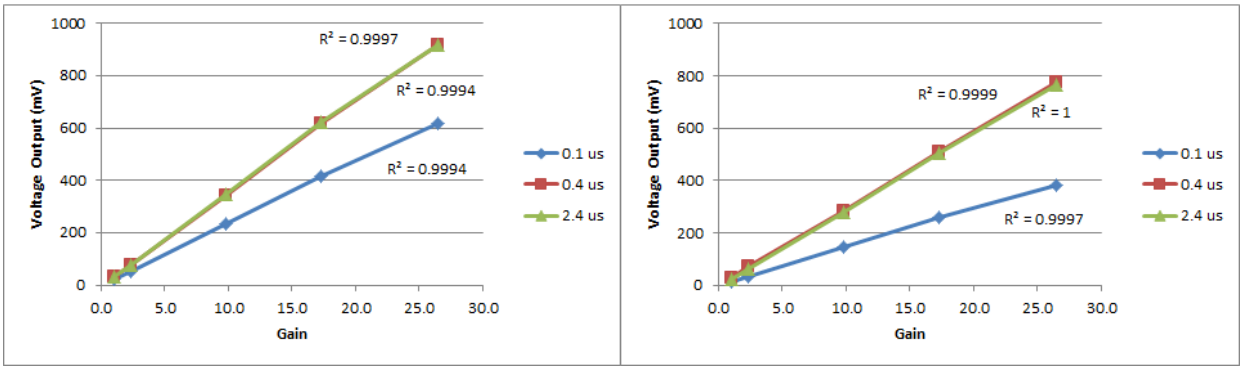

Figure 5.6 Gain linearity curves for the DUT low gain range, using analog shaping times of 0.1 µs, 0.4µs, and 2.4µs. Analog output 1 (left) and analog output 2 (right).

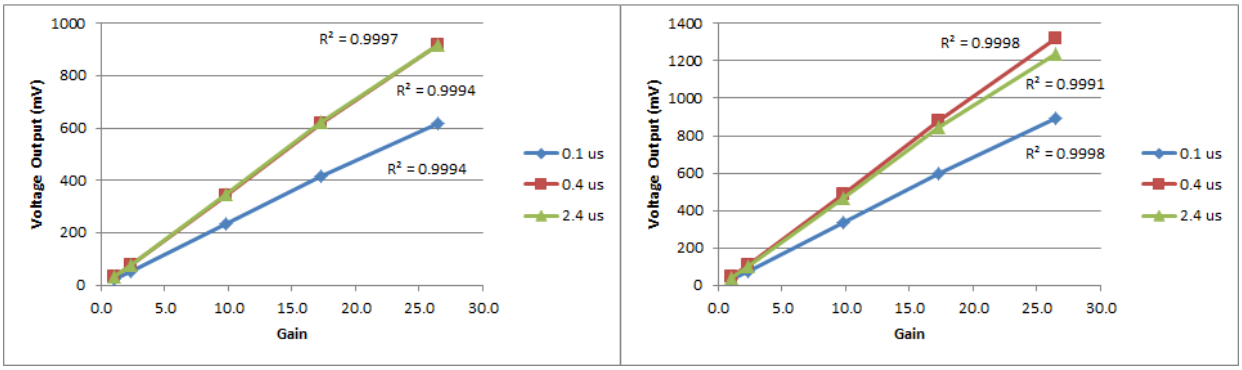

Figure 5.7 Gain linearity curves for the DUT medium gain range, using analog shaping times of 0.1 µs, 0.4µs, and 2.4µs. Analog output 1 (left) and analog output 2 (right).

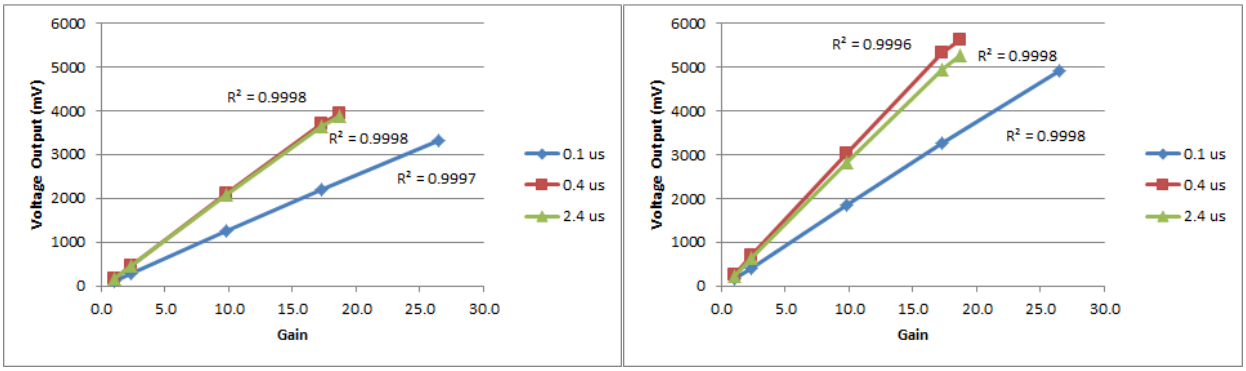

Figure 5.8 Gain linearity curves for the DUT high gain range, using analog shaping times of 0.1 µs, 0.4µs, and 2.4µs. Analog output 1 (left) and analog output 2 (right).

The “Charge vs. Pulse Height” graphic in Figure 5.9 provides confirmation of the stated gain values using nominal parameters (per DUT documentation) of 0.81V/pC gain and 0.4µs shaping time: the measured gain on output Analog 1 is ~0.9 V/pC, and for Analog 2 the gain is ~0.7 V/pC. These values effectively bracket the vendor’s asserted gain value for that particular gain setting

(0.81 V/pC) and therefore, they semi-quantitatively confirm the veracity of the gain values quoted by the vendor. As shown in Table 5.3, however, the specified and as-measured gain values may differ significantly depending on the shaping time and gain range. Note that the specified-to-measured gain ratio is expected to be similar for all shaping times for a given gain range and analog output channel. While the values for 0.4 and 2.4 μs shaping times are similar, the ratios for 0.1 μs shaping time are somewhat higher. This indicates that there is indeed some degree of ballistic deficit occurring at very short shaping times for the ~100-ns input pulse, thereby reducing the measurement pulse height compared to the expected value.

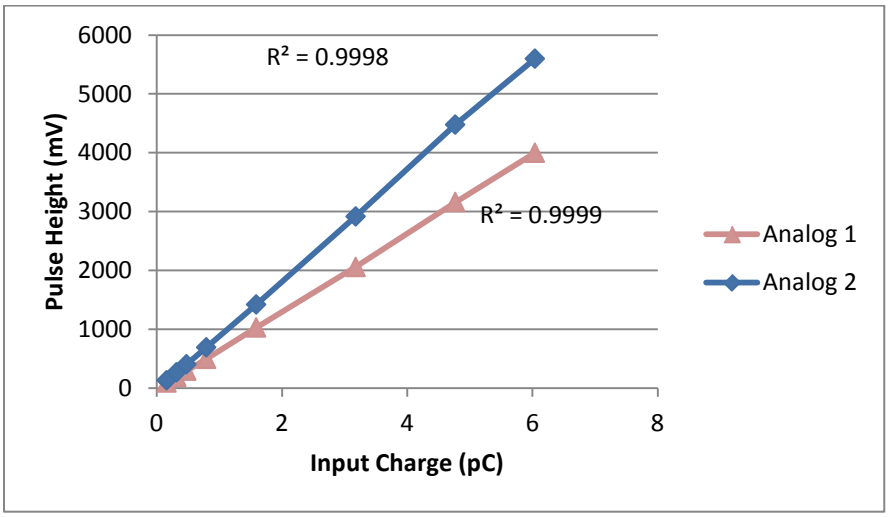

Figure 5.9 Example of absolute charge calibration for a specific nominal gain setting (0.81 V/pC) and analog shaping time (0.4 μs).

Table 5.3 Specified-to-measured gain ratio over various analog shaping times and gain settings.

Manufacturer Specified Gain to Measured Gain Ratio						
Gain Jumper	**Low**		**Medium**		**High**	
Output	**Analog 1**	**Analog 2**	**Analog 1**	**Analog 2**	**Analog 1**	**Analog 2**
Shaping Time (μs)						
0.1	4.17	2.82	2.06	1.42	2.43	1.67
0.4	2.05	1.43	1.40	0.98	1.46	1.02
2.4	2.01	1.49	1.40	1.04	1.49	1.10

The charge versus pulse height data in Figure 5.9 is an example of the data needed to determine the mapping between the amount of charge presented to the DUT input, and the amplitude of the bipolar output pulse, for each gain and shaping-time combination. This mapping provides the conversion coefficients used to support the analysis of differential pulse height spectra (see Test 19) and equivalent noise charge (ENC) analysis (see Test 24). These coefficients, given in units of V/pC for three gain values are tabulated in Table 5.4. As noted in the discussion of Table 5.3, the conversion coefficients for the shortest shaping time is skewed because all of the AWG charge input is not being collected. To prevent this test-specific bias from propagating through the analysis of detectors with different pulse shape and timing characteristics than the AWG used in this test, a nominal conversion coefficient was defined for each gain value. These nominal conversion coefficients, as used in the quantitative charge analysis reported later in this document, are given in the last row of Table 5.4.

Table 5.4 Measured gain ratio of analog output pulse height (V) to input charge (pC) for various analog shaping times and gain settings.

	Gain Range (V/pC)		
Shaping Time (μs)	**L (1.9 mV/pC Nominal)**	**M (60 mV/pC Nominal)**	**H (1900 mV/pC Nominal)**
0.1	0.672	40.8	1030
0.4	1.27	57.9	1660
2.4	1.18	51.8	1520

Test Result: Pass (with caveats). The measured gain values at three different settings are consistent with the vendor-asserted values, but the range of absolute gain provided by the DUT is not as broad (at the high or low end) as that specified by the IAEA.

Test 4: ANALOG SHAPING CONSTANT – SECTION C.2

This test is used to evaluate the functionality and accuracy of the analog shaping time controls. The AWG generated a 500 mV, 1 kHz ramp with 2.2 nF precision capacitor (as depicted in Figure 5.3) to produce the input pulses to the DUT. Analog shaping times (τ) of 0.1 μs, 0.2 μs, 0.4 μs, 1.2 μs and 2.4 μs were used. These are the specific analog shaping times referenced in the Bot documentation, although other intermediate values are possible through the use of provided dual in-line package DIP switches.

Table 5.5 DUT settings used for Test 4.

Parameter	**Setting**	**Value**
HVH - High Voltage	0	400 V
HVL - High Voltage	0	
G2 – Gain	0	1
G3 – Gain	0	
DH – Discriminator High	1	360 mV
DL – Discriminator Low	8	
SW4 – TTL Pulse Width	001	200 ns

The data of Figure 2.7 indicate that the output bipolar pulse shape and duration is consistent with expectations in absolute and relative terms, for a given value of τ. Assuming a standard analog, bipolar shaping method (i.e., CR^2-RC^n, [Ref = Knoll]) in which τ for each analog stage is equivalent, the total bipolar pulse width (i.e., rising edge to trailing edge of second lobe) is expected to be approximately 2×τ. The DUT exhibits this behavior, and the relative deviation from the expected values is reasonably consistent over the full range of analog shaping times (as evidenced by the high correlation coefficients for both charge- and current-sensitive modes.

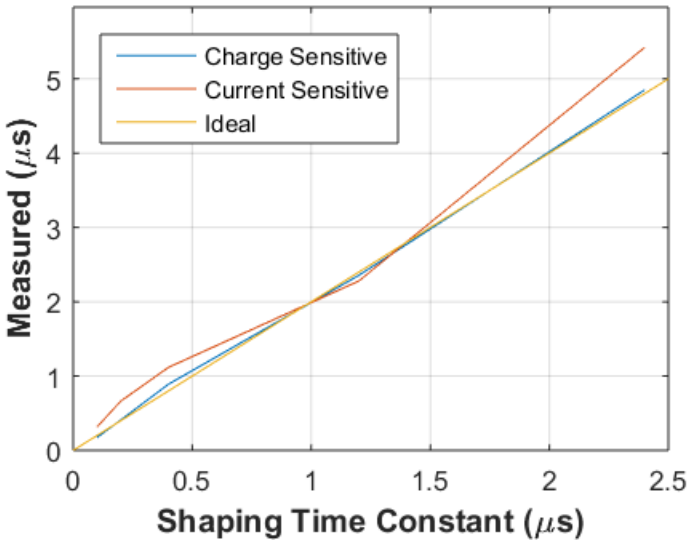

Figure 5.10. Relationship between measured duration of the bipolar output pulse width and the user-defined analog shaping time constant (τ).

Test Result: Pass. The measured pulse durations for both charge- and current-sensitive modes, as a function of τ, *are consistent with theoretical prediction over the full range of* τ *variability.*

Test 5: Discriminator Threshold – Section C.3

This test is used to evaluate linearity and absolute accuracy of the discriminator control. Nominal discriminator settings were varied from 60 mV to the top of the available range, 3.84 V. The DUT for this test was the original FEUM prototype and not FEUM v1.1. The settings for this test are listed in Table 5.6.

Table 5.6 DUT settings used for Test 5.

Parameter	**Setting**	**Value**
HVH - High Voltage	0	400 V
HVL - High Voltage	0	
SW1 - Shaping Time	000011	0.08 μs
SW2 - Shaping Time	001100	
G2 – Gain	0	1
G3 – Gain	0	
SW4 – TTL Pulse Width	0010	1800 ns

For each discriminator setting, the AWG input voltage, nominal discriminator threshold (in V, per device settings) voltage, and corresponding MCA bin (scaled to units of voltage) were measured. The left pane of Figure 5.11 illustrates the relationship between nominal and measured discriminator voltage level. The linearity of the discriminator control, as measured against a best-fit line through the data, has a linear correlation coefficient over the entire range of more than 0.999. While the absolute accuracy of the threshold is relatively good below approximately 2V, significant offsets from the nominal setting (approaching 10%) are evident at the top end of the ~3-4V range (right pane of Figure 5.11). The data presented for this test were acquired using the initial DUT. The test was not repeated using FEUM v1.1.

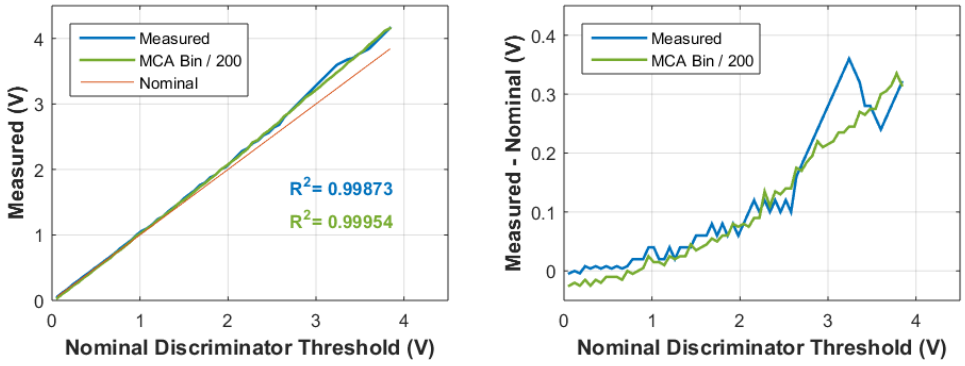

Figure 5.11 Linearity (left) and absolute accuracy (right) of the DUT discriminator. The "Nominal" line in the left pane represents the expected behavior; the offset in the right pane is the difference between the measured and nominal. The best-fit line in the left pane is used to evaluate the linearity of the discriminator.

Test Result: Inconclusive. Input from the IAEA is needed to determine whether the relatively low degree of linearity and relatively high offset at the top of the discriminator range voltages is critical to UMS deployments.

Test 6: TTL Pulse Width – Section C.4

This test is used to evaluate the absolute accuracy of the TTL pulse-width controls. Four pulse-width settings were tested, three times each. The standard deviation of the redundant tests was no more than 4.4 ns for any setting. The DUT settings used for this test are given in Table 5.7.

Table 5.7 DUT settings for Test 6.

Parameter	**Setting**	**Value**
Charge Gain	H	1.9-70 V/pC
G2 – Gain	0	1
G3 – Gain	0	
HVH - High Voltage	4	800 V
HVL - High Voltage	0	
SW1 - Shaping Time	00000011	2.4 µs
SW2 - Shaping Time	00000011	
DH – Discriminator High	1	360 mV
DL – Discriminator Low	8	

The results of the TTL pulse-width tests are given in Figure 5.12. The linearity of the TTL pulse-width control, as measured against a best-fit line through the data, is high with a linear correlation coefficient greater than 0.99. The absolute accuracy is relatively good at all tested values with no significant offsets.

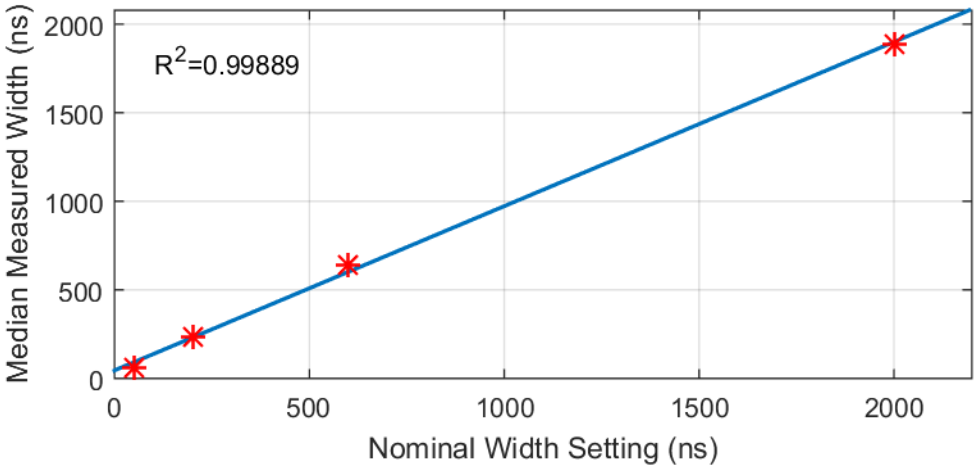

Figure 5.12 TTL pulse width linearity.

The basic functional tests for the TTL output produced a positive finding, however data gathered during the course of the dead time measurements (Test 23) revealed a potential issue. A time-interval histogram method provides a more comprehensive evaluation of the TTL output characteristics, as shown in Figure 5.13. The expected behavior in these histogram plots is a very narrow peak centered at the user-defined pulse width value. This behavior was exhibited for all tested combinations of digital and analog pulse width, except for those involving the longest digital pulse width (2000 ns). The top pane of Figure 5.13 shows the inconsistent behavior of the pulse widths at that setting, including tails that extend to very low values. In addition, the centroid of the main lobe is somewhat different (~1900 ns) than the nominal setting. For the 50-ns setting, the predominant pulse duration is longer than the nominal setting (~70 ns versus 50 ns), but the tails effect is much less pronounced.

The cause of this tailing at longer shaping times is not known for certain, but could be explained by the characteristics of the one-shot timers generally used to create the digital output pulses. The output width is measured using the charge decay of a capacitor. If events occur very close together in time, the capacitor may not have enough time to recharge completely. It would then prematurely trigger the one-shot timer to end the pulse. Further investigation of this behavior, over a wider range of parameter settings, may be warranted but is beyond the scope of this test.

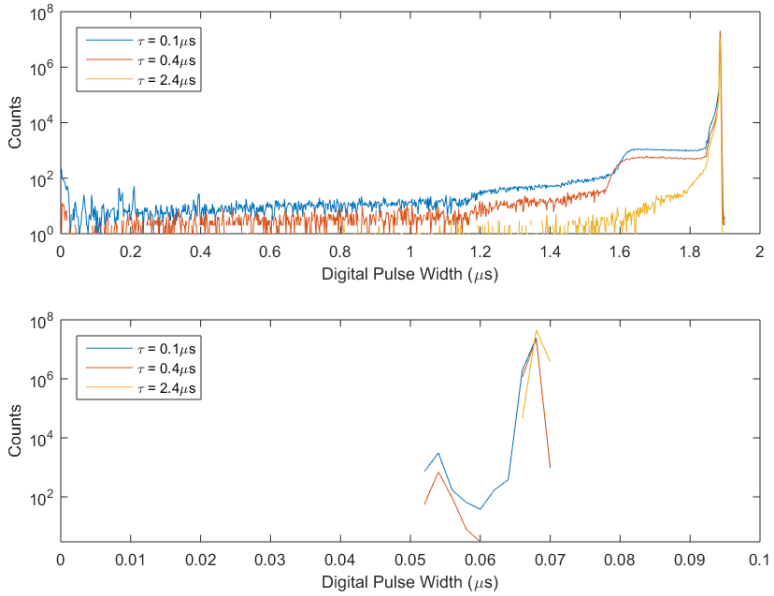

Figure 5.13 Pulse-width histograms for the digital output, for three different analog shaping times (τ = 0.1, 0.4 and 2.4 μs) .Top: Digital pulse width setting of 2000 ns. Bottom: Digital pulse width setting of 50 ns.

Test Result: Pass (with caveats). The DUT has met the basic functional requirements of Test 7, but further investigation may be warranted for long pulse-width settings.

Test 7: BIAS SUPPLY-VOLTAGE – SECTION C.5

This test is used to evaluate the absolute accuracy of the high-voltage controls. Thirty-three settings were used ranging from lowest (400V) to highest (1993.75V) settings supported by the DUT. The tests were conducted using the isolated power supply input. Measurements were taken using a 1000:1 voltage probe with a 3.5 point precision multi-meter, thus voltage values have a resolution of 1 V. The DUT settings for this test are listed in Table 5.8 and the results are given in Table 5.9.

Table 5.8 DUT settings for Test 8.

Parameter	**Setting**	**Value**
HVH - High Voltage	0	400 V
HVL - High Voltage	0	
SW1 - Shaping Time	00000000	0.08 μs
SW2 - Shaping Time	00000000	
G2 – Gain	0	1
G3 – Gain	0	
DH – Discriminator High	0	60 mV
DL – Discriminator Low	4	
SW4 – TTL Pulse Width	001	200 ns

Table 5.9 Comparison of each high voltage setting to the measured high voltage.

Settings (HVH/HVL)	High Voltage Value (V)	Measured (V)	Error (V)	Error (%)
0/0	400 V	389	-11	-2.750%
0/8	450 V	440	-10	-2.222%
1/0	500 V	492	-8	-1.600%
1/8	550 V	541	-9	-1.636%
2/0	600 V	594	-6	-1.000%
2/8	650 V	642	-8	-1.231%
3/0	700 V	695	-5	-0.714%
3/8	750 V	744	-6	-0.800%
4/0	800 V	797	-3	-0.375%
4/8	850 V	844	-6	-0.706%
5/0	900 V	897	-3	-0.333%
5/8	950 V	942	-8	-0.842%
6/0	1000 V	996	-4	-0.400%
6/8	1050 V	1048	-2	-0.190%
7/0	1100 V	1095	-5	-0.455%
7/8	1150 V	1138	-12	-1.043%
8/0	1200 V	1193	-7	-0.583%
8/8	1250 V	1236	-14	-1.120%
9/0	1300 V	1290	-10	-0.769%
9/8	1350 V	1333	-17	-1.259%
A/0	1400 V	1386	-14	-1.000%
A/8	1450 V	1430	-20	-1.379%
B/0	1500 V	1482	-18	-1.200%
B/8	1550 V	1526	-24	-1.548%
C/0	1600 V	1577	-23	-1.438%
C/8	1650 V	1621	-29	-1.758%
D/0	1700 V	1671	-29	-1.706%
D/8	1750 V	1716	-34	-1.943%
E/0	1800 V	1765	-35	-1.944%
E/8	1850 V	1810	-40	-2.162%
F/0	1900 V	1858	-42	-2.211%
F/8	1950 V	1903	-47	-2.410%
F/F	1993.75 V	1944	-49	-2.459%

The results are summarized in the following figure, which plots the high voltage setting versus the as-measured high voltage, and calculates the linearity of that relationship.

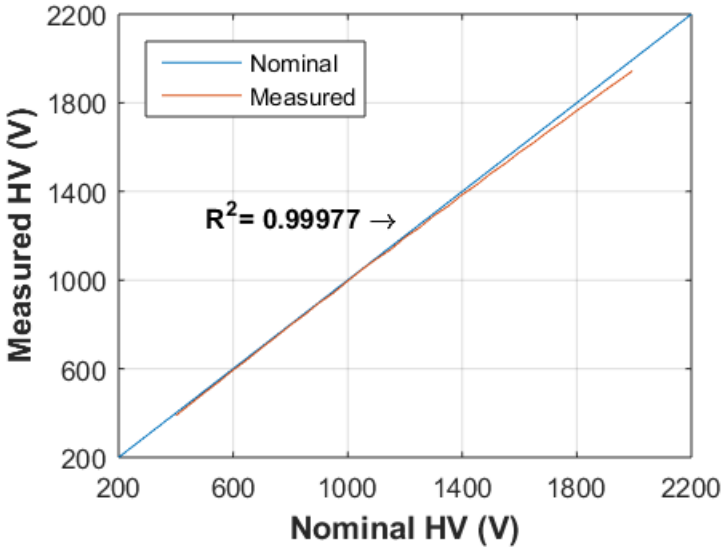

Figure 5.14 High voltage linearity for test 7.

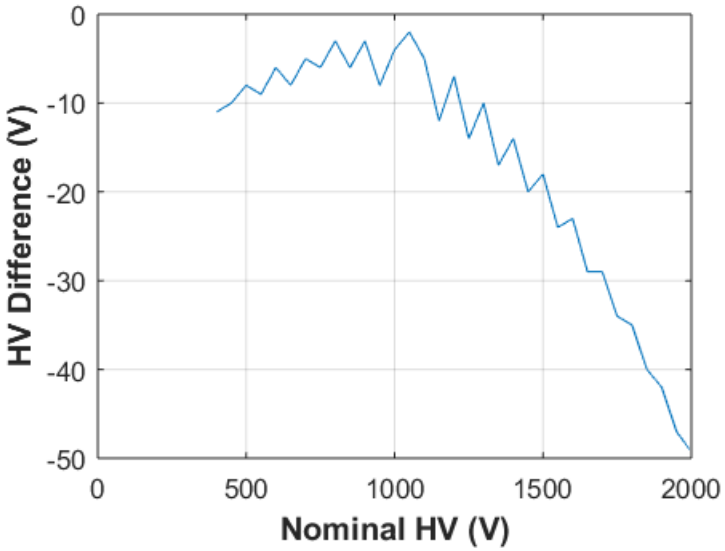

Figure 5.15 Voltage difference between as-measured and nominal (expected) and measured high voltage.

All measured voltages were below the nominal voltage. The average error was −16.91 V with a minimum error of −2 V and maximum error of −49 V. However, the average percentage error was −1.309% with a minimum −0.190% and maximum of −2.750%.

Test Result: Pass (with caveats). The measured versus asserted voltage relationship shows a high degree of linearity but the absolute accuracy progressively degrades as voltage level is increased. It is expected that is accuracy is not problematic for the kinds of sensors utilized by the IAEA, but input from the IAEA is needed on this question.

Test 8: BIAS SUPPLY - STABILITY – SECTION C.6

Full, long-term evaluation of high-voltage stability was not performed because it would have required testing over time periods of weeks to months. A preliminary evaluation using the earliest FEUM prototype, over shorter time scales, was completed. Testing over a 24-hour time period, with a sampling period of 1 second and a nominal value of 400 V yielded a mean value of 399.12 V with a standard deviation of 0.07V.

Test Result: Inconclusive. Longer-term testing, over a range of nominal values and loads, is needed to provide definitive findings on high-voltage stability.

Test 9: INPUT/OUTPUT PORT RESISTANCE – SECTION C.10

This test was not conducted because the original test methods were not practical for all input/output ports. Some ports require the FEUM to be energized and measured in reference to test points which are not available on the FEUM prototype.

Test Result: Not Performed.

Test 10: LED COUNT RATE – SECTION C.4

A visual check confirmed that the LED is functioning properly, in the qualitative sense. No quantitative testing was performed, nor is it considered necessary to evaluate the basic functionality of the LED indicator.

Test Result: Pass.

Test 11: ISOLATED INPUT POWER – SECTION C.7

This test is intended to verify the stability of the high voltage power output and the analog 1 output pulse amplitude as a function of varying supply voltages at the isolated power supply input. The input supply voltage was varied from +8V to +15V and the high voltage output was recorded with at minimum and maximum settings. Similarly, gain responses at maximum, minimum, and median gain settings were recorded at each supply voltage. Other DUT configuration settings used can be seen in Table 5.10 and Table 5.11. The results for stability of the high voltage with varying input voltage are depicted in Figure 5.16.

Table 5.10 DUT settings for Test 11, high voltage verification.

Parameter	**Setting**	**Value**
Charge Gain	L	1.9-68 mV/pC
G2 – Gain	0	1
G3 – Gain	0	
SW1 - Shaping Time	00000000	0.1 μs
SW2 - Shaping Time	00000000	
DH – Discriminator High	1	360 mV
DL – Discriminator Low	8	
SW4 – TTL Pulse Width	001	200 ns

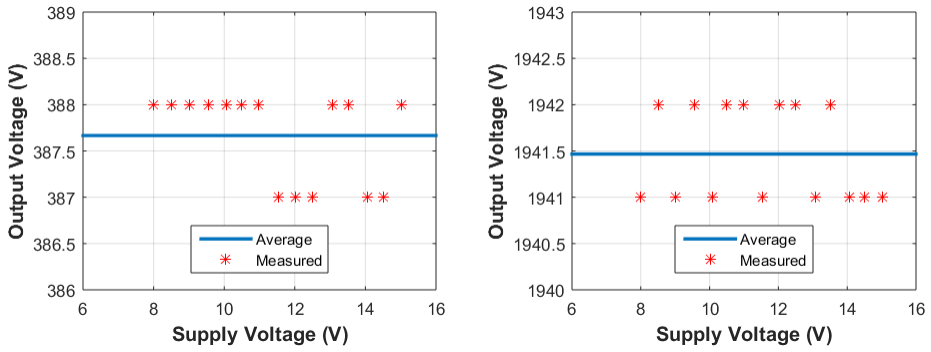

Figure 5.16 High voltage stability as a function of supply voltage. Note that the resolution of the measurement is 1 V.

.

At the minimum setting of 400 V, the measured values had a standard deviation of 0.4880 V, approximately 0.1%. , and a bias of approximately -12 V form the nominal value. At the maximum setting, the measured value had a standard deviation of 0.5164 V, approximately 0.025%, and a bias of approximately -59 V from the nominal value. These relatively large bias values are discussed more fully in Test 7. Given the types of sensors typically used by the IAEA for counting applications, this HV stability is deemed adequate.

For gain response as a function of supply voltage at the isolated supply input, DUT settings can be seen in Table 5.11. The input pulses were generated using the AWG ramp with amplitude of 10 mV and a 2200 pF precision capacitor, similar to test setups described previously. The analog output amplitude was stable across the isolated input supply range.

Table 5.11 DUT settings for Test 12, gain response.

Parameter	**Setting**	**Value**
Charge Gain	L	1.9-68 mV/pC
G2 – Gain	0	1
G3 – Gain	0	
SW1 - Shaping Time	00000011	2.4 µs
SW2 - Shaping Time	00000011	
DH – Discriminator High	1	360 mV
DL – Discriminator Low	8	
SW4 – TTL Pulse Width	001	200 ns

Table 5.12 Stability of gain as function of supply voltage. Values in parentheses after the pulse amplitude are the percent differences from the mean, over the three different supply voltages.

	Relative Gain ->	**1**	**13.44**	**36**
Test #	**Supply Voltage (V)**	**Analog Output Amplitude (mV)**		
1	8.0	18.8 (-4.1%)	256 (-3.3%)	648 (-3.3%)
2	11.5	20 (2.1%)	268 (1.2%)	680 (1.4%)
3	15.0	20 (2.1%)	270 (2.0%)	684 (2.0%)

Test Result: Pass. The deviation in high voltage and gain due to varying input voltage is minimal and is not expected to impact the operation of typical UMS sensors operated in counting mode.

Test 12: DIGITAL INPUT - LOGIC VOLTAGE LEVELS – SECTION C.8

This test is to verify that the input logic high (V_{IH}) and low (V_{IL}) levels are compliant with 5-V TTL logic. The DUT settings used are listed in the table below. Standard TTL logic levels are displayed in Table 5.14.

Table 5.13 DUT settings for Test 12.

Parameter	**Setting**	**Value**
Charge Gain	M	0.06-2.2 V/pC
G2 – Gain	0	1
G3 – Gain	0	
HVH - High Voltage	0	400 V
HVL - High Voltage	0	
SW1 - Shaping Time	00000011	2.4 µs
SW2 - Shaping Time	00000011	
DH – Discriminator High	1	360 mV
DL – Discriminator Low	8	
SW4 – TTL Pulse Width	001	200 ns

Table 5.14 Standard TTL logic levels.

Mode	Logic Low		Logic High	
	Minimum (V)	Maximum (V)	Minimum (V)	Maximum (V)
(input)	0	0.8	2.0	5
(output)	0	0.5	2.7	5

The TTL output is transformer-coupled and therefore, measuring V_{IL} from circuit ground is not applicable (i.e. measurements are the delta between the signal and ground output). Because this input is transformer-coupled, the device is reading a differential voltage referenced only to the FEUM circuit ground. Therefore it is not possible to determine at what point the DUT's input circuit would stop registering logic lows, i.e. the DUT doesn't have an exact cutoff voltage.

A 25 kHz input rate, with TTL pulses having varying amplitudes, was used to evaluate the sensitivity of recorded count rate to TTL voltage level. As Table 5.14 indicates, the recorded count rate is highly variable for voltages below 1.8V, apparently due to the generation of multiple output TTL pulses per input pulse. For pulse amplitudes above 1.8V, the recorded output rate is quite stable and as expected in the absolute sense. For example, the average recorded rate was 25.4829 kHz for 5-V amplitudes.

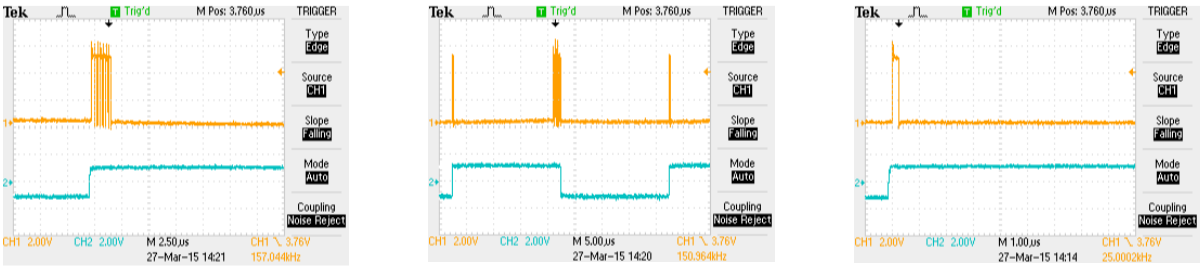

Figure 5.17 Digital input and output pulses for 1.1V input (left), 1.174V input (center) and 1.18V input (right). The input signal is in blue and the output response in yellow. Note the multiple output pulses that occur for TTL input pulses below 1.18V.

Table 5.15 Count rates (kHz) for various digital input voltages, for an input pulse rate of 25 kHz.

1.09 V	1.1 V	1.173 V	1.174 V	1.18 V	5 V
0 kHz	145.7856 kHz	50.9998 kHz	28.7658 kHz	25.2827 kHz	25.4829 kHz

As there is to be no guarantee of how a TTL device will operate in the region between 0.8 V and 2 V (and our required TTL high level is 2.4 V), this should not be considered a problem, but rather should be noted in the event a significant increase in counts occurs, the logic levels may need to be assessed if its known that received logic levels are near the 2 V threshold.

Test Result: Pass. The measured pulses for logic levels above the threshold are consistent with expectations.

Test 13: DIGITAL INPUT - DIGITAL SUMMING – SECTION C.8

This test is to verify that the digital summing function works correctly, such that pulses presented at the detector input and the digital input are properly summed and presented to the digital output. The DUT settings for this test are listed in Table 5.16.

Table 5.16 DUT settings for Test 13.

Parameter	**Setting**	**Value**
Charge Gain	M	0.06-2.2 V/pC
G2 – Gain	0	1
G3 – Gain	0	
HVH - High Voltage	0	400 V
HVL - High Voltage	0	
SW1 - Shaping Time	00000011	2.4 μs
SW2 - Shaping Time	00000011	
DH – Discriminator High	1	360 mV
DL – Discriminator Low	8	
SW4 – TTL Pulse Width	001	200 ns

The test configuration for verifying digital summing functionality is shown in Figure 5.18, and consists of two random pulse generators (RPG) to the DUT's detector and digital inputs. Each random pulse generator was used to present pulses at rates ranging from approximately 100 cps to 1 Mcps. Count rates were measured for each RPG output and the DUT output, over a 60-second period. A set of 3 measurements was taken when presenting only to the detector input, only to the digital input, and then simultaneously. Figure 5.19 and Figure 5.20 show representative input pulses for the detector input and digital input respectively.

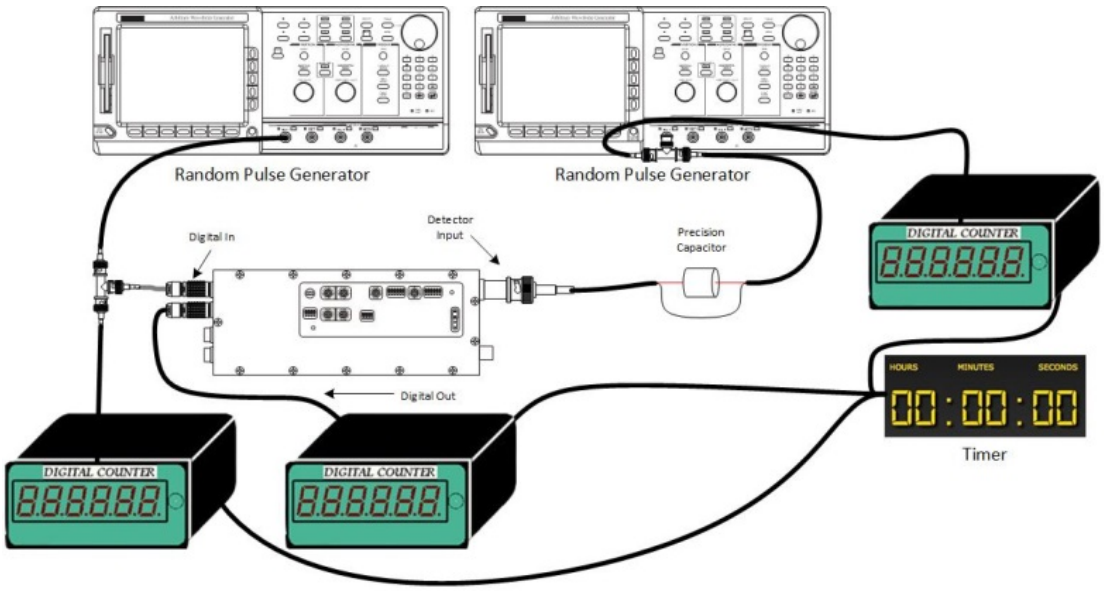

Figure 5.18 Simple summing setup for verifying digital input summing functionality.

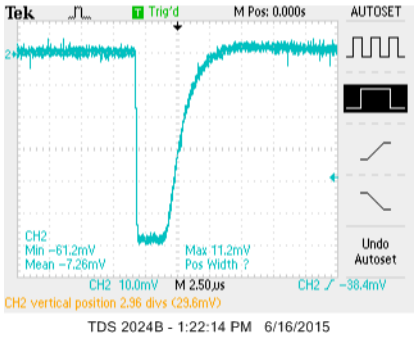

Figure 5.19 Example of signal presented to the detector input.

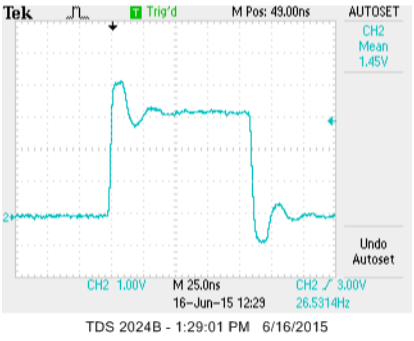

Figure 5.20 Example signal presented to the digital input.

The results of the digital summing test are presented in Table 5.17 below for a TTL pulse width setting of 200ns.

Table 5.17. Digital summing results for a range of input rates presented to the detector and digital inputs. TTL pulse width is 200ns for all cases. The relative difference (%) between the ideal and observed output rates are given parentheses.

Average Counts (kcps)	Detector Only		Digital Input Only		Simultaneous Inputs			
	Input rate (kcps)	Output rate (kcps)	Input rate (kcps)	Output rate (kcps)	Detector input rate (kcps)	Digital input rate (kcps)	Ideal summed rate (kcps)	Output summed rate (kcps)
0.1667	173	173 (0%)	201	200 (0%)	173	202	375	374 (-0.267%)
1.67	1699	1680 (-1.12%)	2013	2013 (0%)	1703	2013	3717	3694 (-0.619%)
10	11216	10627 (-5.25%)	10751	10743 (0%)	10796	10727	21523	21162 (-1.677%)
100	96302	90447 (-6.08%)	114763	113644 (-0.97%)	98313	109003	207316	199436 (-3.801%)
1000	982856	881526 (-10.31%)	866928	761009 (-12.21%)	1087355	866828	1954183	1351229 (-30.86%)

The data in Table 5.16 indicates that the digital summing function of the DUT is performing as expected for rates of approximately 100 kcps on each input. The output rates for those cases are consistent with expectations for dead-time effects on the individual outputs, and the relative difference for the observed summed rate is bracketed by the differences on each input. For the highest rate tested, however, the observed summed rate exhibits a much larger relative decrease that does either input acting independently.

Test Result: Inconclusive. At input rates approaching 1 Mcps at the detector and digital input, significant departures from the expected summed rates were observed. More investigation is needed to determine whether this behavior is to be expected, given the design of the device, and whether IAEA uses of FEUM devices would be compromised by this behavior.

Test 14: GROUNDED INPUT POWER – SECTION C.7

This test is intended to verify the stability of the high voltage power output and the analog 1 output pulse amplitude as a function of varying supply voltages at the analog 2 power input. The input supply voltage was varied from +10.5V to +15V and the high voltage output was recorded at both minimum and maximum settings. Similarly, gain responses at maximum, minimum, and median gain settings were recorded at each supply voltage. DUT configuration settings used can be seen in Table 5.18 and Table 5.19. The results are presented in Figure 5.16 and Table 5.20.

Table 5.18 DUT settings for Test 14, high voltage verification.

Parameter	**Setting**	**Value**
Charge Gain	L	1.9-68 mV/pC
G2 – Gain	0	1
G3 – Gain	0	
SW1 - Shaping Time	00000000	0.1 μs
SW2 - Shaping Time	00000000	
DH – Discriminator High	1	360 mV
DL – Discriminator Low	8	
SW4 – TTL Pulse Width	001	200 ns

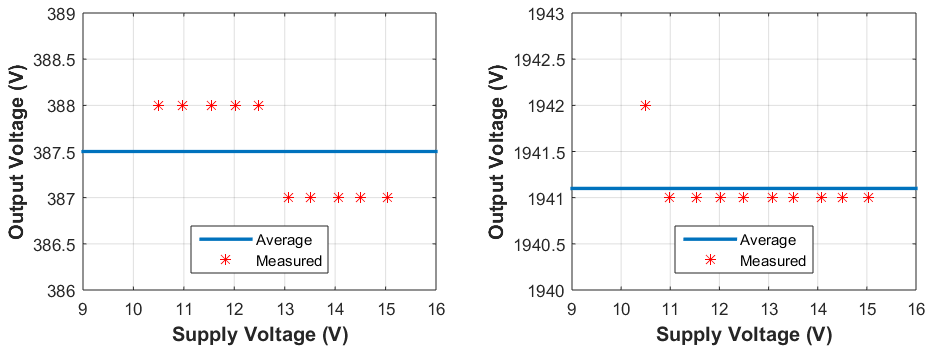

Figure 5.21 High voltage stability vs varied ground referenced power input.

At the minimum setting of 400 V, the measured values had a standard deviation of 0.5270 V, approximately 0.1%., and a bias of approximately -12 V from the expected value. At the maximum setting, the measured value had a standard deviation of 0.3162 V, approximately 0.016%, and a bias of approximately -59 V from the nominal value. These relatively large bias values are discussed more fully in Test 7. Given the types of sensors typically used by the IAEA for counting applications, this HV stability is deemed adequate. Note that the ground-coupled power supply has a higher minimum voltage supply limit of 10.5 V; not all results of Test 11 are compatible for comparison with Test 14.

DUT settings can be seen in the table below for testing gain response to input pulse generated using the AWG ramp with amplitude of 10mV with a 2200pF precision capacitor. The analog output amplitude is stable across the grounded input supply range and is consistent with the results for the isolated input supply range.

Table 5.19 DUT settings for Test 14, gain response.

Parameter	**Setting**	**Value**
Charge Gain	L	1.9-68 mV/pC
G2 – Gain	0	1
G3 – Gain	0	
SW1 - Shaping Time	00000011	2.4 µs
SW2 - Shaping Time	00000011	
DH – Discriminator High	1	360 mV
DL – Discriminator Low	8	
SW4 – TTL Pulse Width	001	200 ns

Table 5.20 Stability of gain as function of supply voltage. Values in parentheses after the pulse amplitude are the percent differences from the mean, over the three different supply voltages.

	Relative Gain ->	**1**	**13.44**	**36**
Test #	**Supply Voltage**	**Analog Output Amplitude (mV)**		
1	10.5	13.6 (-1.5%)	216 (-0.9%)	592 (-3.1%)
2	13.0	13.8 (0%)	218 (0%)	616 (0.8%)
3	15.0	14 (1.5%)	220 (0.9%)	624 (2.2%)

Test Result: Pass. The deviation in high voltage and gain due to varying input voltage is minimal and is not expected to impact the operation of typical UMS sensors operated in counting mode.

Test 15: ANALOG OUTPUT 1 & 2 – SECTION C.9

This test is to verify that the shaping amplifier's output is compatible with interfacing devices by inspecting the output voltage levels and pulse shape and to verify outputs are decoupled or superimposed on (V_{cc}.) This test is also intended to verify that the two outputs are identical except for the DC offset.

For these tests, the power-supply voltage was set to 12V (mid-range) and twenty waveform pairs were captured using an oscilloscope (inputs from Analog #1 and #2), ten while operating on the isolated power input and ten while operating on the ground referenced power input (Analog #2 port). Their pulse widths and amplitudes (minus DC offset) were measured. The DUT settings used for this test are given in Table 5.21.

Table 5.21 DUT settings for Test 15.

Parameter	**Setting**	**Value**
Charge Gain	L	1.9-68 mV/pC
G2 – Gain	0	1
G3 – Gain	0	
HVH - High Voltage	0	000 V
HVL - High Voltage	0	
SW1 - Shaping Time	00000011	2.4 µs
SW2 - Shaping Time	00000011	
DH – Discriminator High	1	360 mV
DL – Discriminator Low	8	
SW4 – TTL Pulse Width	001	200 ns
Detector Source Impedance	330 kΩ	
Precision Capacitor	2200 pF	

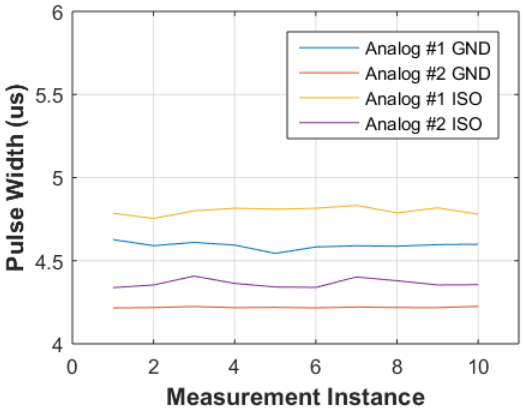

Figure 5.22 Analog #1 & #2 measured pulse widths.

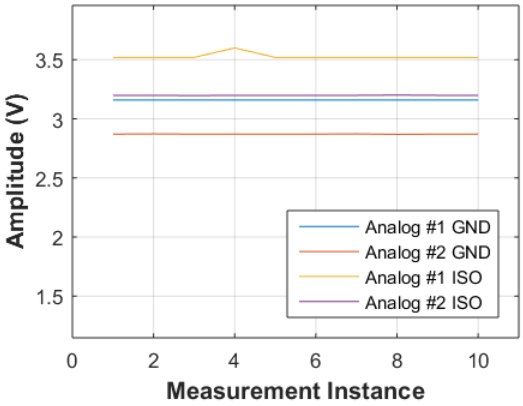

Figure 5.23 Analog #1 & #2 (without DC offset) measured pulse amplitudes.

The pulse widths are stable (maximum standard deviation of 0.02 µs). For both channels the pulse width is slightly wider when powering the DUT via the isolated power supply input. Analog #1 pulse widths are wider than Analog #2, regardless of which power supply used.

The pulse amplitudes are stable (maximum standard deviation of 0.025 V). For Analog #1, the amplitude is approximately 0.33 V greater when powering the DUT via the isolated power supply input. Analog #2, however, has a significant increase in amplitude when powering the DUT via the isolated power supply input vs signal being coupled with power input on Analog #2 port.

Test Result: Pass.

Test 16: Digital Output - Logic Voltage Levels – Section C.4

This test is to verify that the output logic high (V_{OH}) and low (V_{OL}) voltage levels are compliant with 5 V TTL logic. This testing was performed at multiple TTL pulses widths to determine if digital pulse width has any detrimental effects on the DUT's logic-level performance. The DUT settings for this test are summarized in Table 5.22.

Table 5.22 DUT settings for Test 16.

Parameter	**Setting**	**Value**
Charge Gain	H	1.9-70 V/pC
G2 – Gain	0	1
G3 – Gain	0	
HVH - High Voltage	0	000 V
HVL - High Voltage	0	
SW1 - Shaping Time	00000011	2.4 µs
SW2 - Shaping Time	00000011	
DH – Discriminator High	1	360 mV
DL – Discriminator Low	0	
SW4 – TTL Pulse Width	001	200 ns

TTL output is transformer coupled and therefore, measuring V_{OL} from circuit ground is not applicable (i.e. measurements are the delta between the signal and ground output). Standard TTL logic levels are listed in Table 5.23.

Table 5.23 Standard TTL logic voltage levels.

Mode	Logic Low		Logic High	
	Minimum (V)	Maximum (V)	Minimum (V)	Maximum (V)
input	0	0.8	2.0	5
output	0	0.5	2.7	5

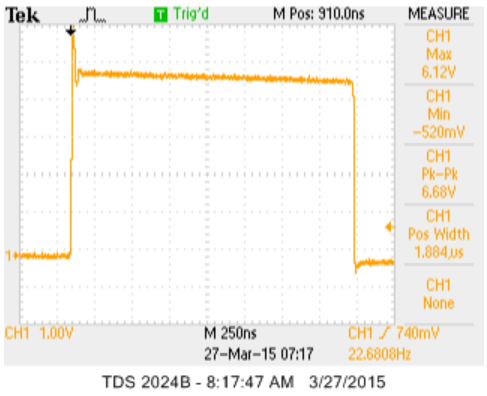

Figure 5.24 Digital output pulse waveform with digital pulse width set to 2000 ns.

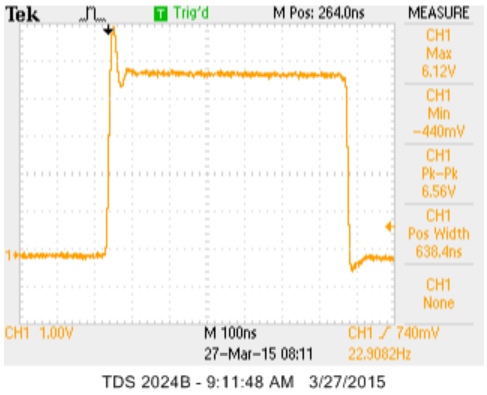

Figure 5.25 Digital output pulse waveform when pulse width set to 600 ns.

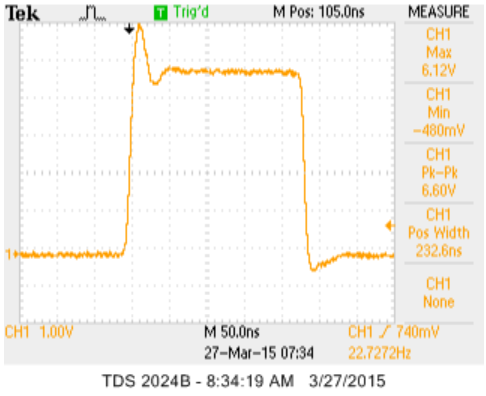

Figure 5.26 Digital output pulse waveform when pulse width set to 200 ns.

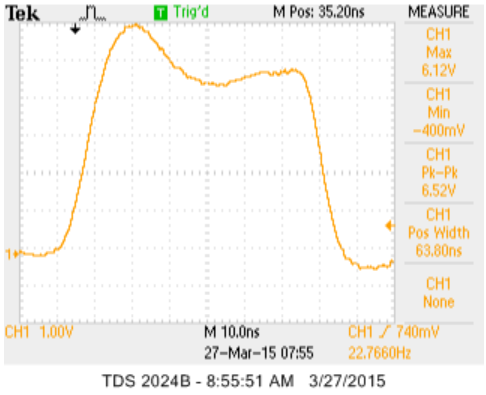

Figure 5.27 Digital output pulse waveform when pulse width set to 50 ns.

Table 5.24 Results for the “output high” logic level test.

Logic High Minimum (V)	Logic High Average (V)	Logic High Maximum (V)
4.80	4.88	4.96

Test Result: Pass. V_{OH}’s minimum, as measured from signal ground, is greater than 2.7 V.

Test 17: GROUND ISOLATION – SECTION C.10

This test is intended to verify that the grounds from each of the inputs and outputs are properly isolated from chassis ground. As a first indicator of ground isolation, measured resistance between signal ground and chassis ground is shown below, where "Short" is defined as <1 Ω and "Open" is defined as >10 MΩ, the maximum measurable value of the multi-meter used for this test.

Table 5.25 Grounding test results for each input output port combination.

	Test In	**Power In**	**Analog1 Out**	**Analog2 Out**	**Digital In**	**Digital Out**	**Chassis**
Detector In	Short	Short	Open	Short	Open	Open	Short
Test In		Short	Open	Short	Open	Open	Short
Power In			Open	Short	Open	Open	Short
Analog1 Out				Open	Open	Open	Open
Analog2 Out					Open	Open	Short
Digital In						Open	Open
Digital Out							Open

Test Result: Pass. Without detailed schematics of the FEUM v1 devices, it is not possible to draw definitive conclusions from these results, but it is expected that the IAEA can use the data in the table below to inform its initial evaluation of the ground isolation provisions.

Test 18: NGAM COMPATIBILITY – SECTION C.11

Following completion of the Test Plan, this test was deemed to be low priority in terms of relevance to an IAEA decision about the DUT itself. Therefore, this test not conducted.

Test Result: Not Performed.

Test 19: BASELINE FEUM PERFORMANCE – SECTION C.12

Baseline performance testing of the FEUM prototype was performed using the configuration and variable parameters shown in Figure 5.1: type and length of coaxial cable, *L*, between the detector and the front-end electronics (RG-71 and RG-174 are commonly used in IAEA deployments), shaping amplifier time constant (τ, in μs) and the relative discriminator threshold, *T*. An MCA is also included in the evaluation setup to allow more detailed investigation of spectral features during the testing, but most IAEA UMS deployments are counting systems that do not include an MCA. Experimental data were acquired in both the familiar differential pulse-height spectrum (DPHS) and integral pulse-height spectrum (IPHS) forms (see below for more discussion of IPHS), per previous IAEA investigations [1].

As described in prior work by the IAEA and others, an important consideration in evaluating FEUM performance is that counting detectors can strike a different balance, when compared to spectrometers, between electronic noise and the statistical noise that stems from the evolution and shaping of the detector signal [1][2]. The metrics used to evaluate FEUM prototype performance should acknowledge this fact, as well as the IAEA's typical deployment and calibration practices. The IPHS was chosen by the IAEA as a performance metric for the application of FEUM to ^{3}He neutron sensors [1]. Examples of a DPHS and the corresponding IPHS for a ^{3}He detector operating under favorable conditions (i.e., laboratory environment, short cables between sensor and FEUM, and long analog pulse shaping times) are shown in the top pane of Figure 3. In the DPHS, the 764-keV full-energy peak from the neutron capture reaction is well-resolved, and the wall effect "shelves" at energies down to 200 keV are relatively low [1]. The corresponding IPHS in the top pane of Figure 3 has a relative integral count rate (per the secondary vertical axis) approaching unity from 0 keV to approximately 200 keV, and declining slowly until the edge of the full-energy

peak where it falls sharply to zero. This indicates that nearly all of the neutron counts in the DPHS are in the full-energy peak and that this peak has a narrow full width at half maximum (FWHM), consistent with a relatively low level of electronic noise.

Example integral pulse-height spectra for a ^{3}He detector operating in more challenging scenarios are given in the bottom pane of Example integral pulse height spectra for near-ideal performance (black) and nominal performance targets for ^{3He} instruments operating in more demanding deployment scenarios: “easy” (green), “medium” (blue) and “difficult” (red)., where T is a relative discriminator threshold normalized to the 764-keV full-energy peak. The black line represents near-ideal performance for this detector, as in the top pane of Figure 3. The green, blue, and red curves are indicative of the IAEA performance targets for the “easy” (short cable, long τ), “medium” (medium length cable, medium τ), and the “difficult” (long cable, short τ) scenarios, respectively. Progressively higher levels of electronic noise and/or gamma-ray pileup require higher minimum discriminator thresholds, and produce reduced relative neutron efficiencies compared to the near-ideal case (black).

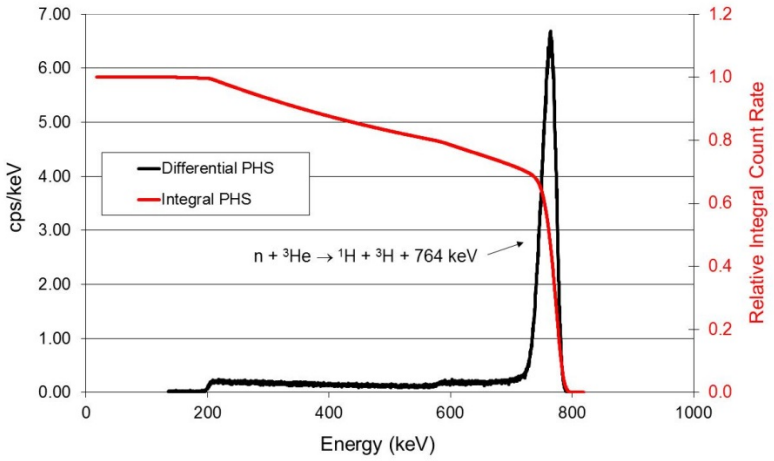

Figure 5.28 Differential and integral pulse-height spectra (PHS) for a ^{3}He instrument operating in favorable conditions.

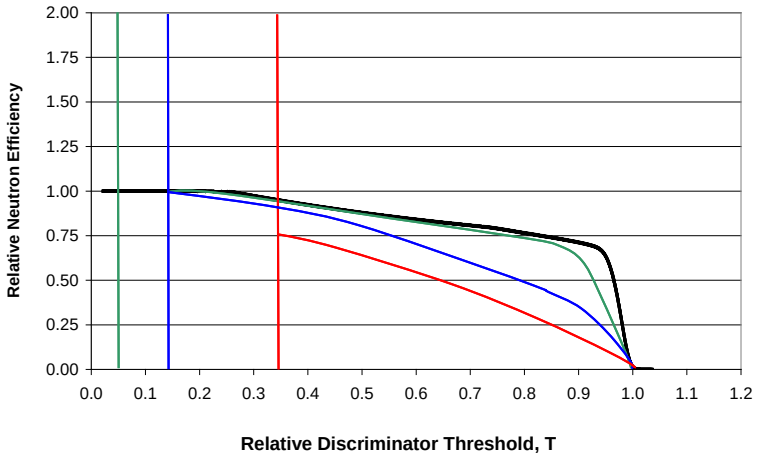

Figure 5.29 Example integral pulse height spectra for near-ideal performance (black) and nominal performance targets for ^{3}He instruments operating in more demanding deployment scenarios: “easy” (green), “medium” (blue) and “difficult” (red).

FEUM performance targets for detector types other than ^{3}He have not been specified by the IAEA. In PNNL’s evaluation, the IPHS and the metrics dictated by the IAEA for ^{3}He are also applied to the AWG because it represents near-ideal performance for a radiation sensor like ^{3}He in which the majority of the signal is collected in a single, isolated peak. Only the DPHS is used for the ^{235}U fission chamber and the NaI(Tl) because no performance targets have been specified by the IAEA, and the PNNL team believes that the DPHS, and the noise floor, are the most revealing diagnostics on performance for these sensor types.

All baseline performance testing was done in a laboratory environment with no significant radiation or electromagnetic backgrounds. Input signals were provided by AWG, a ^{3}He and a U-235 Fission Chamber (FC) proportional counter exposed to ^{252}Cf, and a NaI(Tl) scintillator exposed to ^{137}Cs.

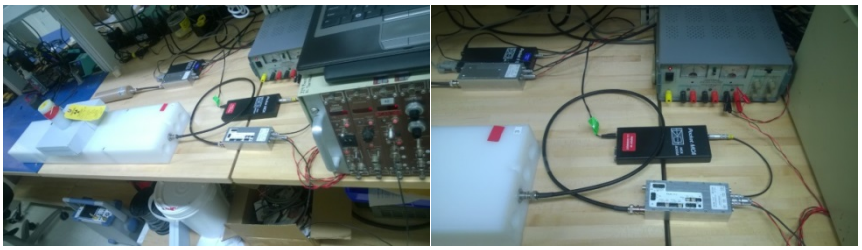

Figure 5.30 General testing station setup.

ARBITRARY WAVEFORM GENERATOR (AWG)

The DUT settings used are listed in Table 5.26. The nominal width of the pulse presented to the DUT input is approximately 100 ns. The AWG was set to generate a 10mV ramp at a repetition rate of 1 kHz, similar to the AWG configurations described previously.

Table 5.26 DUT settings for Test 19, AWG baseline.

Parameter	Setting	Value
Charge Gain	L	1.9-68 mV/pC
G2 – Gain	C	21.67
G3 – Gain	A	
HVH - High Voltage	0	400 V
HVL - High Voltage	0	
DH – Discriminator High	1	360 mV
DL – Discriminator Low	8	
SW4 – TTL Pulse Width	001	200 ns
Detector Source Impedance	330 kΩ	
Precision Capacitor	2200 pF	
Count Time	60 seconds	

Table 5.27 below summarizes the measured performance using the integral pulse height spectrum (IPHS) and the performance metrics described by the IAEA in the FEUM procurement specifications [6]. The noise floor is given by T_{noise} while the efficiency relative to the ideal case (short cable, long analog shaping time) is given by $\varepsilon_{relative.}$ A value of "~" indicates that the noise floor for that test configuration was higher than the specified threshold setting and therefore, relative efficiency cannot be calculated. Figure 5.31 to Figure 5.42 show a graphical view of these results in both IPHS and differential pulse height spectra (DPHS) for the AWG-based tests.

Table 5.27 Baseline performance-testing results for the AWG as the signal generator for both charge-sensitive ("Q mode") and current-sensitive ("I mode") preamplifier modes.

	Q mode		***I mode***	
L (m RG-71), τ (μs)	T_{noise}	$T, \varepsilon_{relative}$	T_{noise}	$T, \varepsilon_{relative}$
(RG-71 12cm, 0.1us)	0.0651	(0.2, 0.80) (0.5, 0.49) (0.8, 0.18)	0.1225	(0.2, 0.79) (0.5, 0.48) (0.8, 0.18)
(RG-71 1m, 0.1us)	0.3440	(0.2, ~) (0.5, 0.47) (0.8, 0.16)	0.4811	(0.2, ~) (0.5, 0.44) (0.8, 0.13)
(RG-71 10m, 0.1us)	0.3144	(0.2, ~) (0.5, 0.47) (0.8, 0.16)	0.5426	(0.2, ~) (0.5, ~) (0.8, 0.11)
(RG-71 50m, 0.1us)	0.3489	(0.2, ~) (0.5, 0.46) (0.8, 0.16)	0.5313	(0.2, ~) (0.5, ~) (0.8, 0.12)
(RG-71 100m, 0.1us)	0.3721	(0.2, ~) (0.5, 0.46) (0.8, 0.15)	0.5667	(0.2, ~) (0.5, ~) (0.8, 0.10)
(RG-174 100m, 0.1us)	0.6010	(0.2, ~) (0.5, ~) (0.8, 0.12)	0.0919	(0.2, 0.81) (0.5, 0.50) (0.8, 0.20)
(RG-71 12cm, 0.4us)	0.0285	(0.2, 0.82) (0.5, 0.51) (0.8, 0.20)	0.0103	(0.2, 0.81) (0.5, 0.50) (0.8, 0.20)
(RG-71 1m, 0.4us)	0.1508	(0.2, 0.80) (0.5, 0.49) (0.8, 0.18)	0.0749	(0.2, 0.80) (0.5, 0.49) (0.8, 0.19)
(RG-71 10m, 0.4us)	0.1470	(0.2, 0.81) (0.5, 0.5) (0.8, 0.19)	0.0878	(0.2, 0.79) (0.5, 0.49) (0.8, 0.19)
(RG-71 50m, 0.4us)	0.1300	(0.2, 0.81) (0.5, 0.5) (0.8, 0.19)	0.0356	(0.2, 0.80) (0.5, 0.50) (0.8, 0.20)
(RG-71 100m, 0.4us)	0.1388	(0.2, 0.80) (0.5, 0.50) (0.8, 0.19)	0.1518	(0.2, 0.78) (0.5, 0.48) (0.8, 0.18)
(RG-174 100m, 0.4us)	0.2246	(0.2, ~) (0.5, 0.48) (0.8, 0.17)	0.2757	(0.2, ~) (0.5, 0.46) (0.8, 0.15)
(RG-71 12cm, 2.4us)	0.0257	(0.2, 0.82) (0.5, 0.51) (0.8, 0.2)	0.0096	(0.2, 0.81) (0.5, 0.50) (0.8, 0.20)
(RG-71 1m, 2.4us)	0.1453	(0.2, 0.81) (0.5, 0.50) (0.8, 0.19)	0.0219	(0.2, 0.81) (0.5, 0.50) (0.8, 0.20)
(RG-71 10m, 2.4us)	0.1547	(0.2, 0.81) (0.5, 0.50) (0.8, 0.19)	0.0246	(0.2, 0.81) (0.5, 0.50) (0.8, 0.20)
(RG-71 50m, 2.4us)	0.1837	(0.2, 0.81) (0.5, 0.50) (0.8, 0.19)	0.0356	(0.2, 0.80) (0.5, 0.50) (0.8, 0.20)
(RG-71 100m, 2.4us)	0.2300	(0.2, ~) (0.5, 0.50) (0.8, 0.19)	0.5667	(0.2, ~) (0.5, ~) (0.8, 0.10)
(RG-174 100m, 2.4us)	0.3211	(0.2, ~) (0.5, 0.48) (0.8, 0.16)	0.0916	(0.2, 0.80) (0.5, 0.49) (0.8, 0.19)

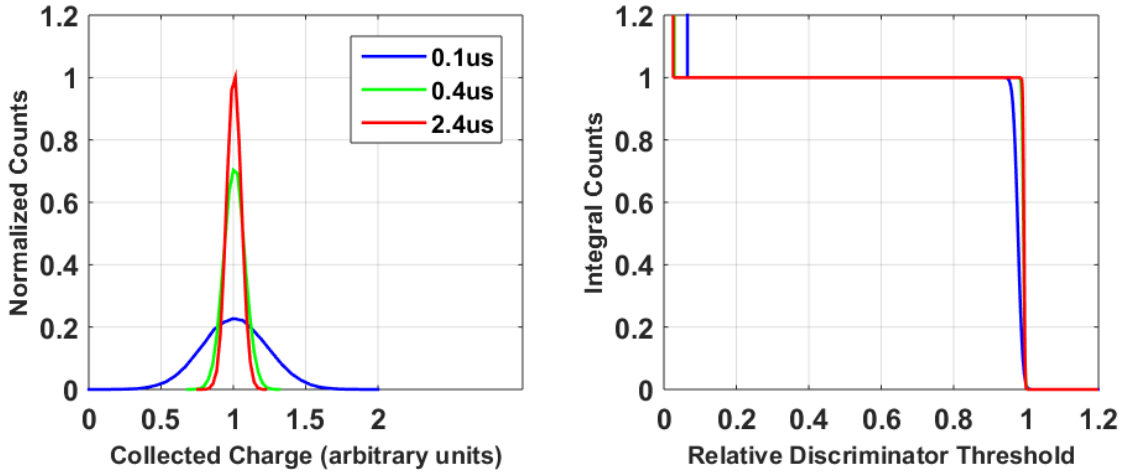

Figure 5.31 AWG baseline performance results: charge-sensitive mode, 12 cm RG-71 cable.

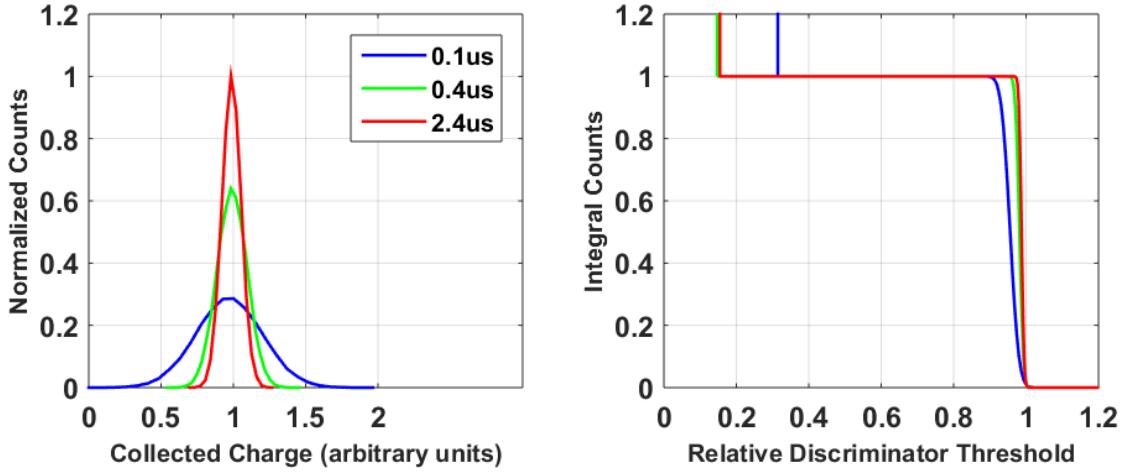

Figure 5.32 AWG baseline performance results: charge-sensitive mode, 10 m RG-71 cable.

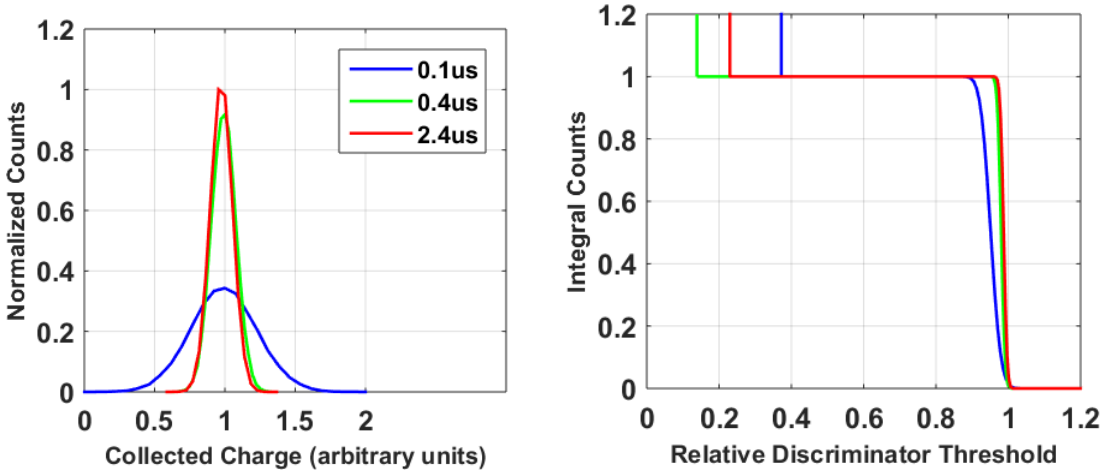

Figure 5.33 AWG baseline performance results: charge-sensitive mode, 100 m RG-71 cable.

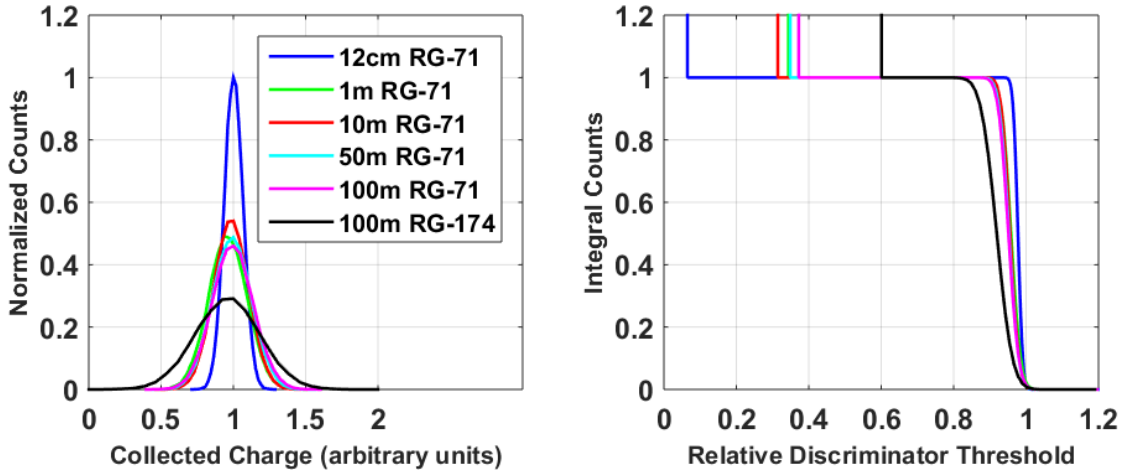

Figure 5.34 AWG baseline performance results: charge-sensitive mode, $\tau = 0.1\mu s$.

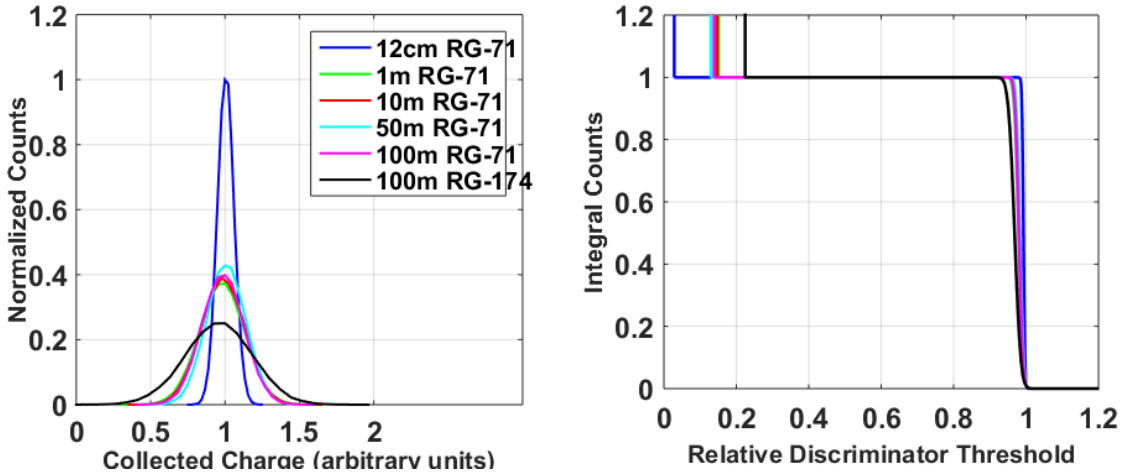

Figure 5.35 AWG baseline performance results: charge-sensitive mode, $\tau = 0.4\mu s$.

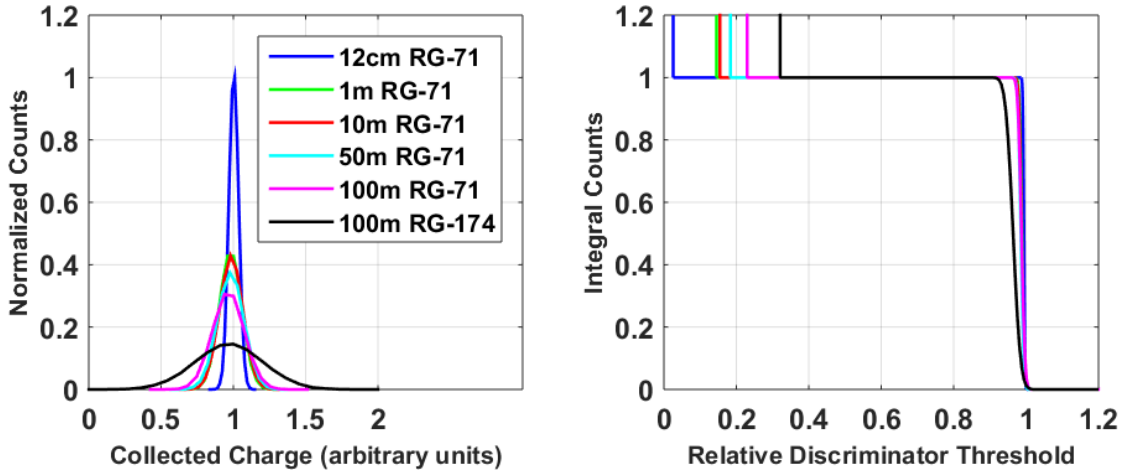

Figure 5.36 AWG baseline performance results: charge-sensitive mode, $\tau = 2.4\mu s$.

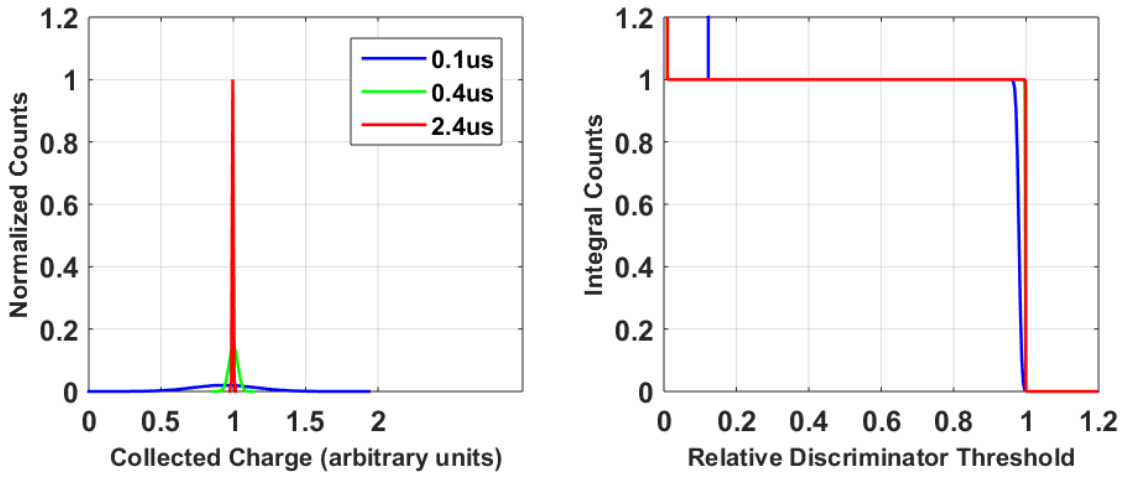

Figure 5.37 AWG baseline performance results: current-sensitive mode, 12 cm RG-71 cable.

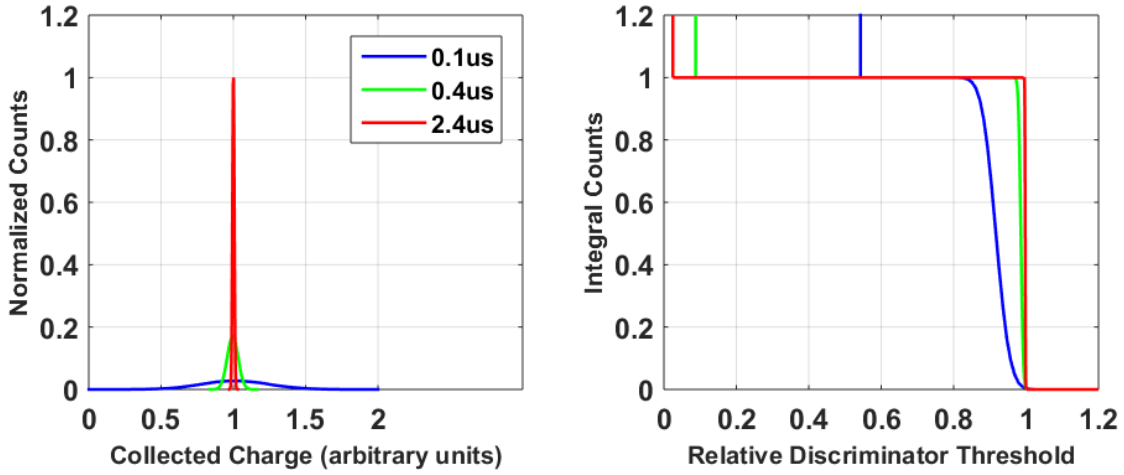

Figure 5.38 AWG baseline performance results: current-sensitive mode 10 m RG-71 cable.

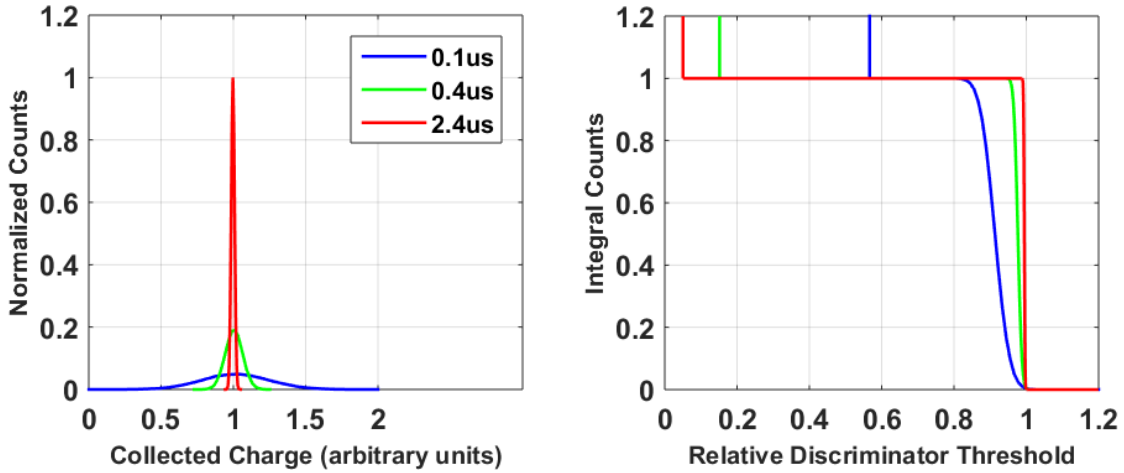

Figure 5.39 AWG baseline performance results: current-sensitive mode, 100 m RG-71 cable.

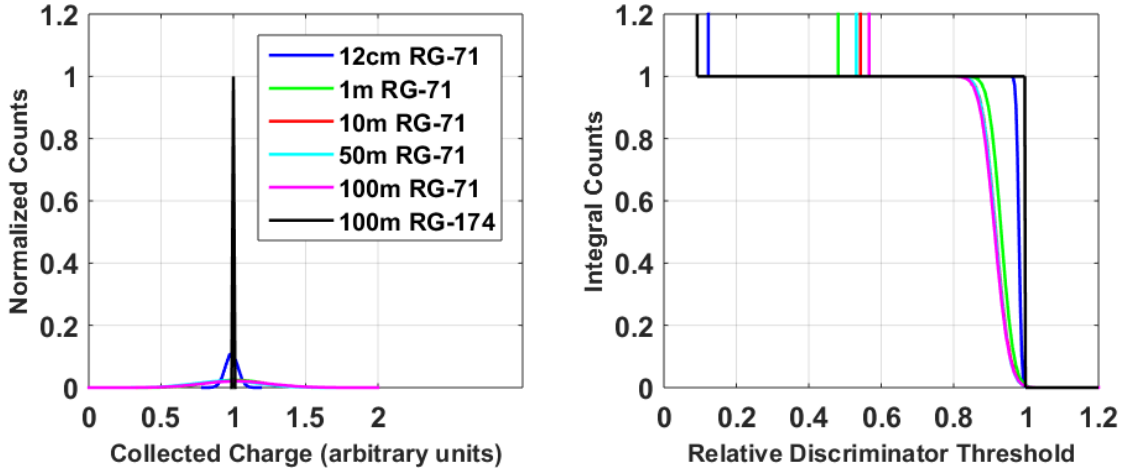

Figure 5.40 AWG baseline performance results: current-sensitive mode, τ = 0.1μs.

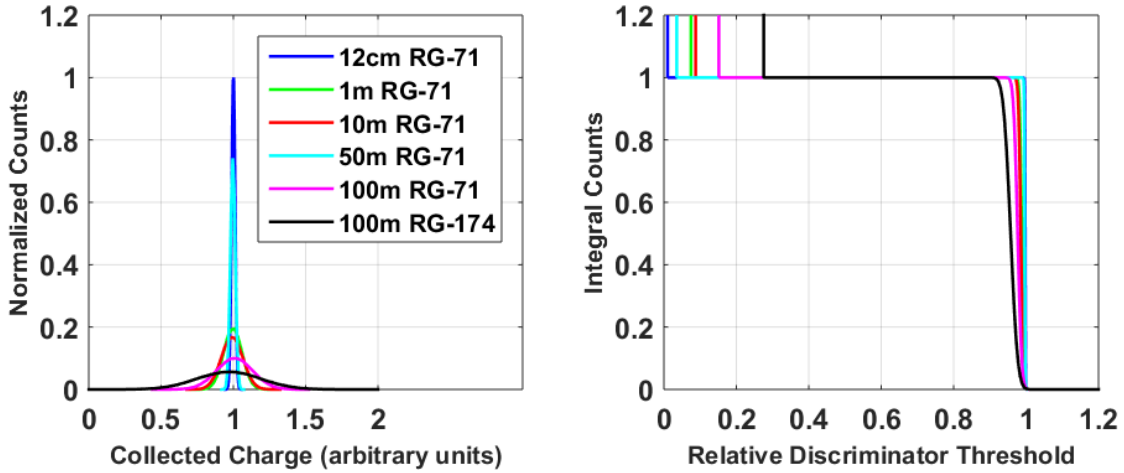

Figure 5.41 AWG baseline performance results: current-sensitive mode, τ = 0.4μs.

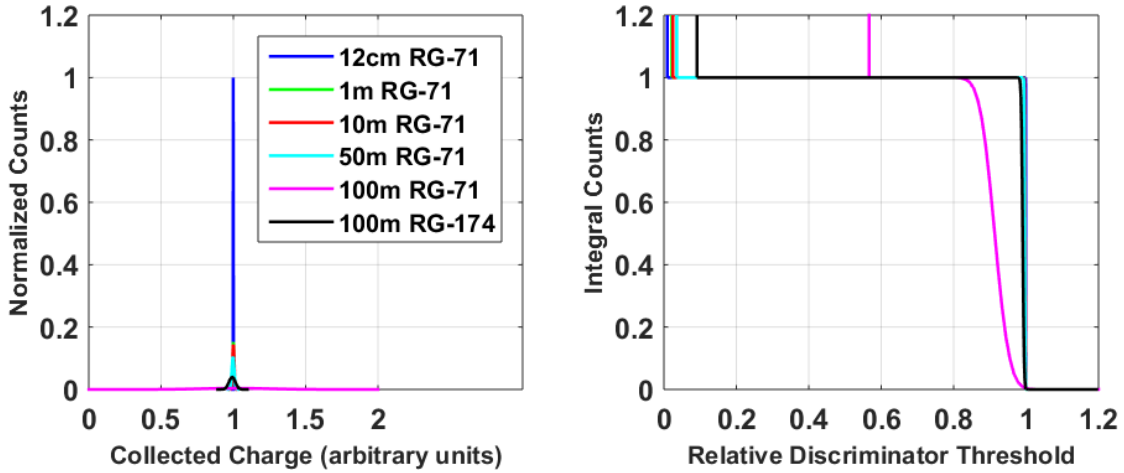

Figure 5.42 AWG baseline performance results: current-sensitive mode, τ = 2.4µs.

The figures above demonstrate that the DUT baseline performance, for the AWG input, approaches the ideal for all but a few cases with either/both very short shaping times or very long cables. Degraded performance is manifested by a higher noise floor and degraded FWHM on the peak. Generally speaking, the performance of the charge-sensitive mode is better than for the current-sensitive mode. All trends are consistent with expectations and with previously published work by the IAEA.

^{3}He Proportional Counter

The DUT settings used are listed in Table 5.28 below.

Table 5.28 DUT settings for Test 19, ^{3}He proportional counter baseline.

Parameter	Setting	Value
Charge Gain	H	1.9-70 V/pC
G2 – Gain	F	14
G3 – Gain	4	
HVH - High Voltage	D	1750 V
HVL - High Voltage	8	
DH – Discriminator High	1	360 mV
DL – Discriminator Low	8	
SW4 – TTL Pulse Width	001	200 ns
Detector Source Impedance	10 MΩ	
Count Time	60 seconds	
Detector Model	RS-P4-0825-203	
Source	20 µCi Cf-252	

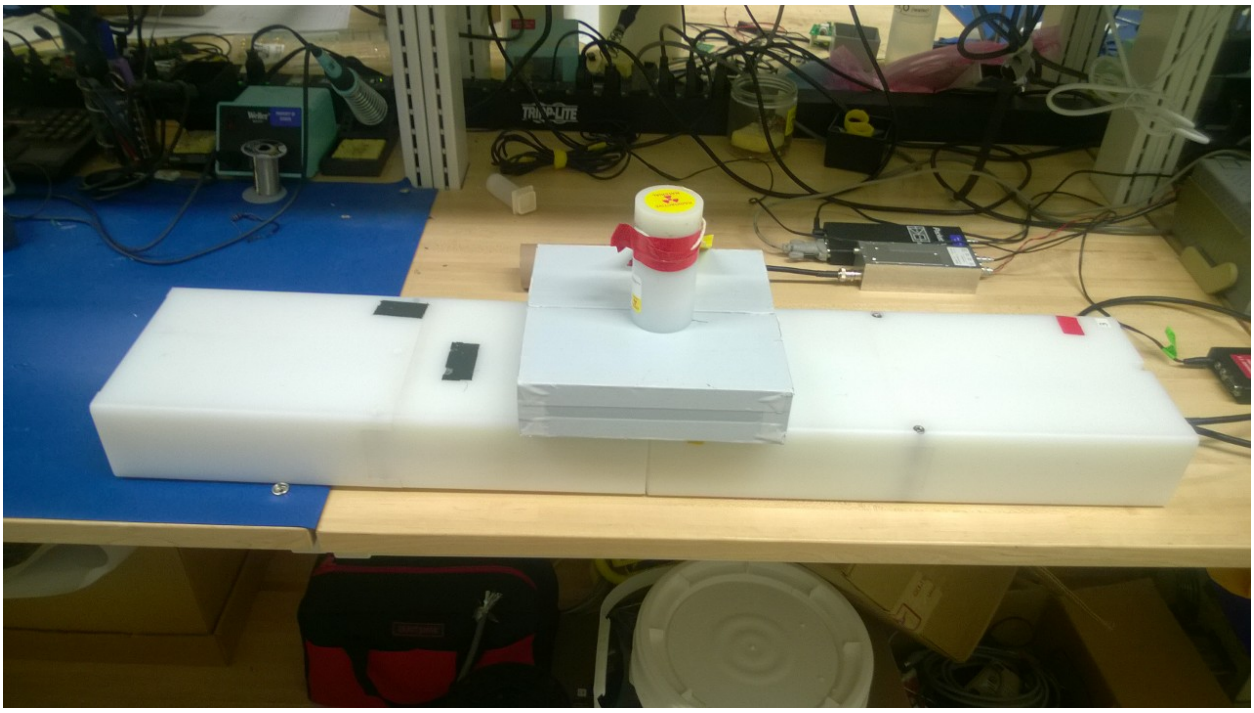

Figure 5.43 Test setup for baseline performance testing using an ^{3}He detector.

The table below summarizes the measured performance using the IPHS and the performance metrics described by the IAEA in the FEUM procurement specifications. The noise floor is given by T_{noise} while the efficiency relative to the ideal case (short cable, long shaping time) is given by $\varepsilon_{relative.}$ A value of "~" indicates that the noise floor for that test configuration was higher than the specified threshold setting and therefore, relative efficiency cannot be calculated.

Table 5.29 Baseline performance-testing results for a ^{3}He detector as the signal generator for both charge-sensitive ("Q mode") and current-sensitive ("I mode") preamplifier modes.

	Q mode		***I mode***	
L (m RG-71), τ (μs)	***T_{noise}***	***T, $\varepsilon_{relative}$***	***T_{noise}***	***T, $\varepsilon_{relative}$***
(RG-71 12cm, 0.1us)	0.0260	(0.2, 0.28) (0.5, 0.09) (0.8, 0.02)	0.0279	(0.2, 0.31) (0.5, 0.11) (0.8, 0.02)
(RG-71 1m, 0.1us)	0.0306	(0.2, 0.30) (0.5, 0.10) (0.8, 0.02)	0.0798	(0.2, 0.34) (0.5, 0.12) (0.8, 0.02)
(RG-71 10m, 0.1us)	0.0995	(0.2, 0.37) (0.5, 0.13) (0.8, 0.02)	0.1963	(0.2, 0.35) (0.5, 0.12) (0.8, 0.02)
(RG-71 50m, 0.1us)	0.1795	(0.2, 0.29) (0.5, 0.09) (0.8, 0.01)	0.3962	(0.2, ~) (0.5, 0.10) (0.8, 0.01)
(RG-71 100m, 0.1us)	0.1944	(0.2, 0.30) (0.5, 0.10) (0.8, 0.01)	0.4200	(0.2, ~) (0.5, 0.11) (0.8, 0.01)
(RG-174 100m, 0.1us)	0.4200	(0.2, ~) (0.5, 0.13) (0.8, 0.01)	0.7241	(0.2, ~) (0.5, ~) (0.8, 0.01)
(RG-71 12cm, 0.4us)	0.0088	(0.2, 0.74) (0.5, 0.40) (0.8, 0.10)	0.0078	(0.2, 0.73) (0.5, 0.40) (0.8, 0.10)

	Q mode		*I mode*	
L (m RG-71), τ (μs)	T_{noise}	T, $\varepsilon_{relative}$	T_{noise}	T, $\varepsilon_{relative}$
(RG-71 1m, 0.4us)	0.0093	(0.2, 0.74) (0.5, 0.41) (0.8, 0.10)	0.0084	(0.2, 0.73) (0.5, 0.40) (0.8, 0.10)
(RG-71 10m, 0.4us)	0.0200	(0.2, 0.76) (0.5, 0.41) (0.8, 0.10)	0.0518	(0.2, 0.79) (0.5, 0.43) (0.8, 0.10)
(RG-71 50m, 0.4us)	0.0835	(0.2, 0.76) (0.5, 0.41) (0.8, 0.09)	0.1933	(0.2, 0.71) (0.5, 0.36) (0.8, 0.06)
(RG-71 100m, 0.4us)	0.1659	(0.2, 0.71) (0.5, 0.36) (0.8, 0.06)	0.3682	(0.2, ~) (0.5, 0.30) (0.8, 0.03)
(RG-174 100m, 0.4us)	0.1795	(0.2, 0.23) (0.5, 0.04) (0.8, 0.01)	0.3443	(0.2, ~) (0.5, 0.09) (0.8, 0.01)
(RG-71 12cm, 2.4us)	0.0170	(0.2, 0.78) (0.5, 0.43) (0.8, 0.11)	0.0151	(0.2, 0.78) (0.5, 0.44) (0.8, 0.12)
(RG-71 1m, 2.4us)	0.0123	(0.2, 0.75) (0.5, 0.42) (0.8, 0.11)	0.0159	(0.2, 0.77) (0.5, 0.43) (0.8, 0.11)
(RG-71 10m, 2.4us)	0.0190	(0.2, 0.75) (0.5, 0.41) (0.8, 0.11)	0.0370	(0.2, 0.79) (0.5, 0.44) (0.8, 0.11)
(RG-71 50m, 2.4us)	0.0529	(0.2, 0.74) (0.5, 0.41) (0.8, 0.10)	0.1386	(0.2, 0.75) (0.5, 0.40) (0.8, 0.08)
(RG-71 100m, 2.4us)	0.1071	(0.2, 0.71) (0.5, 0.38) (0.8, 0.08)	0.2534	(0.2, ~) (0.5, 0.32) (0.8, 0.04)
(RG-174 100m, 2.4us)	0.2283	(0.2, ~) (0.5, 0.07) (0.8, 0.01)	0.2917	(0.2, ~) (0.5, 0.07) (0.8, 0.01)

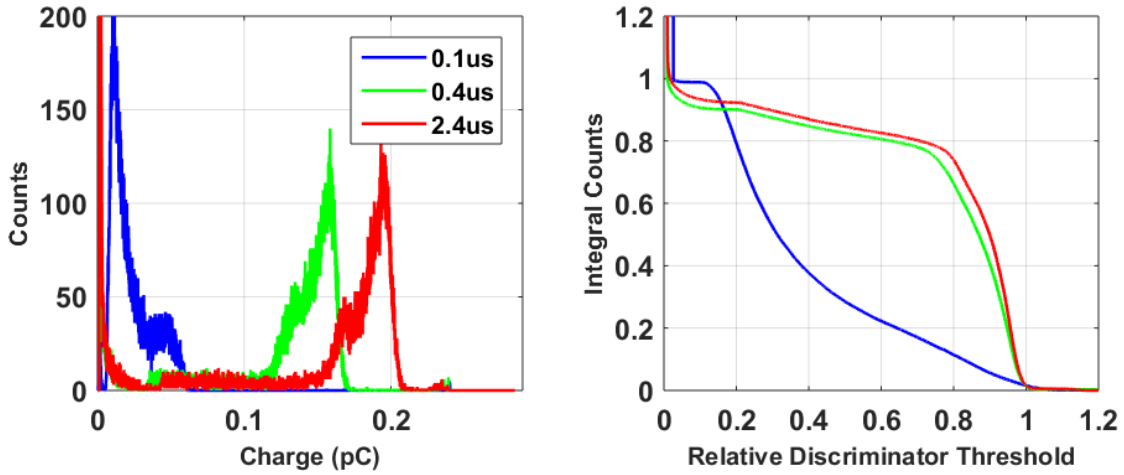

Figure 5.44 He^3 baseline performance results: charge-sensitive mode, 12 cm RG-71 cable.

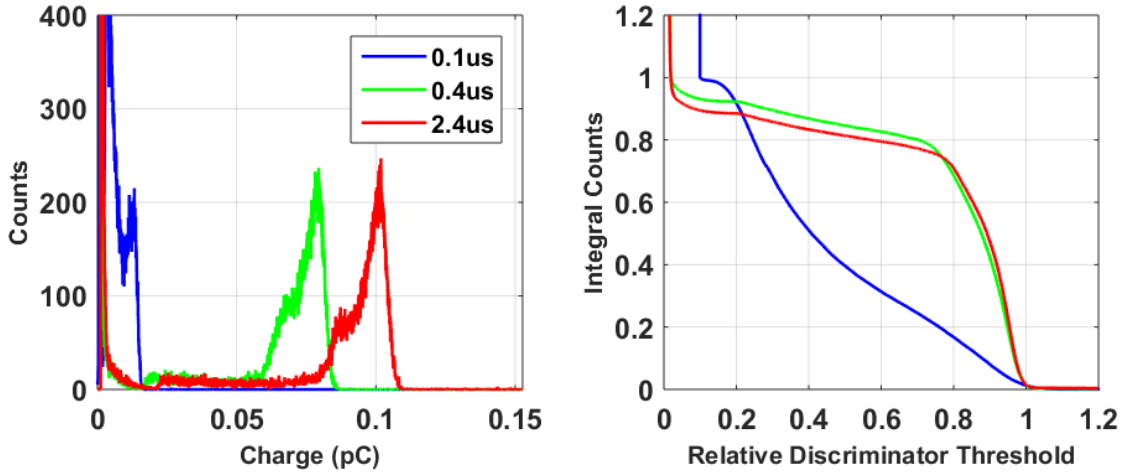

Figure 5.45 He^3 baseline performance results: charge-sensitive mode, 10 m RG-71 cable.

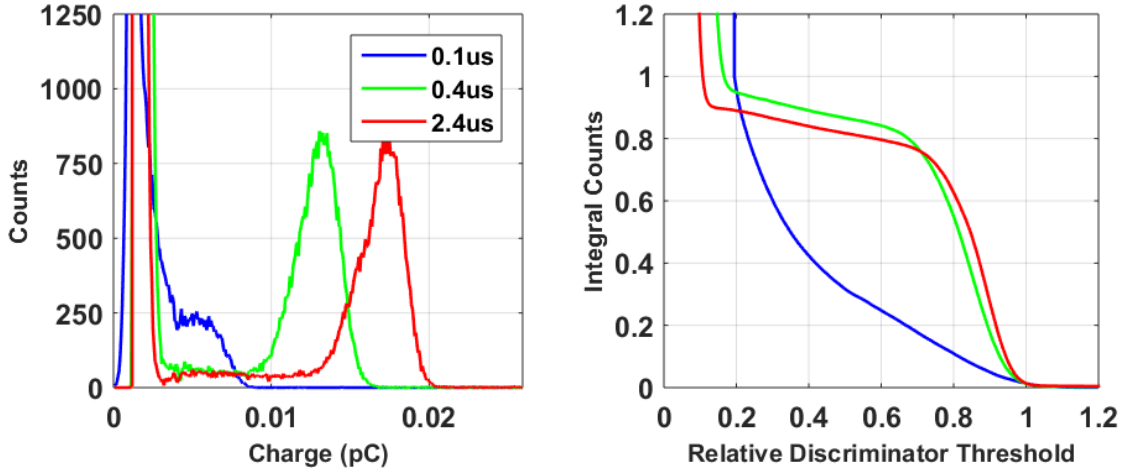

Figure 5.46 He^3 baseline performance results: charge-sensitive mode, 100 m RG-71 cable.

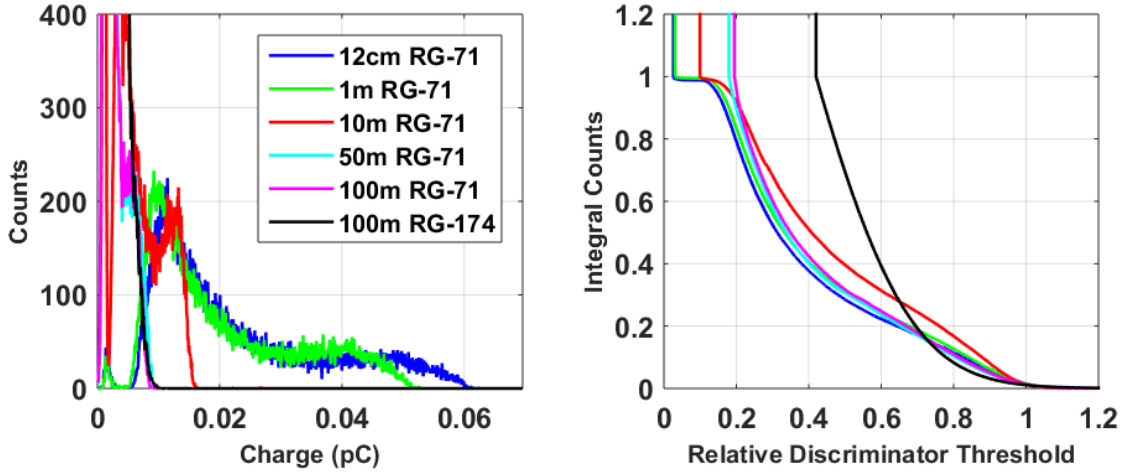

Figure 5.47 He^3 baseline performance results: charge-sensitive mode, $\tau = 0.1\mu s$.

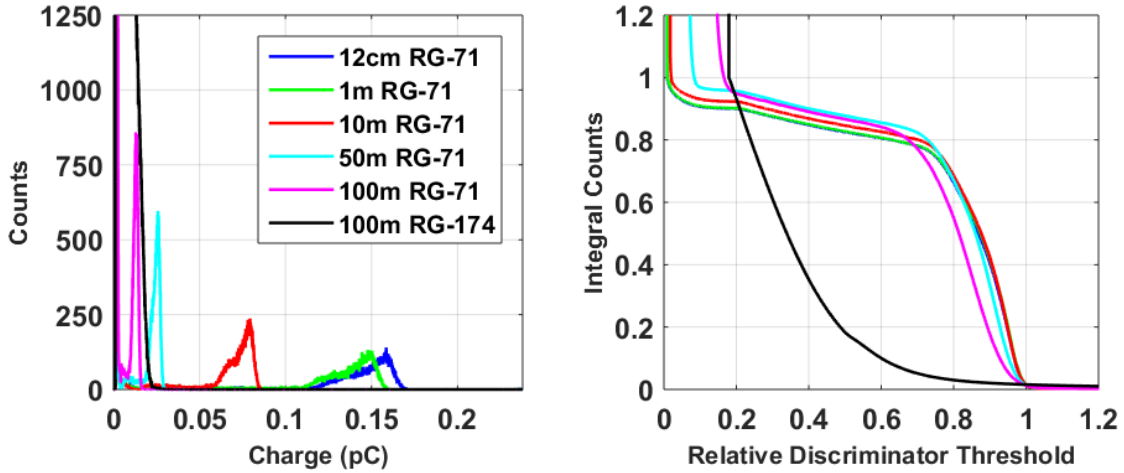

Figure 5.48 He^3 baseline performance results: charge-sensitive mode, $\tau = 0.4\mu s$.

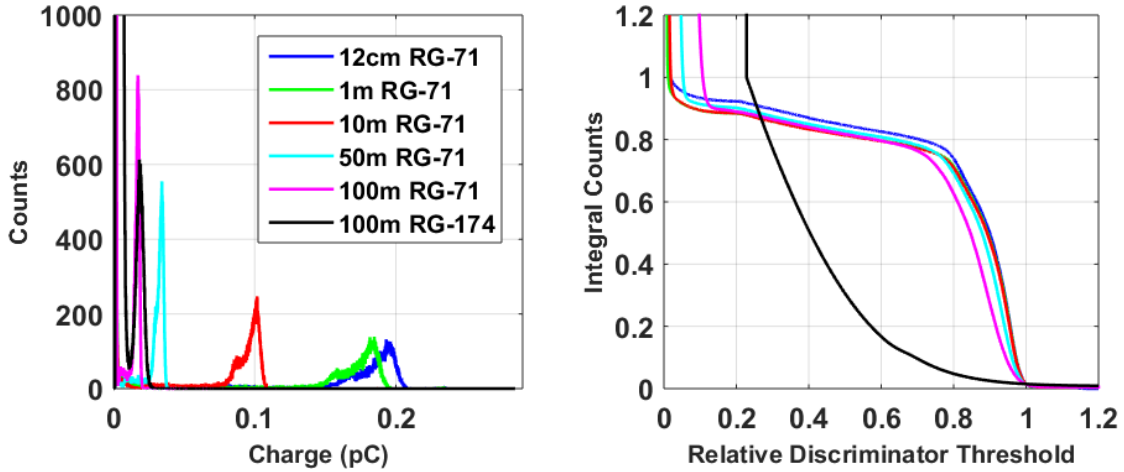

Figure 5.49 He3 baseline performance results: charge-sensitive mode, $\tau = 2.4\mu s$.

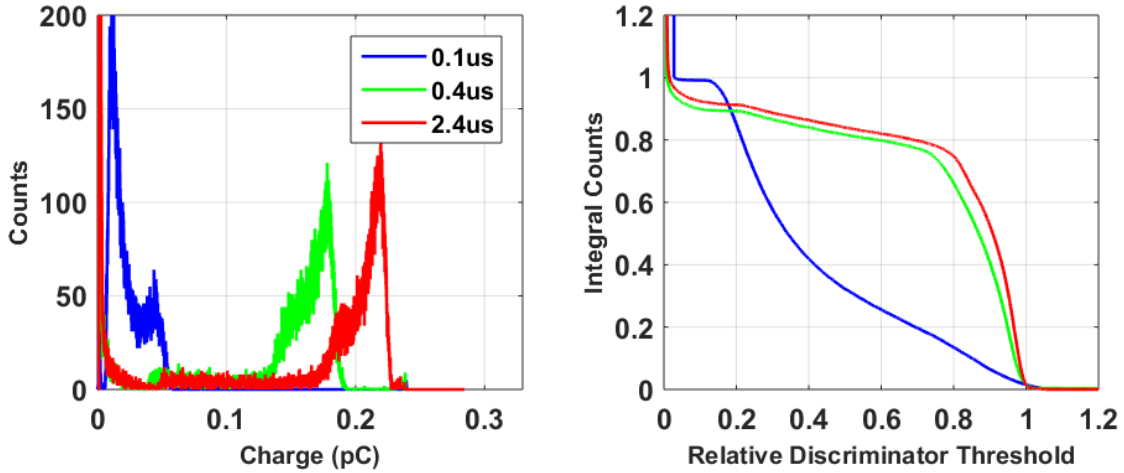

Figure 5.50 He^3 baseline performance results: current-sensitive mode, 12 cm RG-71 cable.

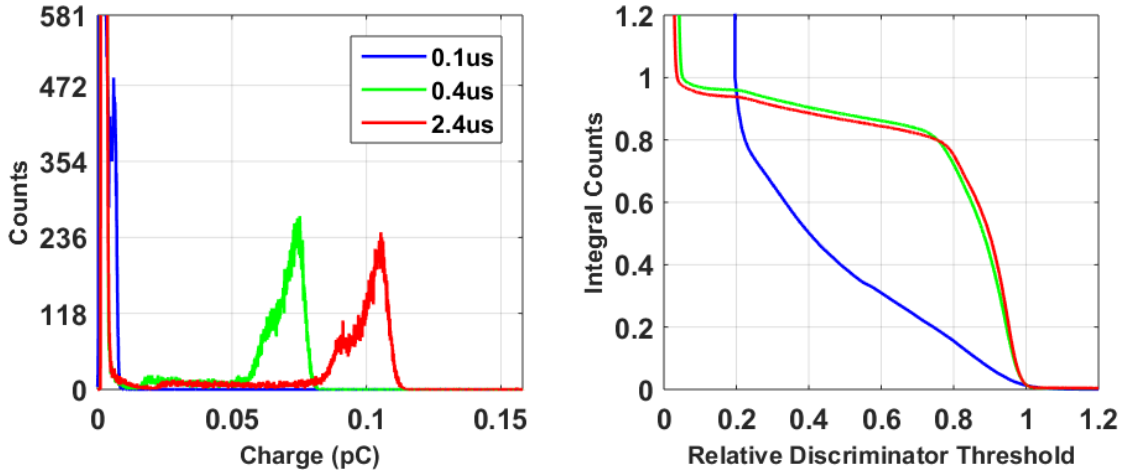

Figure 5.51 He^3 baseline performance results: current-sensitive mode, 10 m RG-71 cable.

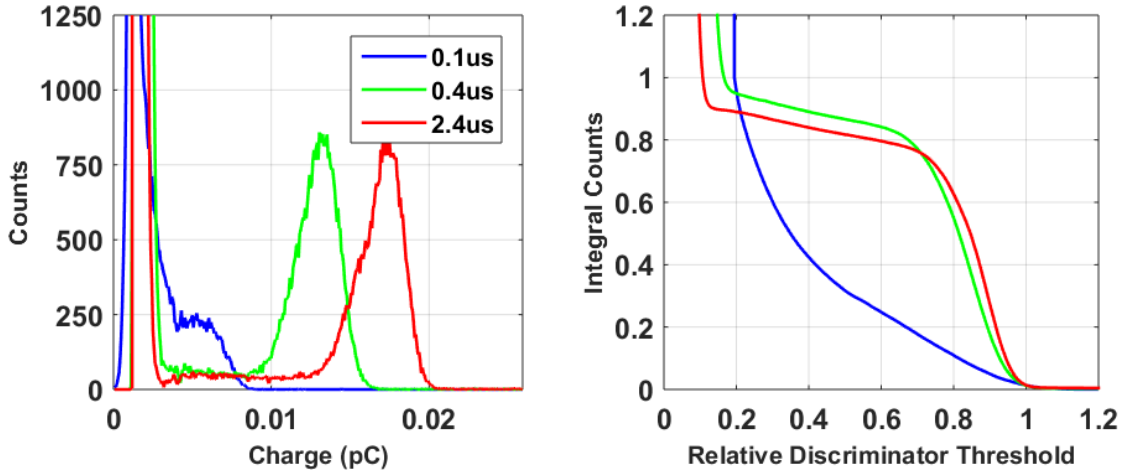

Figure 5.52 He^3 baseline performance results: current-sensitive mode, 100 m RG-71 cable.

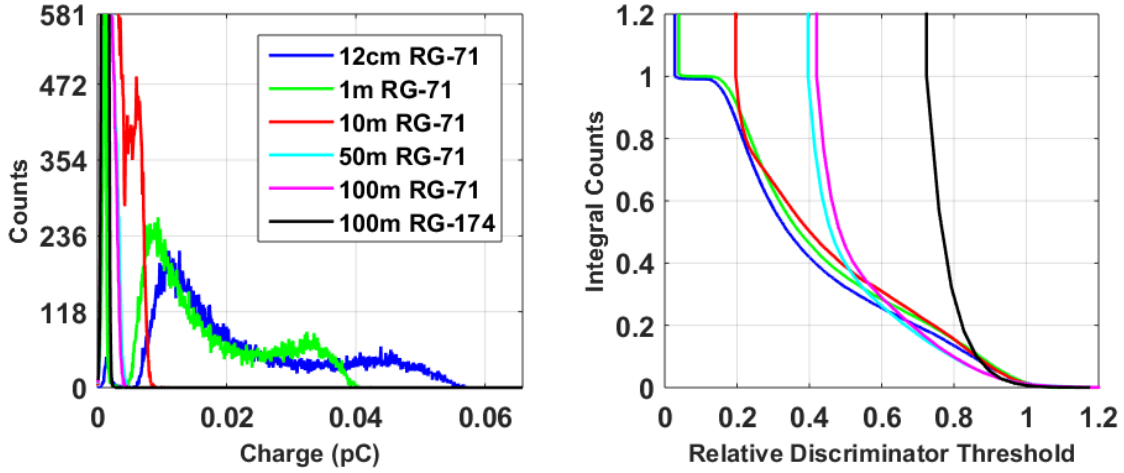

Figure 5.53 He^3 baseline performance results: current-sensitive mode, τ = 0.1µs.

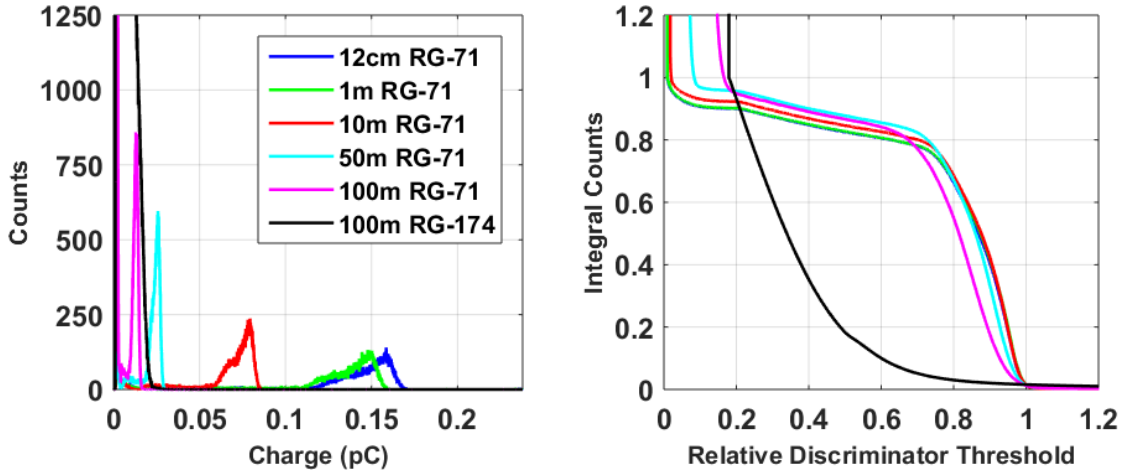

Figure 5.54 He3 baseline performance results: current-sensitive mode, τ = 0.4µs.

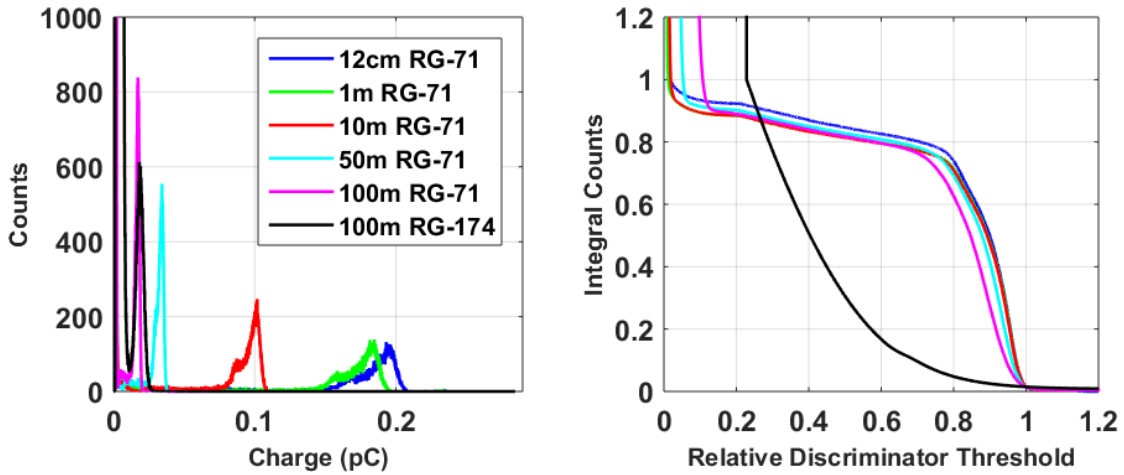

Figure 5.55 He3 baseline performance results: current-sensitive mode, τ = 2.4μs.

The baseline performance for the DUT coupled to a ^{3}He detector is consistent with expectations, including a severely degraded performance at very short shaping times and/or long cables. Degraded performance is manifested by a higher noise floor and degraded FWHM on the full-energy (i.e., 764-keV) peak. Generally speaking, the performance of the charge-sensitive mode is better than for the current-sensitive mode. All trends are consistent with expectations and with previously published work by the IAEA.

It should be noted that the tabulated performance (i.e., T_{noise} and $\varepsilon_{relative.}$) for the DUT cannot be directly compared to the target values for ^{3}He sensors, as provided in the IAEA specifications because there appears to be an error in the IAEA calculations for the ^{3}He performance targets in ^{3}He. More investigation and consultation with the IAEA is needed.

U-235 Fission Chamber

Baseline performance tests for the DUT coupled to a fission chamber were conducted for proof of principle and validation of testing methods, but are not presented here because the available source was too weak to produce meaningful findings in acceptable count times. In addition, the most relevant results for a fission chamber are in the presence of an intense gamma-ray field, where fission chambers are most often utilized by the IAEA. Those results are presented in in Test 24: High Radiation Tests.

NaI(Tl) Scintillator

The DUT settings used are listed in Table 5.30 below.

Table 5.30 DUT settings for Test 19, NaI (Tl) Scintillator baseline.

Parameter	**Setting**	**Value**
Charge Gain	L	1.9-68 mV/pC
G2 – Gain	8	3.67
G3 – Gain	0	
HVH - High Voltage	5	900 V
HVL - High Voltage	0	
DH – Discriminator High	1	360 mV
DL – Discriminator Low	8	
SW4 – TTL Pulse Width	001	200 ns
Detector Source Impedance	330 kΩ	
Count Time	60 seconds	
Detector Model	Ludlum 44-2	
Source	9.66 μCi Cs-137	

Figure 5.56 Test Setup for NaI. The button source is taped to the end of the detector.

The measured performance for the NaI(Tl) detector is summarized in Table 5.31 below using comparisons of the DPHS and the noise threshold for various configurations. Graphical representations of the full-energy DPHS and relative FWHM are shown in Figure 5.57 through Figure 5.68. The relative FWHM plots are intended to semi-quantitatively depict the change in FWHM as the test variables of cable length and analog shaping time are varied.

Table 5.31 Baseline performance-testing results for a NaI(Tl) detector as the signal generator for both charge-sensitive ("Q mode") and current-sensitive ("I mode") preamplifier modes, using the noise threshold as the key parameter.

L (m RG-71), τ (μs)	***Q mode T_{noise}***	***I mode T_{noise}***
(RG-71 12cm, 0.1us)	0.0536	0.0169
(RG-71 1m, 0.1us)	0.0560	0.0199
(RG-71 10m, 0.1us)	0.0526	0.0691
(RG-71 50m, 0.1us)	0.0401	0.1721
(RG-71 100m, 0.1us)	0.0389	0.1858
(RG-174 100m, 0.1us)	0.0828	0.4773
(RG-71 12cm, 0.4us)	0.0154	0.0138
(RG-71 1m, 0.4us)	0.0154	0.0135
(RG-71 10m, 0.4us)	0.0173	0.0187
(RG-71 50m, 0.4us)	0.0168	0.0120
(RG-71 100m, 0.4us)	0.0218	0.0221
(RG-174 100m, 0.4us)	0.0365	0.0493
(RG-71 12cm, 2.4us)	0.0100	0.0115
(RG-71 1m, 2.4us)	0.0116	0.0112
(RG-71 10m, 2.4us)	0.0133	0.0132
(RG-71 50m, 2.4us)	0.0151	0.0071
(RG-71 100m, 2.4us)	0.0215	0.012
(RG-174 100m, 2.4us)	0.0383	0.0256

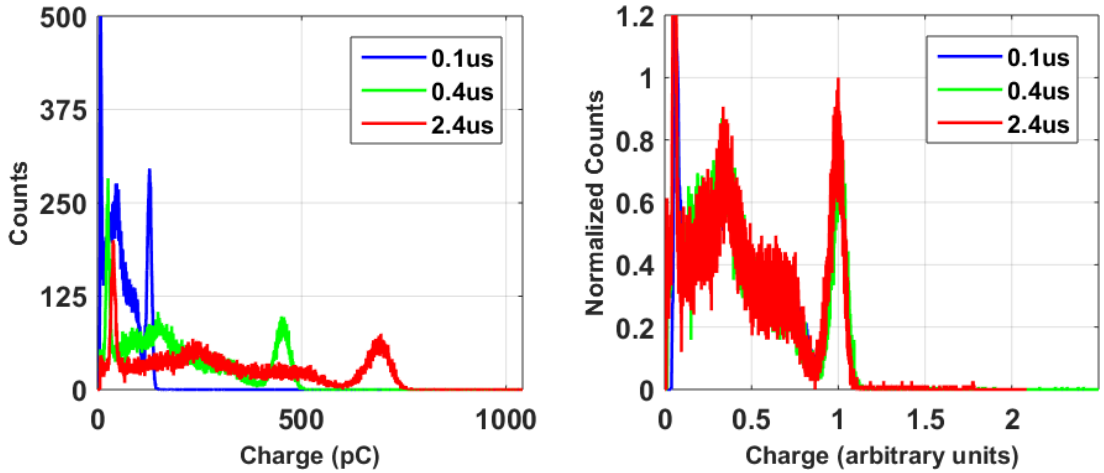

Figure 5.57 NaI baseline performance results: charge-sensitive mode, 12 cm RG-71 cable. Shown in pC (left) and peak-normalized arbitrary units (right).

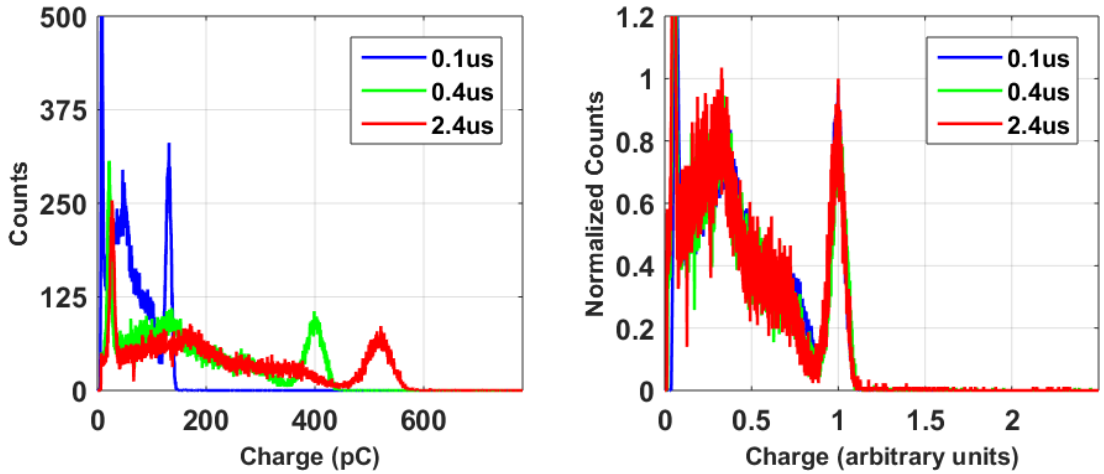

Figure 5.58 NaI baseline performance results: charge-sensitive mode, 10 m RG-71 cable. Shown in pC (left) and peak-normalized arbitrary units (right).

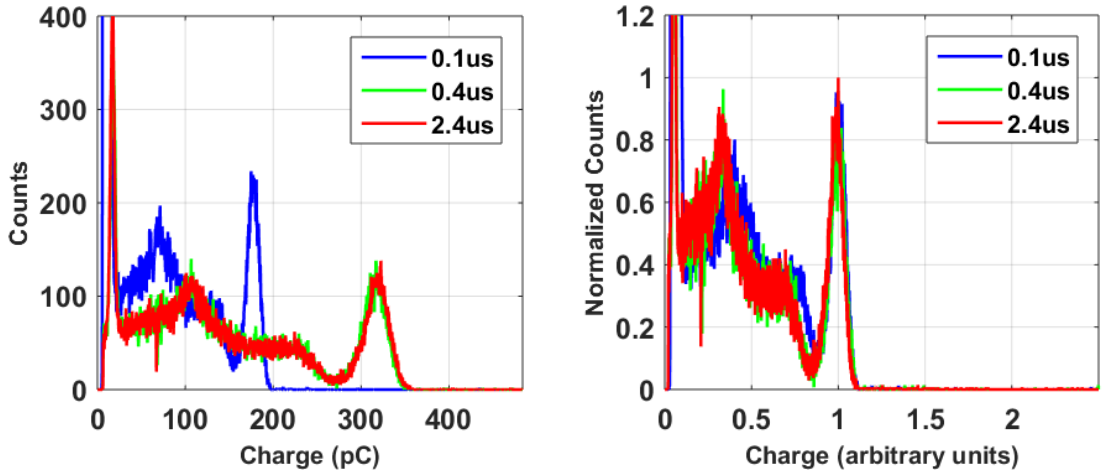

Figure 5.59 NaI baseline performance results: charge-sensitive mode, 100 m RG-71 cable. Shown in pC (left) and peak-normalized arbitrary units (right).

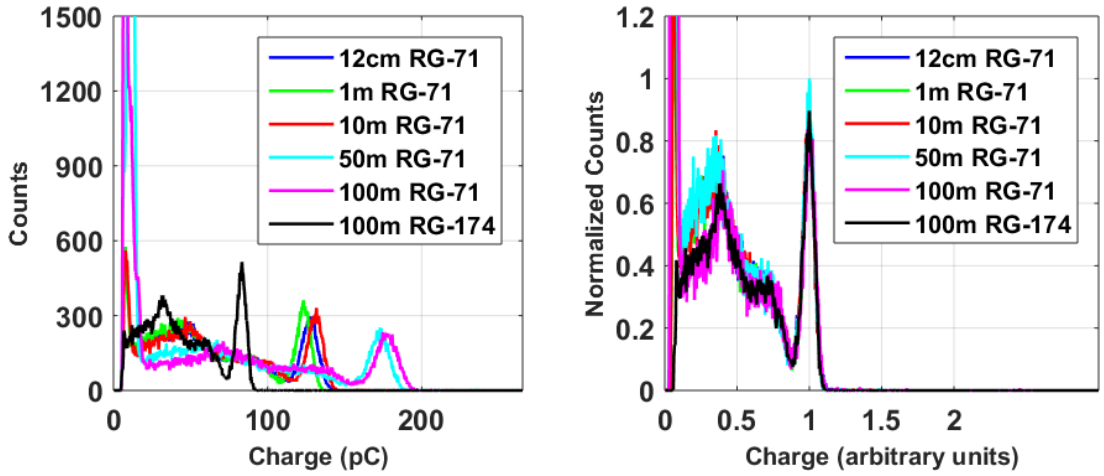

Figure 5.60 NaI baseline performance results: charge-sensitive mode, $\tau = 0.1$ µs. Shown in pC (left) and peak-normalized arbitrary units (right).

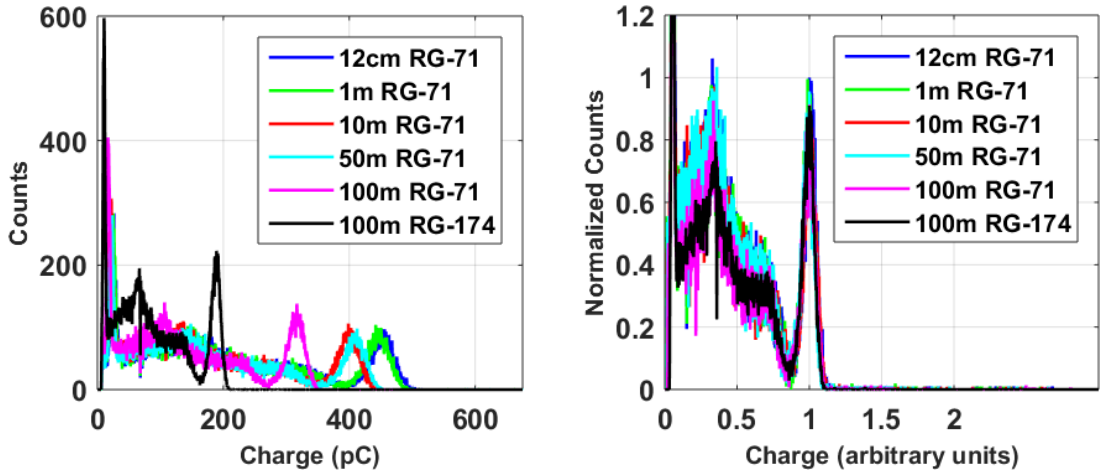

Figure 5.61 NaI baseline performance results: charge-sensitive mode, τ = 0.4 μs. Shown in pC (left) and peak-normalized arbitrary units (right).

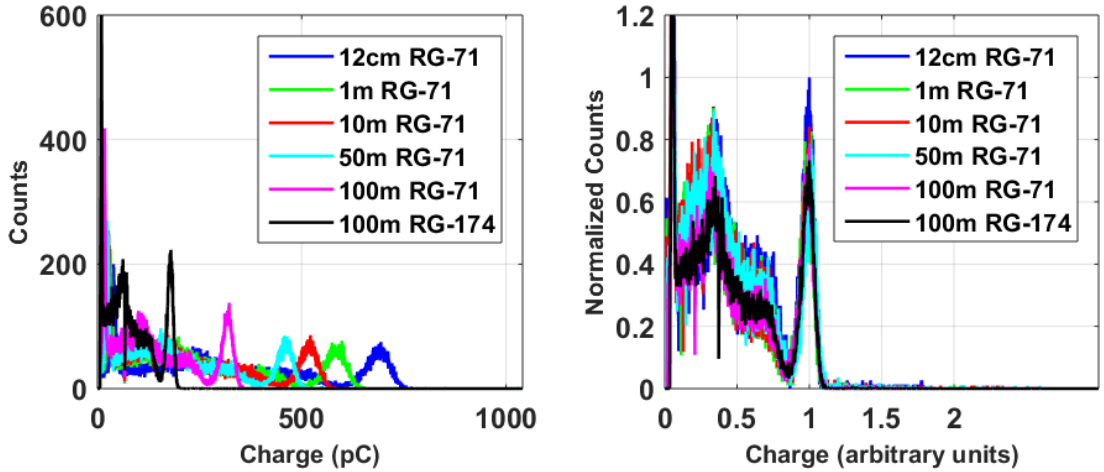

Figure 5.62 NaI baseline performance results: charge-sensitive mode, τ = 2.4 μs. Shown in pC (left) and peak-normalized arbitrary units (right).

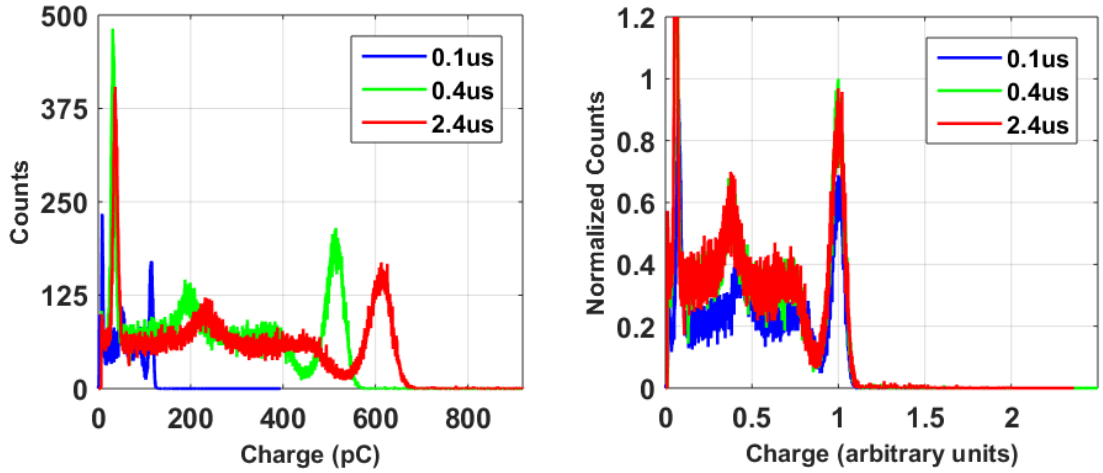

Figure 5.63 NaI baseline performance results: current-sensitive mode, 12 cm RG-71 cable. Shown in pC (left) and peak-normalized arbitrary units (right).

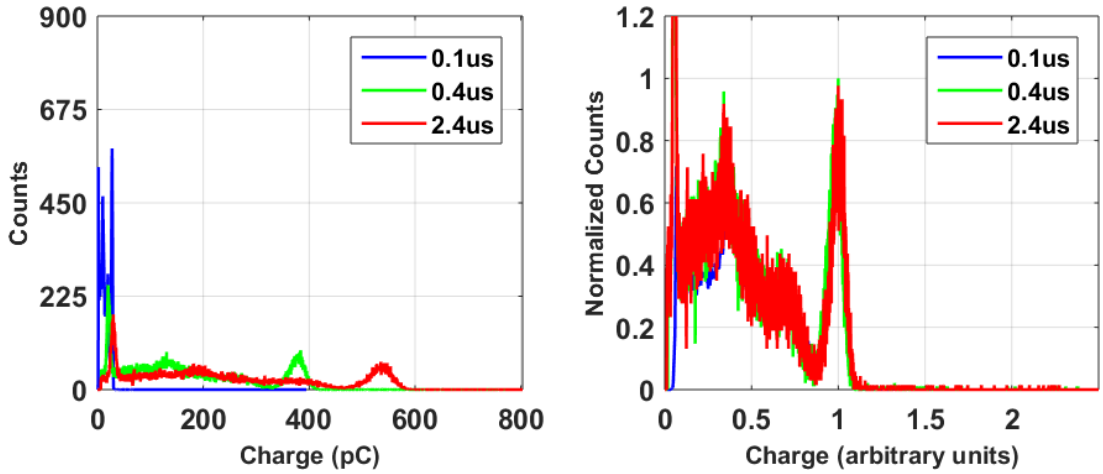

Figure 5.64 NaI baseline performance results: current-sensitive mode, 10 m RG-71 cable. Shown in pC (left) and peak-normalized arbitrary units (right).

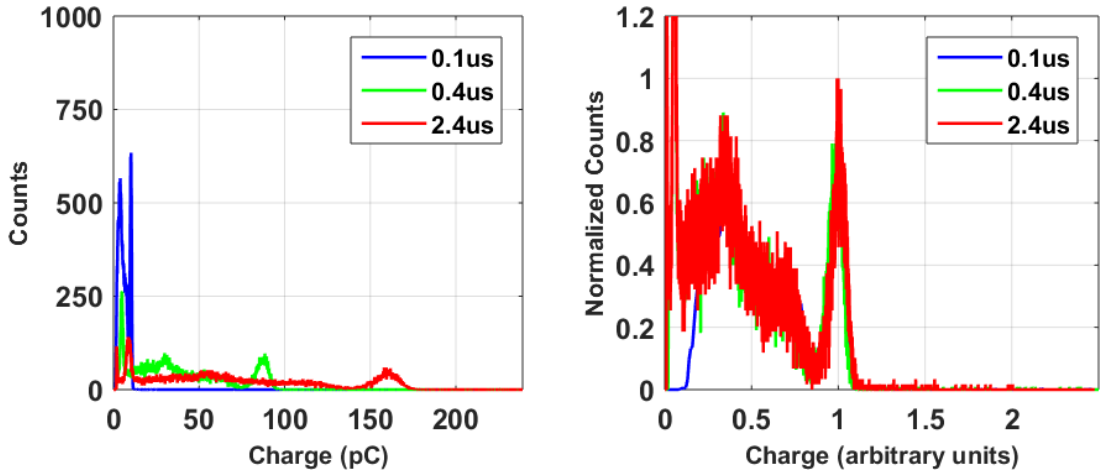

Figure 5.65 NaI baseline performance results: current-sensitive mode, 100 m RG-71 cable. Shown in pC (left) and peak-normalized arbitrary units (right).

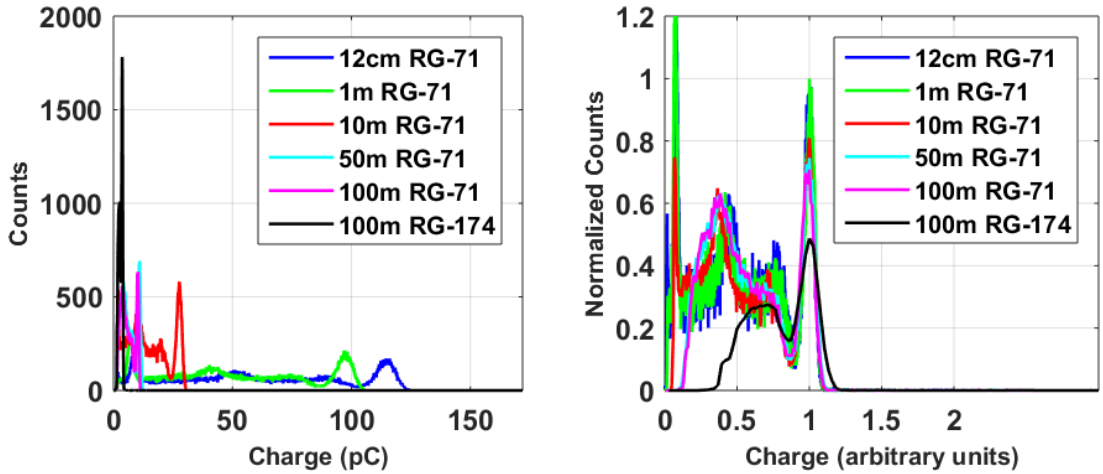

Figure 5.66 NaI baseline performance results: current-sensitive mode, $\tau = 0.1$ µs. Shown in pC (left) and peak-normalized arbitrary units (right).

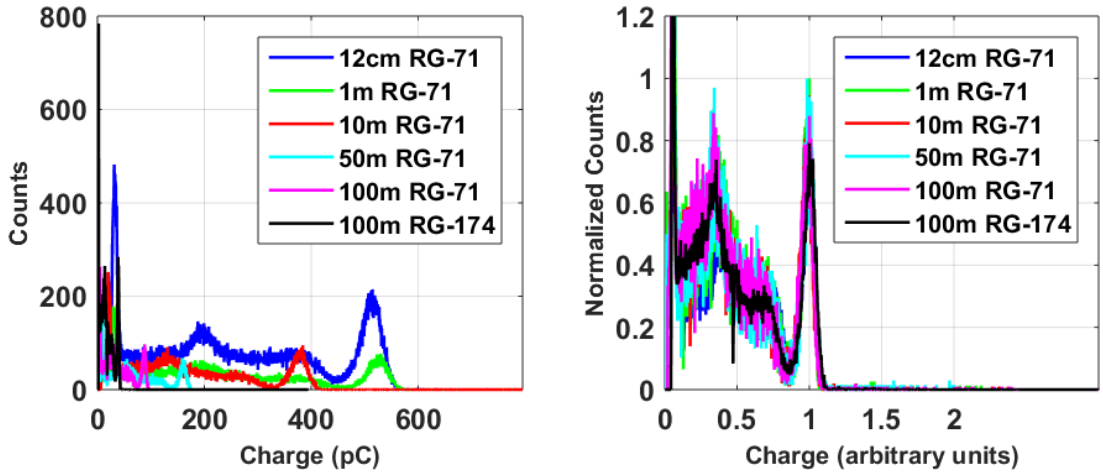

Figure 5.67 NaI baseline performance results: current-sensitive mode, τ = 0.4 μs. Shown in pC (left) and peak-normalized arbitrary units (right).

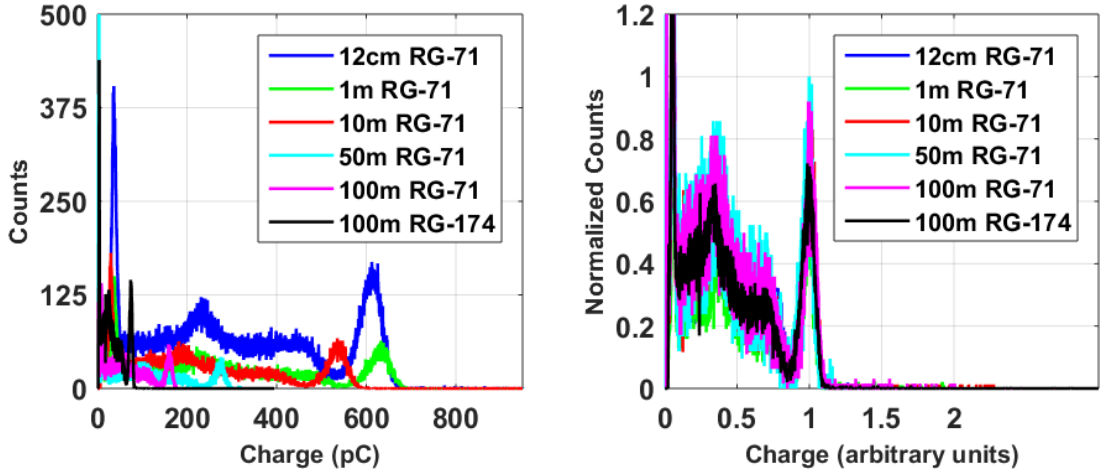

Figure 5.68 NaI baseline performance results: current-sensitive mode, τ = 2.4 μs. Shown in pC (left) and peak-normalized arbitrary units (right).

Test Results: Pass. The baseline performance for the DUT coupled to a NaI(Tl) detector is generally consistent with expectations, including relatively clean spectroscopic performance in even the most challenging cases with short shaping times and long cables. The relatively high amount of charge produced by a PMT / NaI(Tl) combination makes signal degradation in long cables less problematic than for 3He. The lack of ballistic deficit effects in NaI(Tl), as compared to 3He, are a significant factor in maintaining strong performance even at short shaping times. Performance in charge-sensitive mode was marginally better than for current-sensitive, in terms of the noise floor and FWHM.

NaI(Tl) results and trends were as expected except for the cases with 50 m and 100 m RG-71 cables and 0.1 μs shaping time. The unexpectedly low noise floor and high peak centroid location are not understood. Errors in the testing configuration or data distillation may be to blame.

Test 20: RADIATED EMI/RFI SUSCEPTIBILITY – SECTION C.13

This test measures the performance of DUT with respect to input signal, cable length, cable type and analog shaping time while being exposed to radiated EMI/(RFI) radio frequency interference signals. All testing was done in an anechoic chamber to reduce electromagnetic background, in accordance with MIL-STD-461E, reference RS103. A matrix of analog shaping times and cable lengths were tested. Signal generators included the AWG, a ^{3}He proportional counter exposed to ^{252}Cf, and a NaI(Tl) scintillator exposed to ^{137}Cs.

For the AWG, a broad range of EMI frequencies were tested, from 100 MHz to 2 GHz. For the three radiation sensors, only frequencies from 700 MHz to 2 GHz were tested, as specified in MIL-STD-461E, reference RS103. In the results below, '0MHz' refers to no injected noise (i.e. EMI generator output is disabled).

Figure 5.69 EMI test setup with whip antenna.

Table 5.32 Antenna far field distance.

f(MHz)	Antenna Length (m)	Distance (cm)
100	0.75	37.5
200	0.7	65
300	0.7	98
400	0.7	130
500	0.7	163

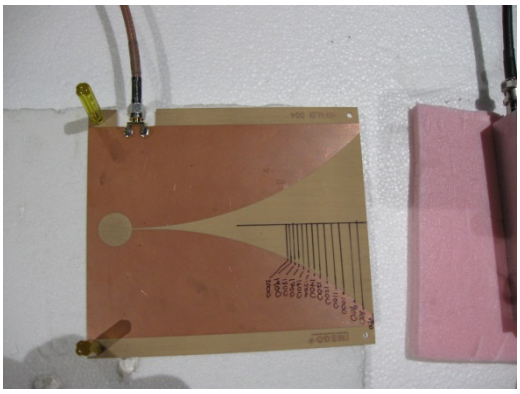

Figure 5.70 EMI test setup with Vivaldi antenna.

Table 5.33 Antenna far field distance.

f(MHz)	Distance (cm)
700	10.5
1000	15
1500	22.5
2000	30

ARBITRARY WAVEFORM GENERATOR (AWG)

The DUT settings used are listed in Table 5.34 below.

Table 5.34 DUT settings for Test 20, AWG EMI.

Parameter	**Setting**	**Value**
Charge Gain	L	1.9-68 mV/pC
G2 – Gain	C	21.67
G3 – Gain	A	
HVH - High Voltage	0	400 V
HVL - High Voltage	0	
DH – Discriminator High	1	360 mV
DL – Discriminator Low	8	
SW4 – TTL Pulse Width	001	200 ns
Detector Source Impedance	330 kΩ	
Precision Capacitor	2200 pF	
Count Time	60 seconds	

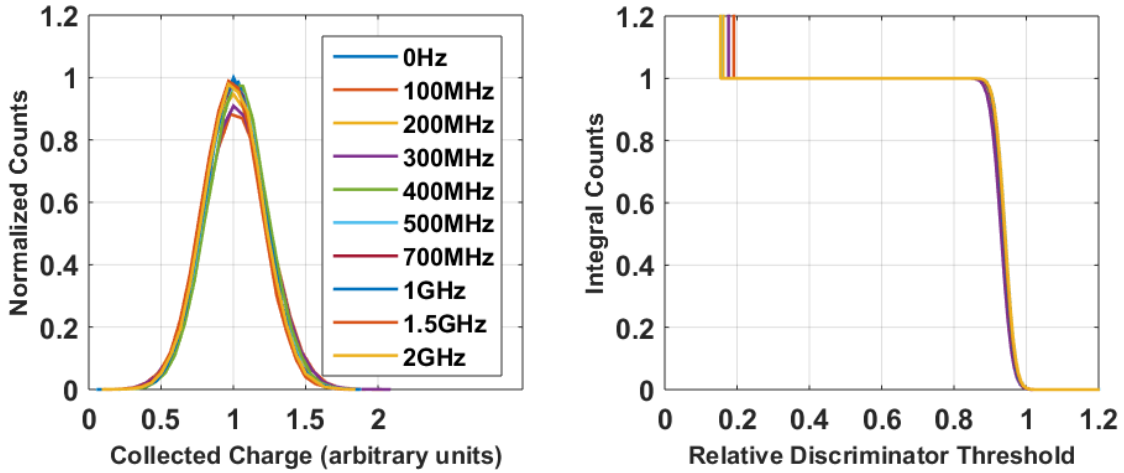

Figure 5.71 AWG radiated EMI results: charge-sensitive mode, 12 cm RG-71 cable, τ = 0.1µs.

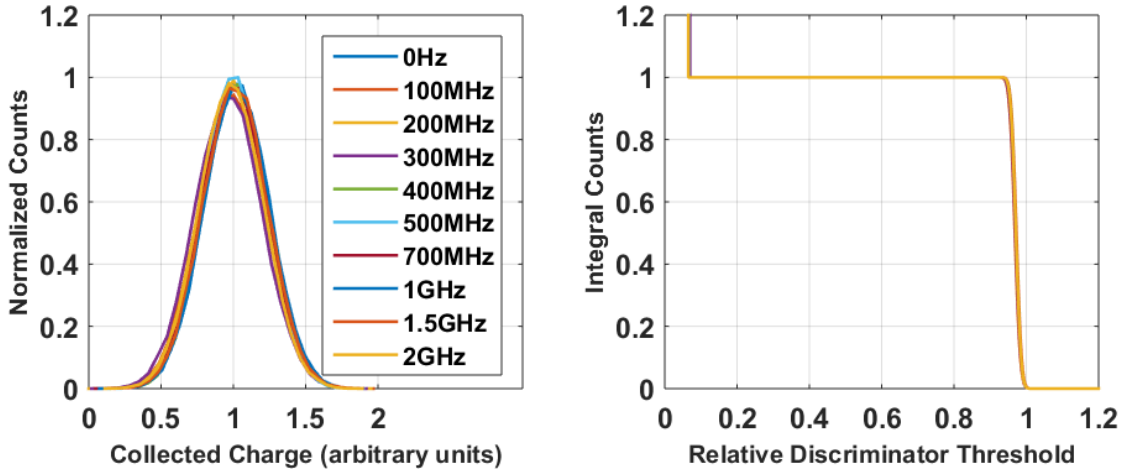

Figure 5.72 AWG radiated EMI results: charge-sensitive mode, 12cm RG-71 cable, τ = 0.4µs.

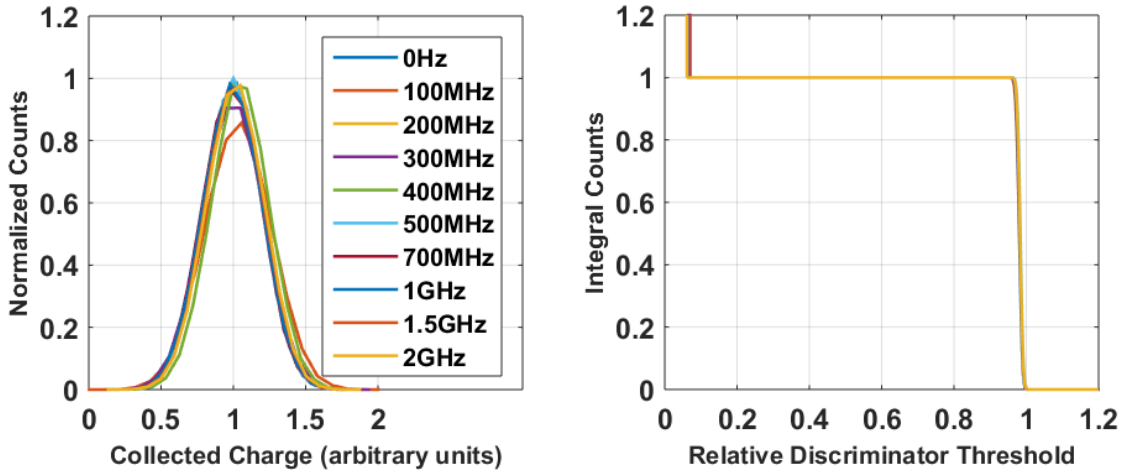

Figure 5.73 AWG radiated EMI results: charge-sensitive mode, 12 cm RG-71 cable, τ = 2.4µs.

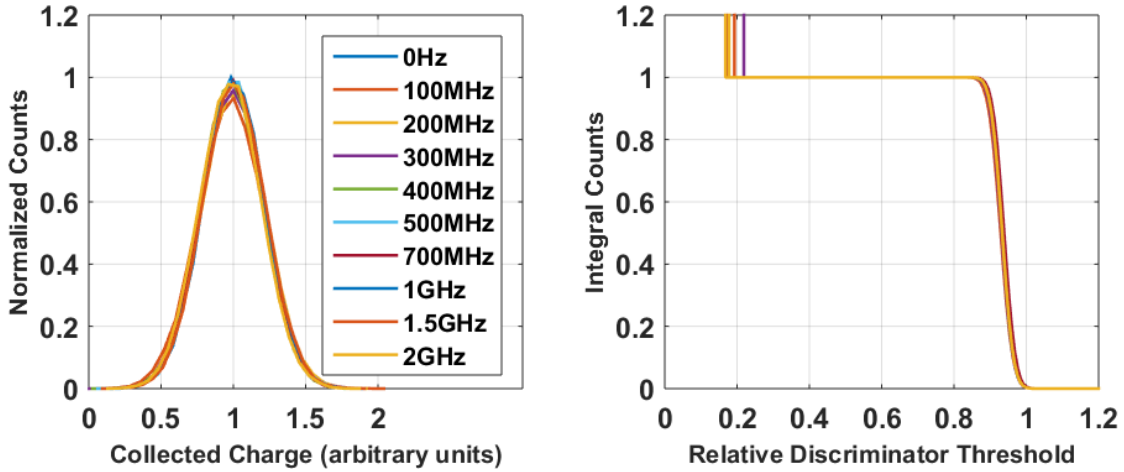

Figure 5.74 AWG radiated EMI results: charge-sensitive mode, 100 m RG-71 cable, τ = 0.1µs.

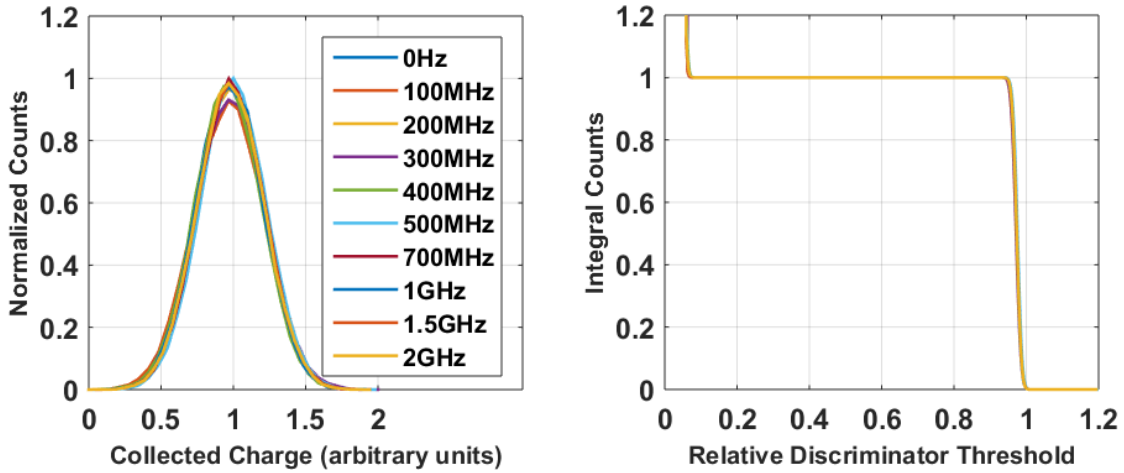

Figure 5.75 AWG radiated EMI results: charge-sensitive mode, 100 m RG-71 cable, τ = 0.4µs.

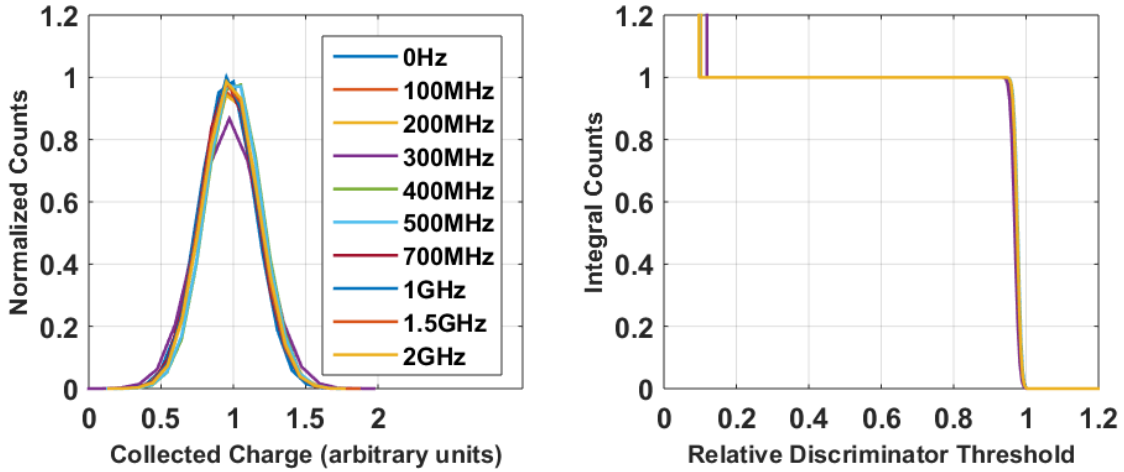

Figure 5.76 AWG radiated EMI results: charge-sensitive mode, 100 m RG-71 cable, τ = 2.4µs.

^{3}He Proportional Counter

The DUT settings used are listed in Table 5.35 below.

Table 5.35 DUT settings for Test 20, ^{3}He proportional counter EMI.

Parameter	Setting	Value
Charge Gain	H	1.9-70 V/pC
G2 – Gain	8	13.44
G3 – Gain	8	
HVH - High Voltage	D	1750 V
HVL - High Voltage	8	
DH – Discriminator High	1	360 mV
DL – Discriminator Low	8	
SW4 – TTL Pulse Width	001	200 ns
Detector Source Impedance	10 MΩ	
Count Time	60 seconds	
Detector Model	RS-P4-0825-203	
Source	20 µCi Cf-252	

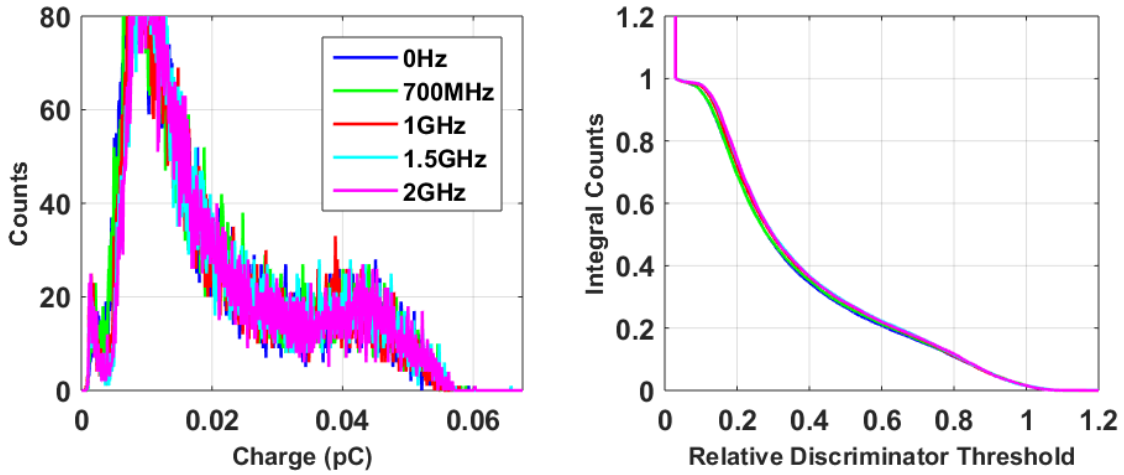

Figure 5.77 ^{3}He radiated EMI results: charge-sensitive mode, 12 cm RG-71 cable, τ = 0.1µs.

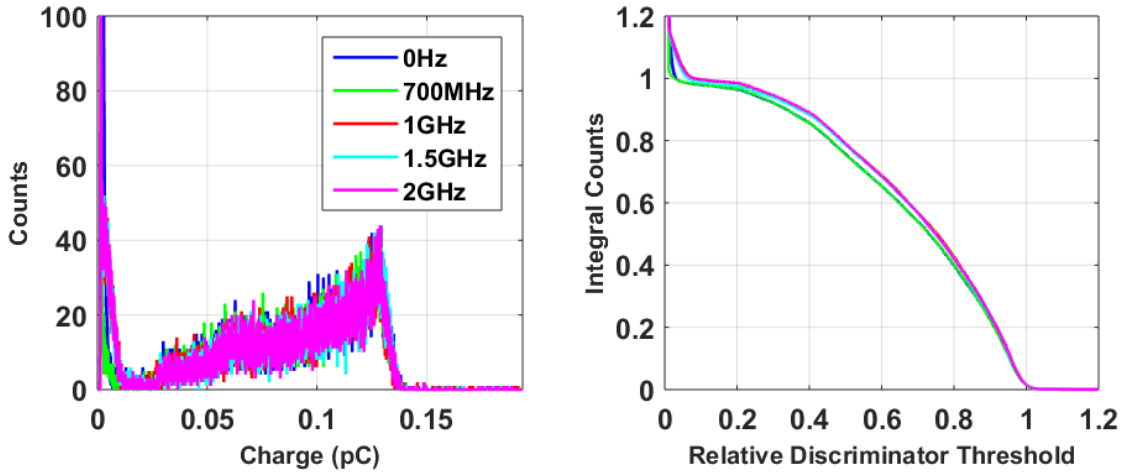

Figure 5.78. ^{3}He radiated EMI results: charge-sensitive mode, 12 cm RG-71 cable, τ = 0.4µs.

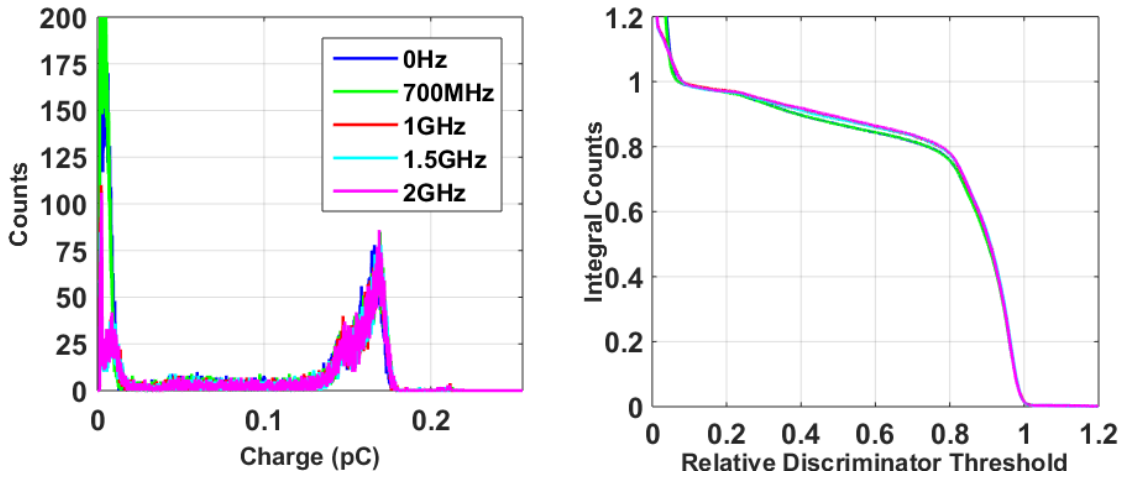

Figure 5.79. ^{3}He radiated EMI results: charge-sensitive mode, 12 cm RG-71 cable, τ = 2.4µs.

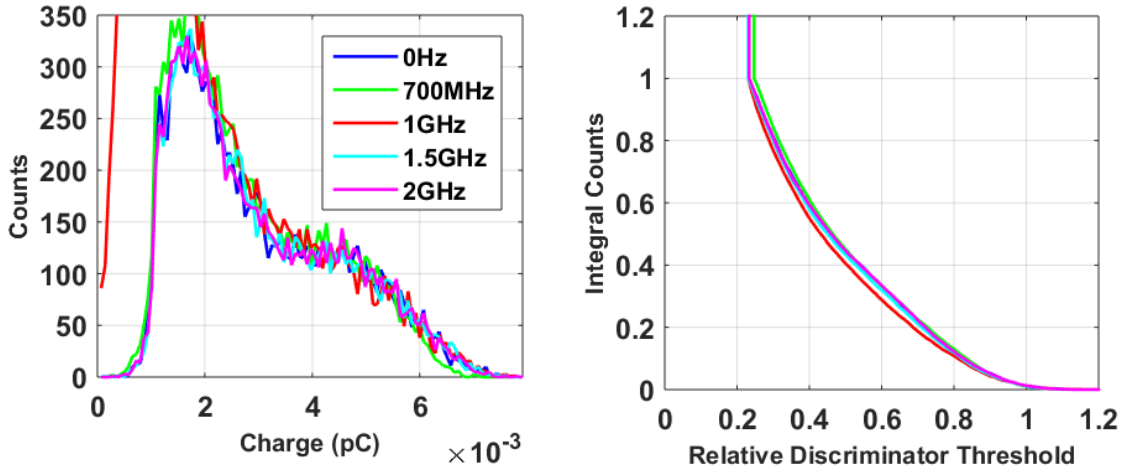

Figure 5.80. ^{3}He radiated EMI results: charge-sensitive mode, 100 m RG-71 cable, τ = 0.1µs.

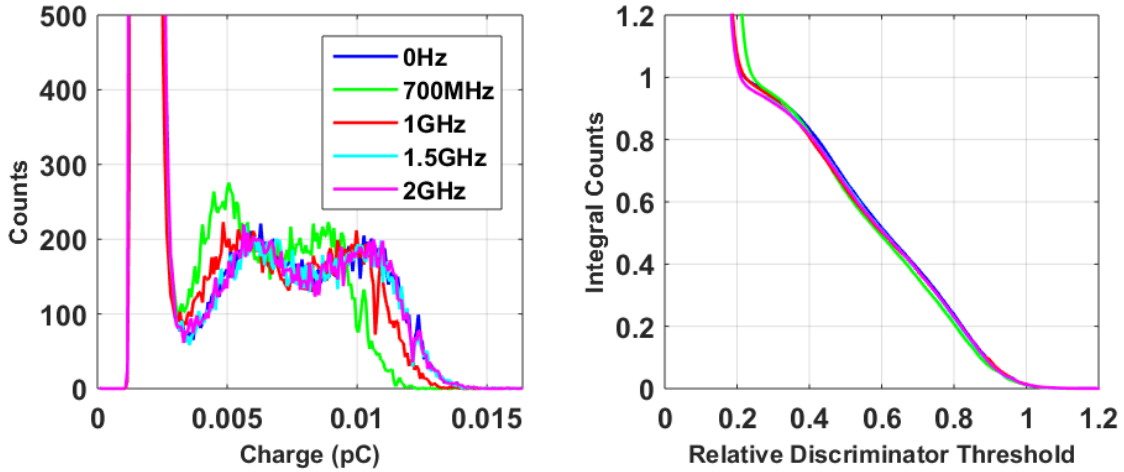

Figure 5.81 ^{3}He radiated EMI results: charge-sensitive mode, 100 m RG-71 cable, τ = 0.4µs.

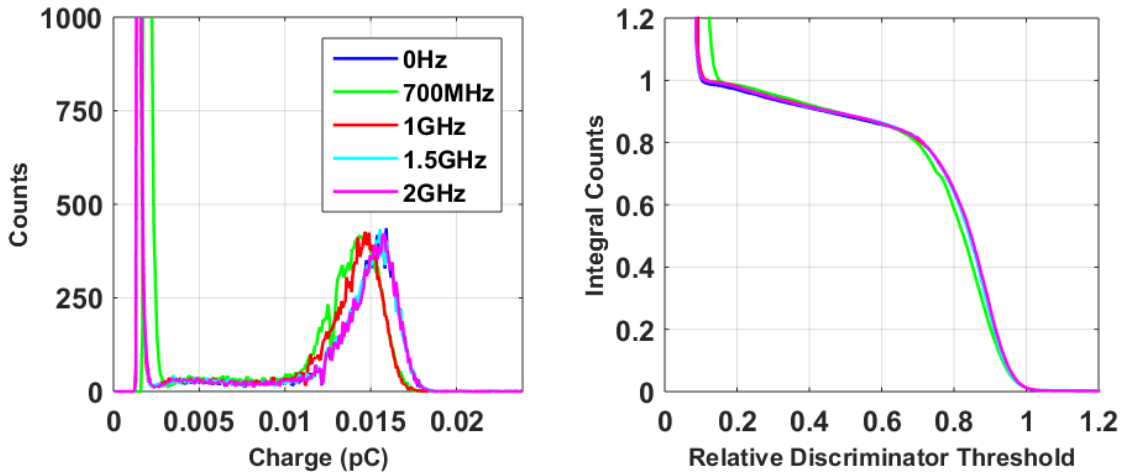

Figure 5.82 ^{3}He radiated EMI results: charge-sensitive mode, 100 m RG-71 cable, τ = 2.4µs.

NAI(TL) SCINTILLATOR

The DUT settings used are listed in Table 5.36 below.

Table 5.36 DUT settings for Test 20, NaI (Tl) scintillator EMI.

Parameter	**Setting**	**Value**
Charge Gain	L	1.9-68 mV/pC
G2 – Gain	C	21.67
G3 – Gain	A	
HVH - High Voltage	3	750 V
HVL - High Voltage	8	
DH – Discriminator High	1	360 mV
DL – Discriminator Low	8	
SW4 – TTL Pulse Width	001	200 ns
Detector Source Impedance	330 kΩ	
Count Time	60 seconds	
Detector Model	Ludlum 44-2	
Source	9.66 µCi Cs-137	

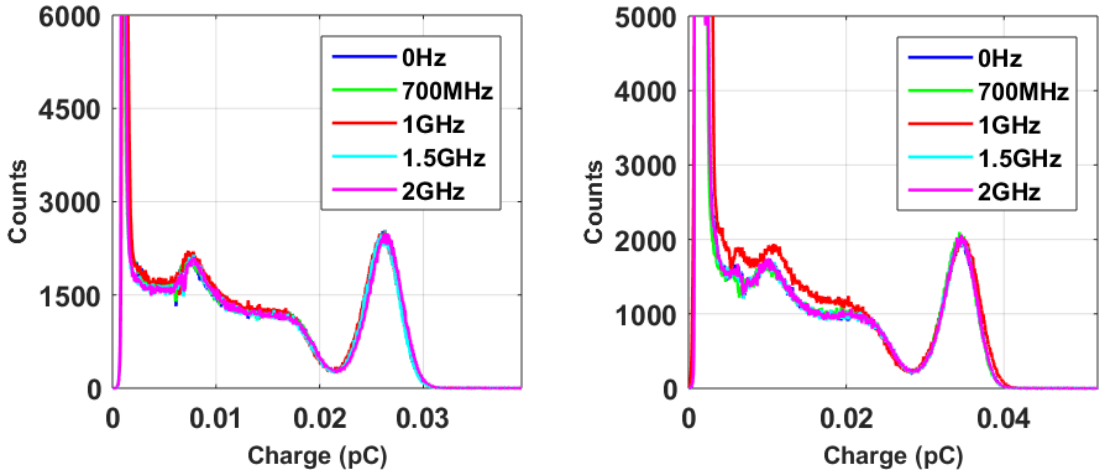

Figure 5.83 NaI radiated EMI results: charge-sensitive mode, τ = 0.1μs. 12 cm RG-71 cable (left) and 100 m RG-71 cable (right).

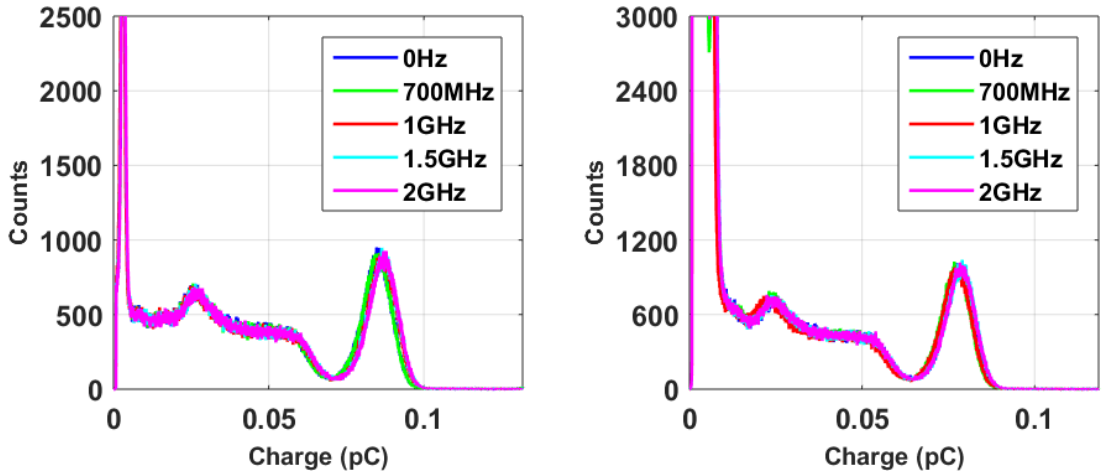

Figure 5.84 NaI radiated EMI results: charge-sensitive mode, τ = 0.4μs. 12 cm RG-71 cable (left) and 100 m RG-71 cable (right).

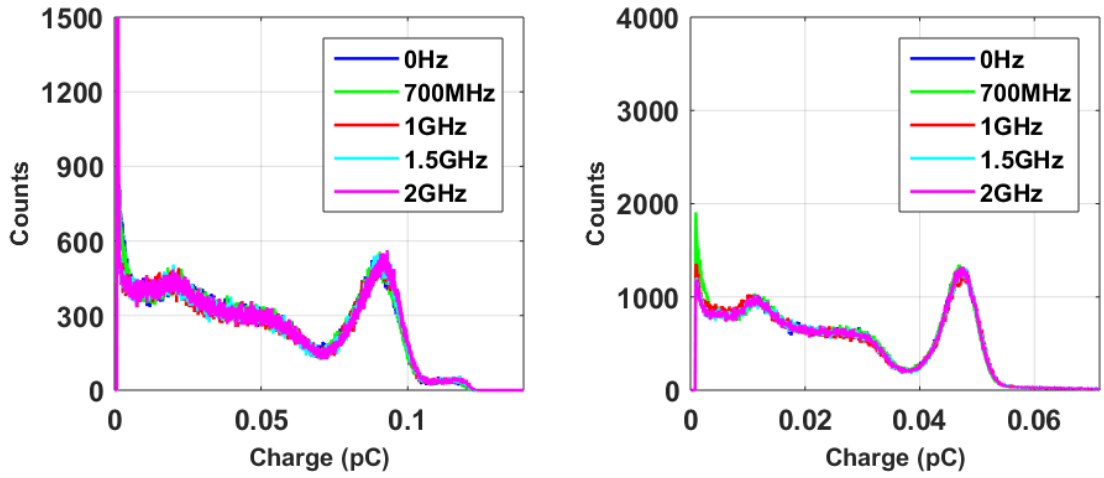

Figure 5.85 NaI radiated EMI results: charge-sensitive mode, τ = 2.4μs. 12 cm RG-71 cable (left) and 100 m RG-71 cable (right).

Test Result: Pass. The performance of the DUT in radiated EMI conditions was, generally speaking, unchanged from the baseline performance, indicating that the FEUM prototypes are robust against ambient EMI conditions over a broad range of frequencies. This statement pertains to the DUT when coupled to the AWG, ^{3}He and NaI(Tl) signal generators. The exception to this statement is for 0.4 μs shaping time when coupled to the ^{3}He detector. Degradation of the DPHS and IPHS is evident, when compared to the baseline performance. The reasons for this exception are not understood; errors in the experimental configuration or data distillation cannot be ruled out.

Test 21: CONDUCTED EMI/RFI SUSCEPTIBILITY – SECTION C.14

Following the completion of the Test Plan, it was decided that there was limited value in such a test if the focus is on the viability of the DUT itself, rather than a complete UMS systems that includes power supply. The logic for this decision is described here.

In conducted EMI tests, the EMI is generally conducted into the DUT through the power supply, since this is the most common path for conductive interference to couple onto powered devices such as the FEUM prototype. Because the FEUM is powered via an externally supplied AC/DC power supply, the rejection of noise is highly dependent on the power supply chosen, which is outside the scope of the FEUM testing. In summary, conducted EMI can be considered a system-level test, while the FEUM evaluation is focused on component-level tests.

Test Result: Not Performed.

Test 22: GROUND LOOP NOISE SUSCEPTIBILITY – SECTION C.15

Following the completion of the Test Plan, it was decided that there was limited value in such a test if the focus is on the viability of the DUT itself. That is, ground-loop issues are highly dependent on the facility's power supply and grounding conditions far removed from the FEUM device, for example at the sensor and cabinet locations. Ground-loop tests can be considered a system-level test, while the FEUM evaluation is focused on component-level tests.

Test Result: Not Performed.

Test 23: DEAD TIME

The dead-time behavior of the prototype FEUM device was evaluated across different analog shaping times (τ), and digital output pulse widths (PW), for the discriminator. Three measurement methods were used: 1) random pulse generator intended to be generically representative of IAEA UMS sensors, 2) "two-source method" using a NaI(Tl) detector and gamma-ray sources to represent gamma-ray sensors, and 3) a "time-interval histogram" method applied to a ^{3}He detector, to represent UMS neutron sensors that must often operate in high gamma-ray fields.

The first method uses the true interaction rate and recorded count rate to determine the dead time. These two rates are measured directly as described in the test plan [3]. A graphical representation of the data are presented in Figure 5.86. Using the paralyzable and non-paralyzable models a value for the dead time was calculated and presented in Table 5.37 and Table 5.38.

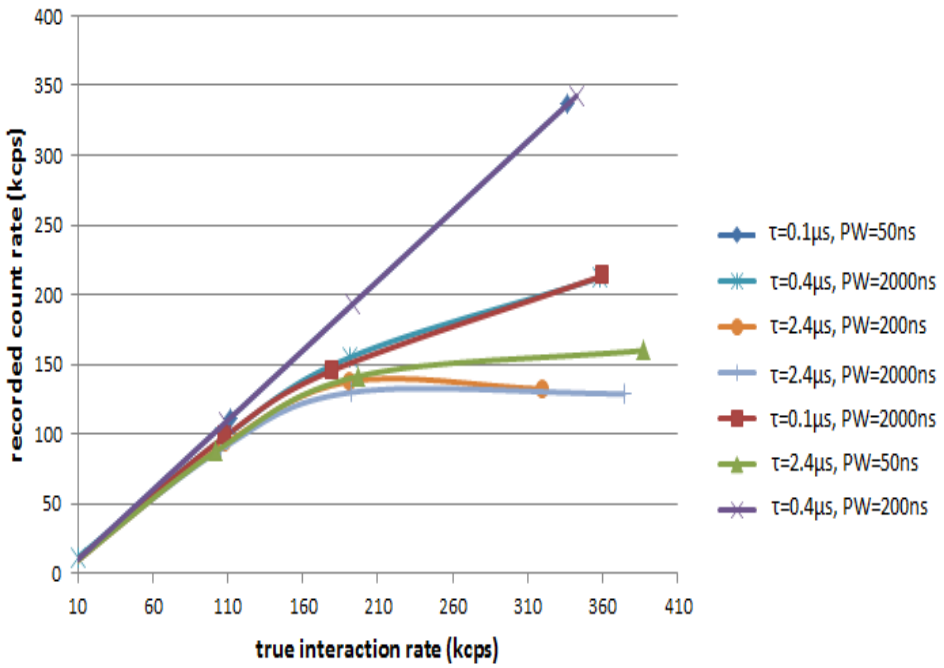

Figure 5.86 Dead time measurements for the random pulse generator method (method 1). τ is analog shaping time and PW is TTL digital pulse width.

Table 5.37 Nonparalyzable Dead time in μs using method 1. Blank values were not measured.

	Digital Pulse Width (ns)		
Analog Shaping Time (μs)	50	200	2000
0.1	0.0		1.9
0.4			1.9
2.4	3.7	4.4	5.1

Table 5.38 Paralyzable Dead time in μs using method 1. Blank values were not measured.

	Digital Pulse Width (ns)		
Analog Shaping Time (μs)	50	200	2000
0.1	0.0		1.5
0.4			1.5
2.4	2.3	2.8	2.8

The second method (“two-source method”) yields only one value for the non-paralyzable model. Table 5.39 below shows the results of this test measured in microseconds.

Table 5.39 FEUM dead time results using the two-source method (method 2) and non-paralyzable model. Results are in µs.

	Digital Pulse Width (ns)	
Analog Shaping Time (µs)	50	2000
0.1	3.0	4.7
2.4	11.6	10.6

The third method ("time interval method") yields a histogram that can be analyzed to determine the dead time of the system. The lower edge of the histogram is the effective dead time of the system.

Table 5.40 FEUM dead time results using the time interval histogram method (method 3). Results are in µs.

	Digital Pulse Width (ns)		
Analog Shaping Time (µs)	50	600	2000
0.1	0.6	0.6	1.8
0.4	1.5		1.8
2.4	6.3	6.3	6.4

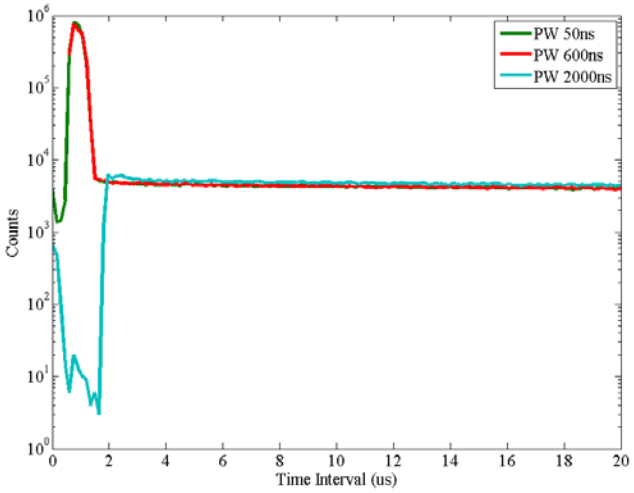

Figure 5.87 Time Interval Histogram with analog shaping time of 0.1 µs. The short time interval peak is due to double pulsing as described in [5]. The short intervals on 2000 ns digital pulse width is most likely due to the problem identified in: TTL Pulse Width – Section C.4.

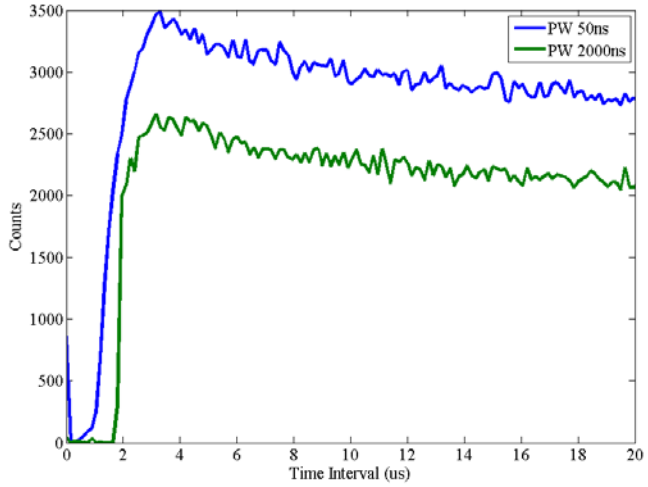

Figure 5.88 Time Interval Histogram with analog shaping time of 0.4 µs.

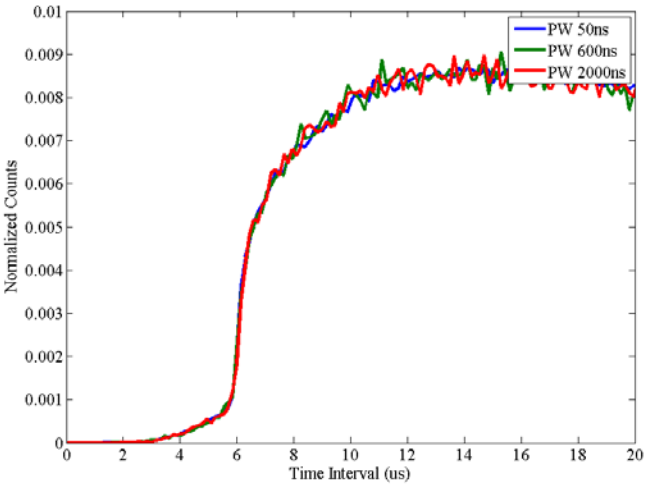

Figure 5.89 Time interval histogram with analog shaping time of 2.4 µs.

The dead-time results above provide quantitative verification that dead-time behavior of the DUT is consistent with expectations. For example, the analog pulse width for a bipolar pulse, as implemented by Bot Engineering, is approximately twice the shaping-time value (varied from 0.1 to 2.4 µs in this testing), and the prototype exhibited dead-time behavior consistent with this pulse-width relationship. The dead time of the digital output was consistent with the user-selected digital pulse width—50, 200 or 2000 ns in this testing. When one of the pulse widths (analog or digital) was significantly longer than the other, the dead-time behavior tends to be consistent with the longer of the pair. When they are comparable, the dead-time is marginally longer than both. The time-interval histogram method, as applied to the ^{3}He detector, showed the effects of double-pulsing at short shaping times, for example 0.1 µs. This result is consistent with prior investigation performed by Los Alamos National Laboratory on double-pulsing in commercially available pulse-processing electronics used in IAEA measurement systems [5].

Test Result: Pass. The dead time is consistent with the device settings and demonstrates phenomenon previously investigated by others.

Test 24: EQUIVALENT NOISE CHARGE

The equivalent noise charge (ENC) evaluation is a basic characterization of instrument noise levels, at a given shaping time and input capacitance. With this ENC data, the IAEA can make predictions of noise level versus cable length for each specific unattended monitoring system (UMS) installation. Evaluation measurements were performed in a manner consistent with open-literature protocols [4]. The ENC characterization test used the AWG as the signal generator and included variation of the shaping time and input capacitance across a wide range of values representative of IAEA UMS scenarios. This test mimics the added capacitance of long coaxial cables by adding capacitors in parallel with the standard 12cm RG-71 cable used for ideal measurements and measuring the noise. The DUT was set to the maximum gain setting (70 V/pC).

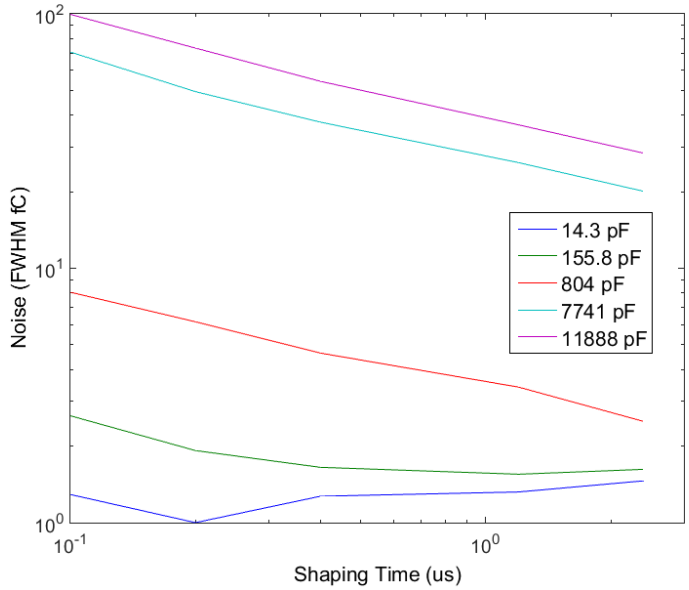

Figure 5.90 Analog shaping time vs noise with 70V/pC gain.

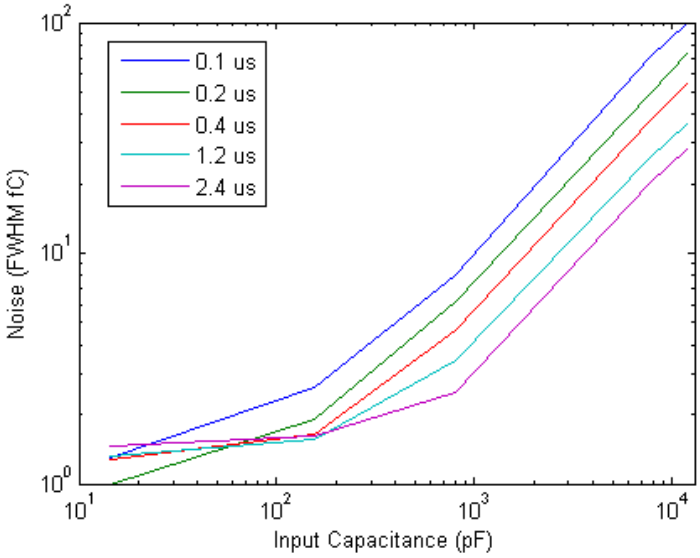

Figure 5.91 Input capacitance vs noise with 70V/pC gain.

The general trends of the ENC for the FEUM prototype Figure 5.90 and Figure 5.91 are consistent with expectations. For example, the ENC decreases with increasing shaping time but increases linearly with input capacitance. In absolute terms, the ENC of the prototype with low external capacitance and long shaping times is approximately 1 fC. This is somewhat higher than commercial off-the-shelf (COTS) low-noise preamplifiers used in high-resolution spectroscopy (~0.2 fC), but consistent with the needs of a FEUM design focused on pulse-counting applications and applicability to a broad range of sensor types, rather than higher-resolution spectroscopy applications.

Test Result: Pass.

Test 25: HIGH RADIATION FIELD SUSCEPTIBILITY

This test measures the performance of the DUT when coupled to neutron detectors are exposed to high gamma-ray radiation fields. A matrix of analog shaping times and cable lengths were tested using a ^{3}He proportional counter and a ^{235}U fission chamber exposed to a ^{252}Cf source (70 μCi) while simultaneously being exposed to a large ^{60}Co source. In the results below, 0 R/hr. refers to a low-exposure situation comparable to the baseline testing described in Test 19.

While the range of dose rates available for this testing is relatively broad, it is unfortunate that it required two different testing configurations, and a relatively large exposure-rate gap arises. For exposure rates up to 1.2 R/hr, the evaluation was performed over a gamma-ray well facility (Figure 5.92). Radiation exposure rate was increased by raising the source using a computer controlled pulley system, bringing it closer to the neutron sensors located at the top of the well. For exposure rates greater than or equal to 10 R/hr, PNNL's High Exposure Facility (HEF) was utilized (Figure 5.93). Gamma exposure rate was adjusted by changing the distance between a test trolley containing the source, and the neutron sensors.

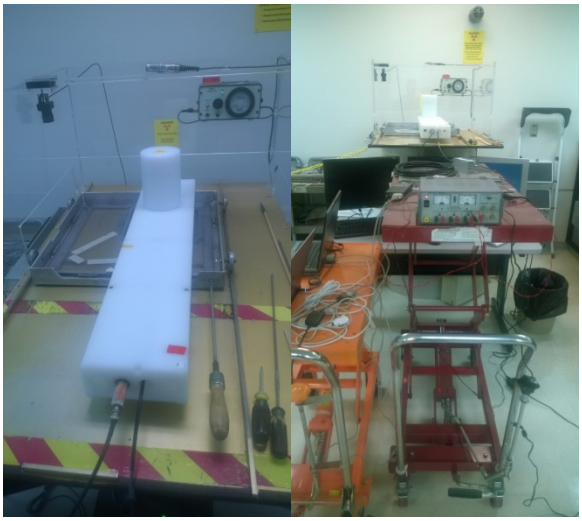

Figure 5.92 Test setup over gamma source well.

NOTE: the images above show ^{3}He and U-235 Fission Chambers in adjacent columns within the high density polyethylene (HDPE) blocks.

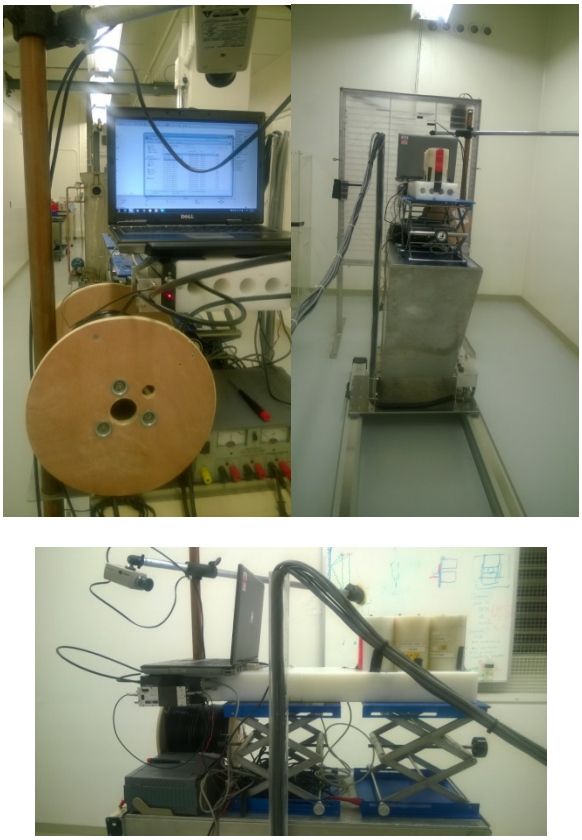

Figure 5.93 Test setup in HEF.

^{3}HE PROPORTIONAL COUNTER

The DUT settings used are listed in Table 5.41 below.

Table 5.41 DUT settings for Test 25, ^{3}He proportional counter, high radiation field.

Parameter	**Setting**	**Value**
Charge Gain	H	1.9-70 V/pC
G2 – Gain	C	18.33
G3 – Gain	8	
HVH - High Voltage	D	1750 V
HVL - High Voltage	8	
DH – Discriminator High	1	360 mV
DL – Discriminator Low	8	
SW4 – TTL Pulse Width	001	200 ns
Detector Source Impedance	10 MΩ	
Detector Model	RS-P4-0825-203	
Count Time	60 seconds	

Table 5.42 ^{3}He high radiation test count rates in charge mode for several exposure rates versus fixed cable lengths and analog shaping times (τ).

Cable	Shaping	Exposure	Counts
RG-71 1m	0.1 µs	0 mR/hr.	117682
RG-71 1m	0.1 µs	80 mR/hr.	172028
RG-71 1m	0.1 µs	500 mR/hr.	496005
RG-71 1m	0.1 µs	1.2 R/hr.	1087789
RG-71 1m	0.1 µs	20 R/hr.	19471978
RG-71 1m	0.1 µs	30 R/hr.	27642650
RG-71 1m	0.4 µs	0 mR/hr.	153890
RG-71 1m	0.4 µs	80 mR/hr.	596979
RG-71 1m	0.4 µs	500 mR/hr.	3130664
RG-71 1m	0.4 µs	1.2 R/hr.	7236523
RG-71 1m	0.4 µs	20 R/hr.	11546574
RG-71 1m	0.4 µs	30 R/hr.	13182483
RG-71 1m	2.4 µs	0 mR/hr.	270734
RG-71 1m	2.4 µs	80 mR/hr.	778082
RG-71 1m	2.4 µs	500 mR/hr.	3078656
RG-71 1m	2.4 µs	1.2 R/hr.	5104277
RG-71 1m	2.4 µs	20 R/hr.	2303059
RG-71 1m	2.4 µs	30 R/hr.	1820875

Cable	Shaping	Exposure	Counts
RG-71 100m	0.1 µs	0 mR/hr.	183158
RG-71 100m	0.1 µs	80 mR/hr.	180451
RG-71 100m	0.1 µs	500 mR/hr.	180714
RG-71 100m	0.1 µs	1.2 R/hr.	179779
RG-71 100m	0.1 µs	10 R/hr.	15403130
RG-71 100m	0.1 µs	20 R/hr.	11507982
RG-71 100m	0.1 µs	30 R/hr.	12972370
RG-71 100m	0.4 µs	0 mR/hr.	6913664
RG-71 100m	0.4 µs	80 mR/hr.	6289313
RG-71 100m	0.4 µs	500 mR/hr.	6561557
RG-71 100m	0.4 µs	1.2 R/hr.	6838501
RG-71 100m	0.4 µs	10 R/hr.	32077277
RG-71 100m	0.4 µs	20 R/hr.	29885184
RG-71 100m	0.4 µs	30 R/hr.	29024474
RG-71 100m	2.4 µs	0 mR/hr.	495796
RG-71 100m	2.4 µs	80 mR/hr.	563880
RG-71 100m	2.4 µs	500 mR/hr.	1285480
RG-71 100m	2.4 µs	1.2 R/hr.	2124859
RG-71 100m	2.4 µs	10 R/hr.	6471248
RG-71 100m	2.4 µs	20 R/hr.	6046727
RG-71 100m	2.4 µs	30 R/hr.	6255828

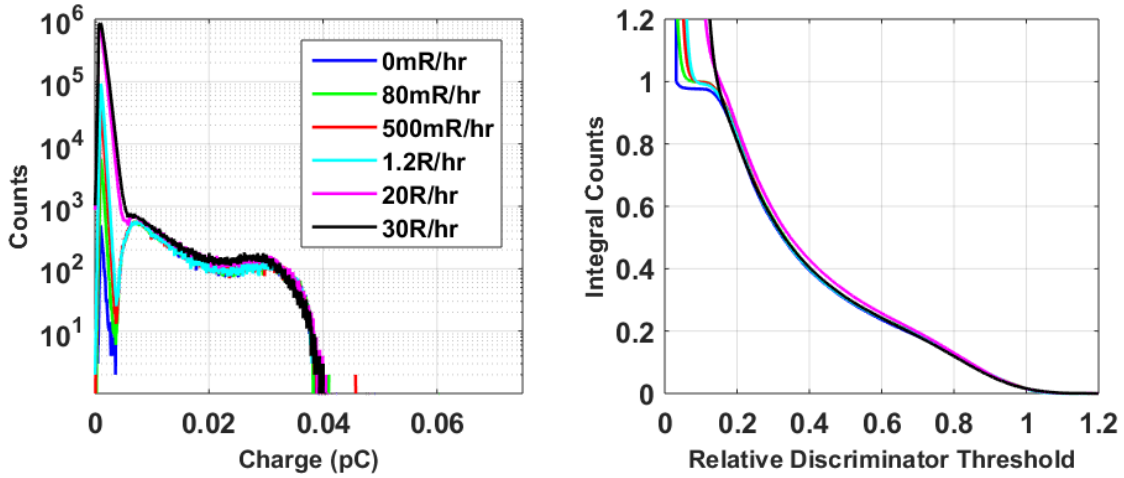

Figure 5.94 ^{3}He high radiation fields results: charge-sensitive mode, 1m RG-71 cable, τ = 0.1µs.

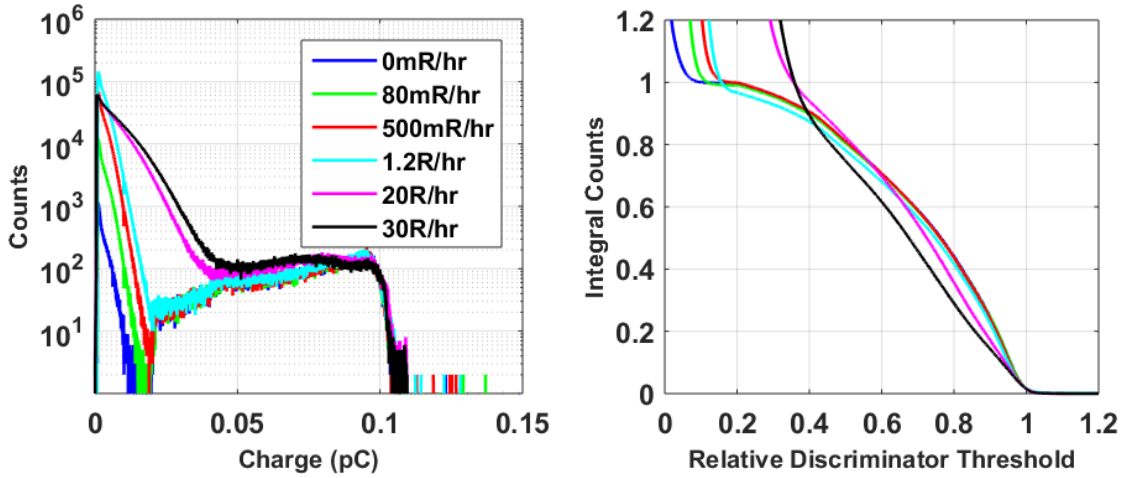

Figure 5.95 ^{3}He high radiation fields results: charge-sensitive mode, 1 m RG-71 cable, τ = 0.4µs.

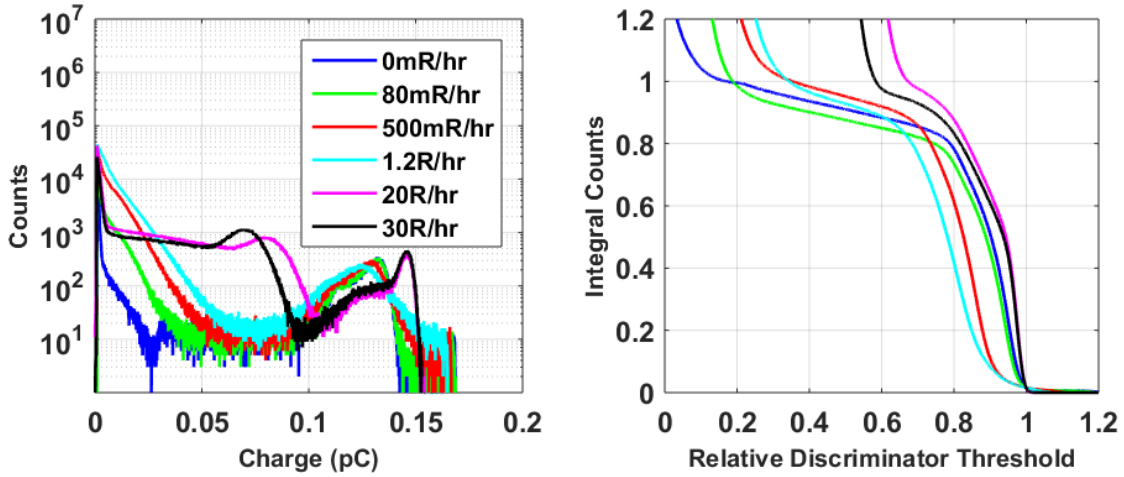

Figure 5.96 ^{3}He high radiation fields results: charge-sensitive mode, 1 m RG-71 cable, τ = 2.4µs. Note that the strange behavior (double peak) for the high dose rate scenarios are not understood. The test team was unable to repeat the high dose rate tests at the HEF.

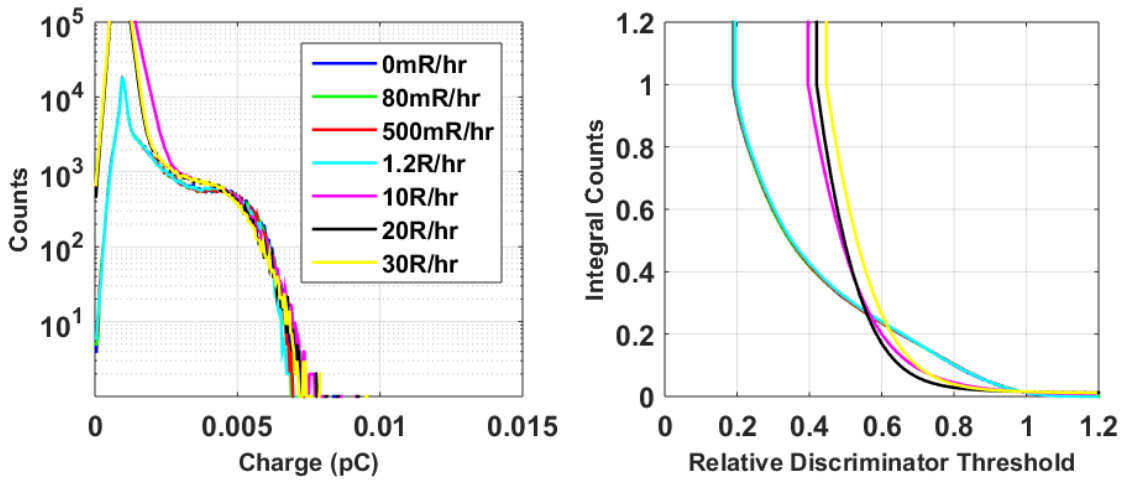

Figure 5.97 ^{3}He high radiation fields results: charge-sensitive mode, 100 m RG-71 cable, τ = 0.1μs.

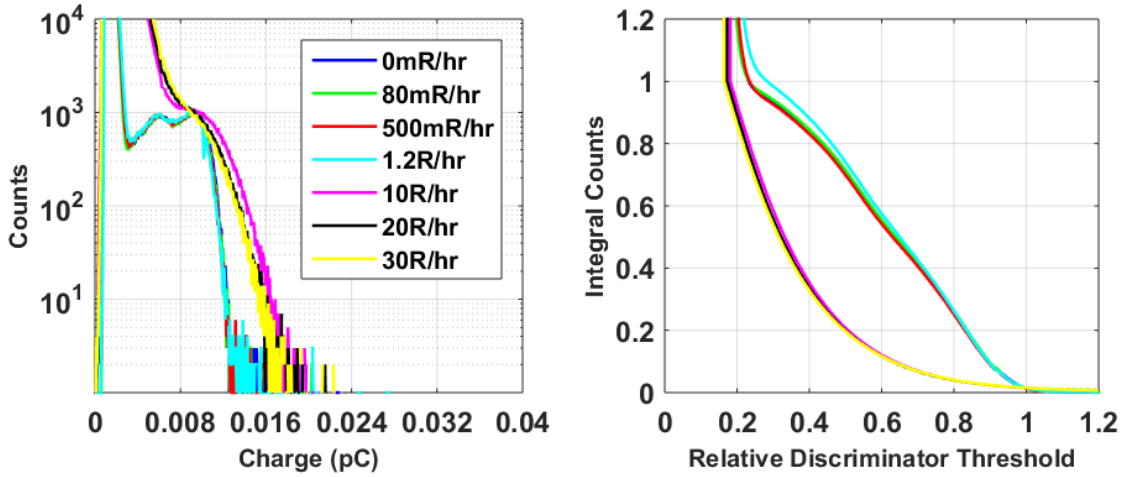

Figure 5.98 ^{3}He high radiation fields results: charge-sensitive mode, 100 m RG-71 cable, τ = 0.4μs.

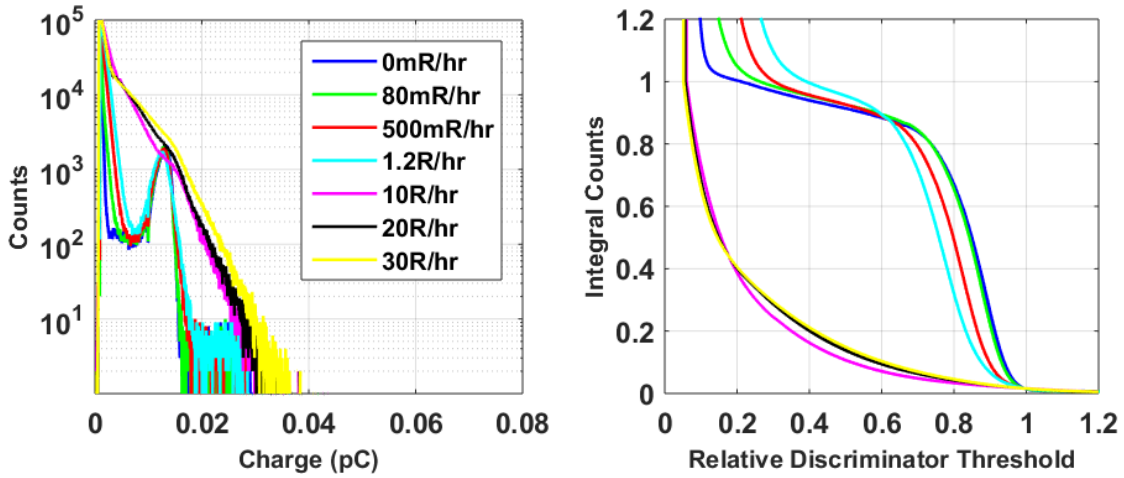

Figure 5.99 ^{3}He high radiation fields results: charge-sensitive mode, 100 m RG-71 cable, τ = 2.4μs.

FISSION CHAMBER

The DUT settings used are shown in Table 5.43 below.

Table 5.43 DUT settings for Test 25, fission chamber, high radiation fields.

Parameter	Setting	Value
Charge Gain	H	1.9-70 V/pC
G2 – Gain	8	13.44
G3 – Gain	8	
HVH - High Voltage	3	750 V
HVL - High Voltage	8	
DH – Discriminator High	1	360 mV
DL – Discriminator Low	8	
SW4 – TTL Pulse Width	001	200 ns
Detector Source Impedance	10 MΩ	
Detector Model	RS-P6-0805-134	
Count Time	300 seconds [3]	

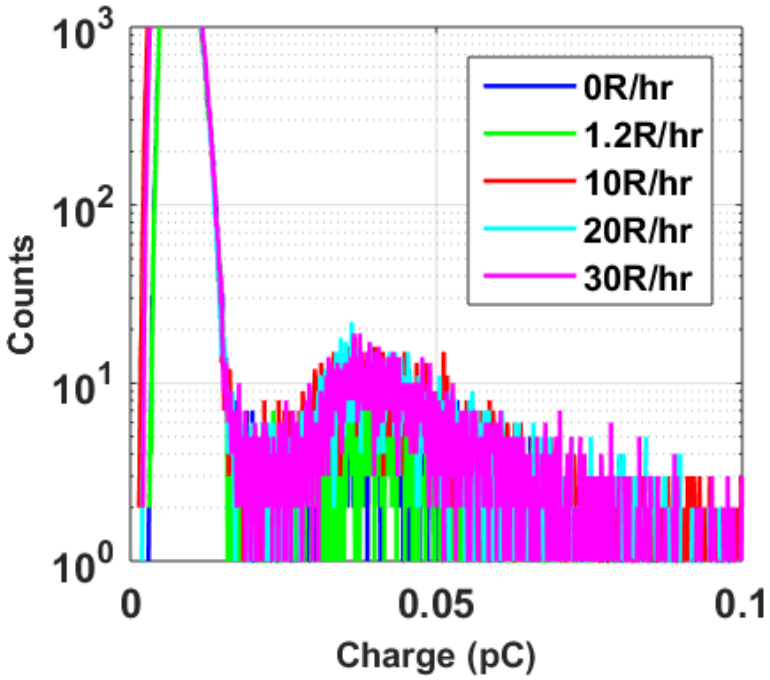

Figure 5.100 FC high radiation fields results: charge-sensitive mode, 1m cable, τ = 0.1µs.

[3] 60 second count time was insufficient to see a peak with the 70 µCi source and larger sources were not available

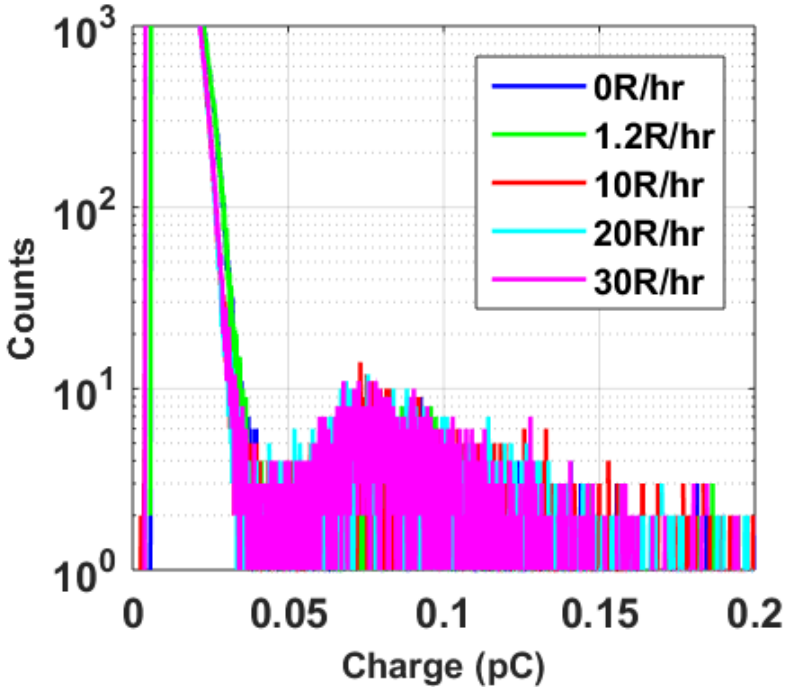

Figure 5.101 FC high radiation fields results: charge-sensitive mode, 1 m cable, τ = 0.4μs.

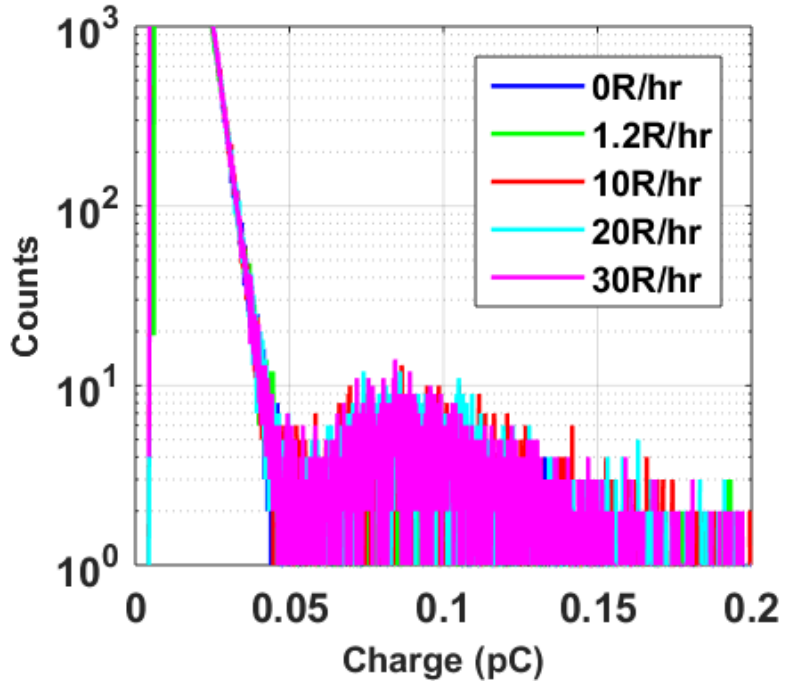

Figure 5.102 FC high radiation fields results: charge-sensitive mode, 1m cable, τ = 2.4μs.

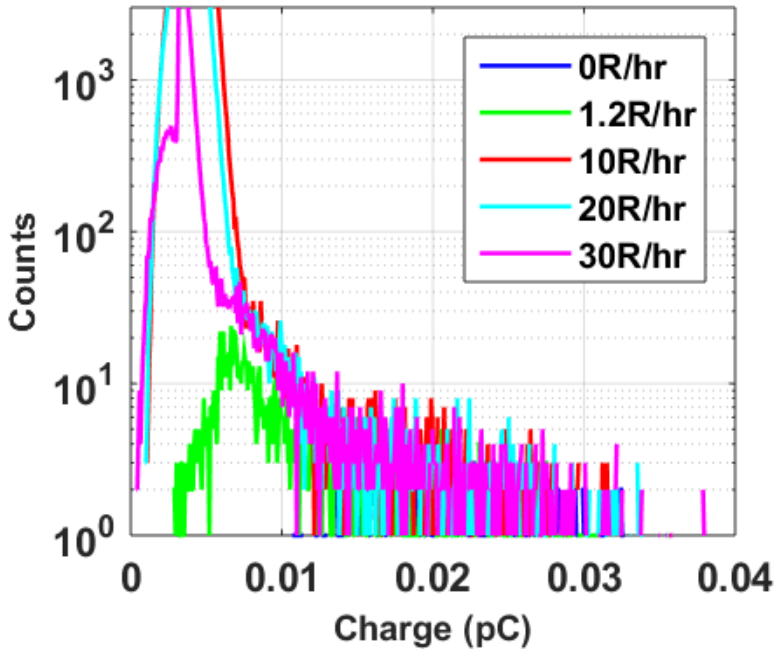

Figure 5.103 FC high radiation fields results: charge-sensitive mode, 100m cable, τ = 0.1μs.

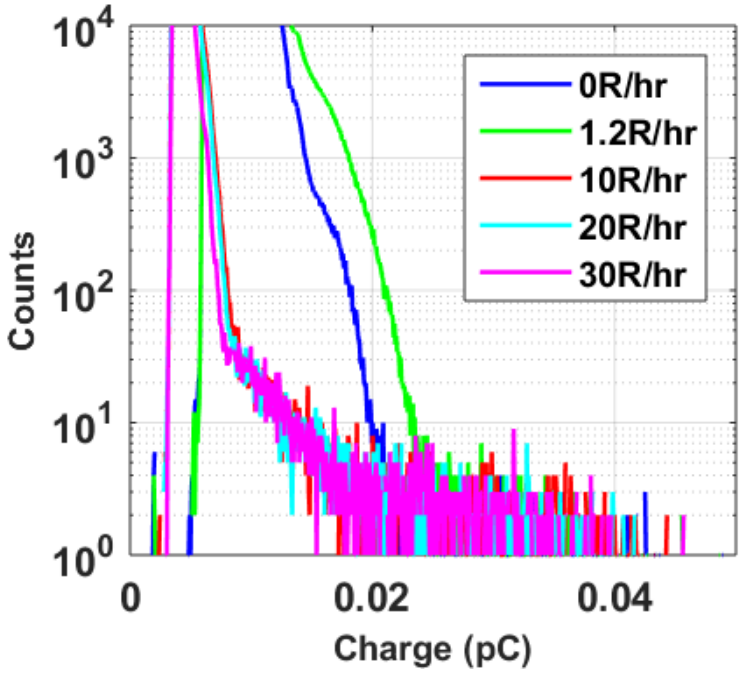

Figure 5.104 FC high radiation fields results: charge-sensitive mode, 100m cable, τ = 0.4μs.

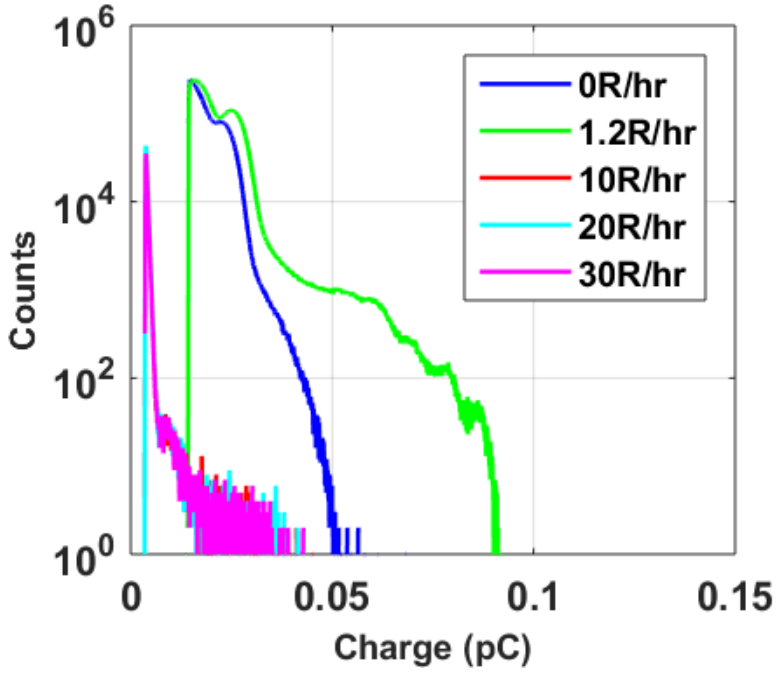

Figure 5.105 FC high radiation fields results: charge-sensitive mode, 100m cable, τ = 2.4μs.

Note that the neutron event lobe of the fission chamber spectrum is not clearly distinguishable for any of the tests in charge-sensitive mode, with 100m cable.

Table 5.44 Fission chamber high radiation test: Count rates above a nominal neutron-event thresholds for charge-sensitive mode, 1 m RG-71 cable.

Shaping	**Exposure**	**Counts**
0.1 μs	0 mR/hr	2907
0.1 μs	80 mR/hr	2664
0.1 μs	500 mR/hr	2669
0.1 μs	1.2 R/hr	2814
0.1 μs	10 R/hr	4131
0.1 μs	20 R/hr	4076
0.1 μs	30 R/hr	4092
0.4 μs	0 mR/hr	3617
0.4 μs	80 mR/hr	3195
0.4 μs	500 mR/hr	3351
0.4 μs	1.2 R/hr	3452
0.4 μs	10 R/hr	4191
0.4 μs	20 R/hr	4188
0.4 μs	30 R/hr	4247
2.4 μs	0 mR/hr	2513
2.4 μs	80 mR/hr	2674
2.4 μs	500 mR/hr	3008
2.4 μs	1.2 R/hr	3065
2.4 μs	10 R/hr	4374
2.4 μs	20 R/hr	4364
2.4 μs	30 R/hr	4337

Test Result: Inconclusive. When coupled to ^{3}He sensors, performance degrades significantly above 10 R/hr for typical shaping times, as expected. For ^{235}U fission chamber and charge-sensitive mode, performance is generally consistent with expectations but dose rates are likely too low to stress the system at shorter shaping times. Current-sensitive mode performs poorly over most scenarios—more investigation is needed.

6 REFERENCES

[1] Smith LE, Pochet T., Buben K. 2011. “Evaluation of Front-End Electronics for Unattended Safeguards Instruments.” IEEE Nuclear Science Symposium Proceedings.

[2] Smith LE, Svoboda J, Ianakiev K, et al. 2014. “Front-end Electronics for Verification Measurements: Performance Evaluation and Viability of Advanced Tamper Indicating Measures.” IAEA International Safeguards Symposium.

[3] Conrad R, Smith LE, Keller D, Morris SJ. 2015. “Front-End Electronics for Unattended Measurement: Prototype Test Plan”. Pacific Northwest National Laboratory, in preparation.

[4] IEEE Standard 301-1976. *IEEE Standard Test Procedures for Amplifiers and Preamplifiers for Semiconductor Radiation Detectors for Ionizing Radiation.*

[5] Ianakiev KD, et al. 2011. “Front-End Electronics for Thermal Neutron Detectors.” Proceedings of the ESARDA Symposium.

[6] Technical Specifications: Front-end Electronics for Unattended Measurements (FEUM)” (IAEA, February 2012)

7 APPENDIX 1: FEUM SCHEMATIC

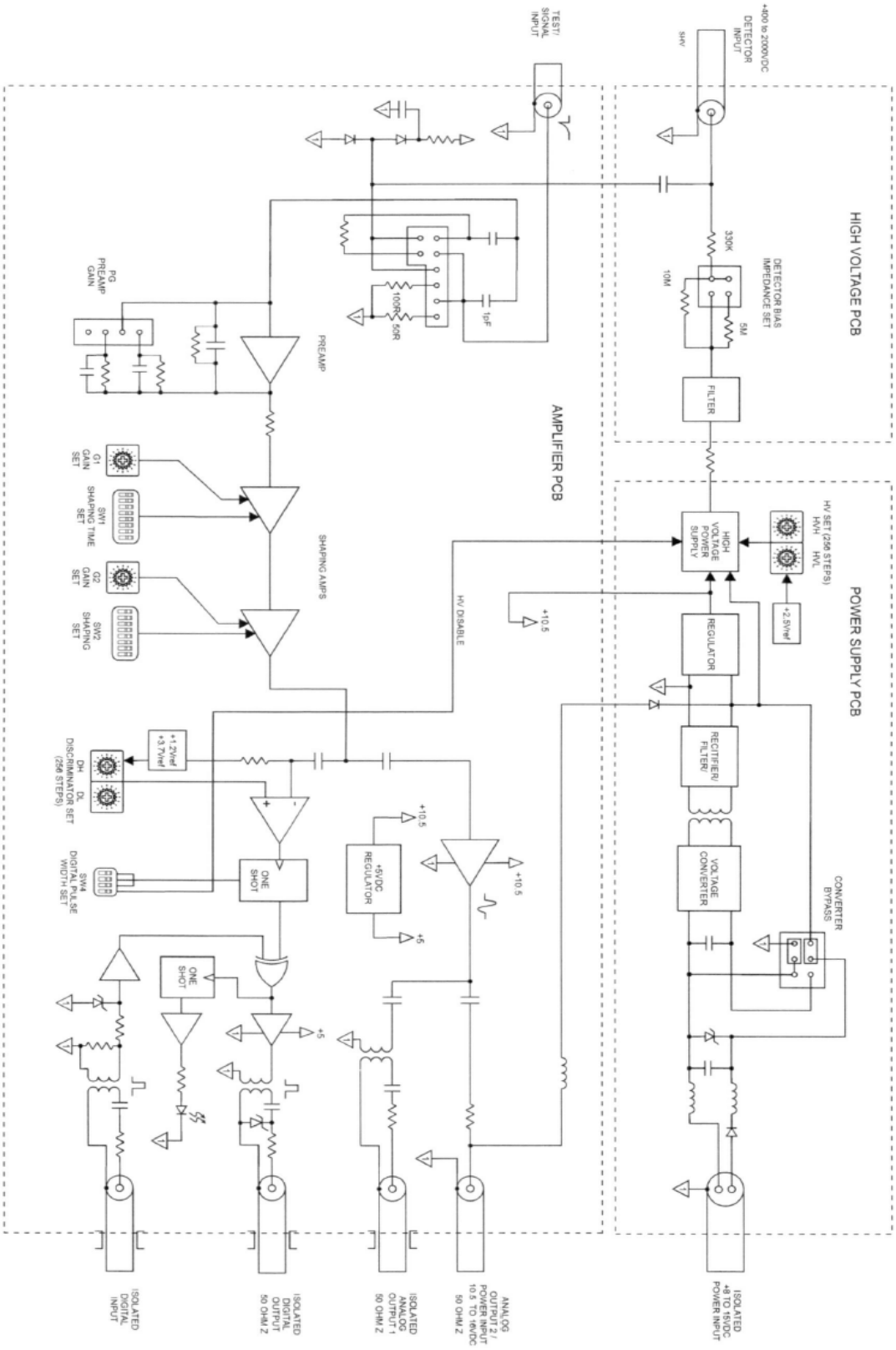

www.pnnl.gov

Pacific Northwest
NATIONAL LABORATORY

Proudly Operated by **Battelle** *Since 1965*

U.S. DEPARTMENT OF
ENERGY

902 Battelle Boulevard
P.O. Box 999
Richland, WA 99352
1-888-375-PNNL (7665)